Impact of Precipitation on Millimetre Wave Fixed Links and Mobile Measurement

YUSHENG CAO

Impact of Precipitation on Millimetre Wave Fixed Links and Mobile Measurement

By

Yusheng Cao

2025

Department of Engineering

Durham University, UK

Declaration

No part of the work described in this thesis has been submitted in support of an application for another degree or qualification to this or any other university or institute of learning.

Acknowledgments

I would like to thank Professor Sana Salous for giving me the opportunity to work on this exciting research theme, guidance and providing significant support for this PhD.

I would like to thank Dr. Adnan Cheema for helping in hardware design and the setup of the weather station, Dr. Xavier Raimundo for helping in Matlab coding and suggestions on data processing, Dr. Jack Tower for FPGA testing and debugging, Dr. Saied El-Faitori for the mobile measurements and Dr. Jie Huang for helping with scientific writing and channel modelling. I would like to thank Ian, Neil and Colin from the electronics workshop and Colin from the mechanical workshop for their support during the fixed link setup. I would like to express my gratitude to all the aforementioned friends and to those who have not been mentioned, for their assistance and support during my time in Durham. May our friendship last forever.

In the end, I would like to thank my family for their support and constant encouragement to complete my study and overcome all the difficulties even I was half a world away from them.

Abstract

Millimetre wave communication stands at the forefront of technological innovation, underpinning the development of fifth-generation and subsequent communication networks. Despite its promise, the propagation characteristic of millimetre wave radio links is significantly compromised by rain attenuation, an important factor during link budget calculations. This thesis undertakes a comprehensive investigation into the impact of precipitation on mmWave fixed links and mobile measurements, combining empirical weather data analysis with advanced channel sounding techniques to unravel the dynamics between rainfall and signal attenuation.

Central to this research is the deployment of a PWS100 laser disdrometer, a high-resolution meteorological instrument, to capture annual rainfall statistics encompassing intensity, duration, and drop size distribution (DSD). Complementing this, an advanced channel sounder operating at 25.84 GHz (K-band) and 77.52 GHz (E-band) was implemented to measure real-time signal attenuation across a 35-meter terrestrial link. These datasets enable an examination of how raindrop microphysics such as size, velocity, and the interaction with electromagnetic waves at mmWave frequencies.

This thesis evaluates established DSD models, including the Marshall-Palmer exponential model, log-normal distribution, and gamma distribution, to assess their fidelity in representing observed rainfall patterns in the Durham region, UK. While the Marshall-Palmer model offers simplicity, its limitations in capturing small-droplet dominance (<1.5 mm) under stratiform rain conditions are highlighted. On the other hand, the gamma distribution demonstrates superior adaptability to diverse rain regimes, accommodating both the skewed droplet populations of convective storms and the narrower spectra of prolonged stratiform events. This finding underscores the necessity of region-specific DSD model calibration, particularly in temperate climates characterized by mixed precipitation types. This thesis encompasses annual statistics of rain events, focusing on intensity, duration, and drop size distribution. This thesis employs various distribution models, including the Marshall and Palmer, log-normal,

and gamma distribution models, to fit the collected DSD data and evaluate their suitability for representing rainfall patterns.

A key finding of this thesis is the significant role of the wet antenna effect on short communication links and the importance of selecting appropriate scattering methods for the calculation of rain attenuation. The study reveals that the ITU-530 model may not be entirely suitable for short links and that a combination of Mie and Rayleigh scattering methods provides more accurate predictions for millimetre wave frequencies.

Overall, this research contributes to a better understanding of the complex interactions between rain and millimetre wave signals, offering valuable insights for the development of robust communication systems capable of operating efficiently under various weather conditions. The results of this research has also led to two journal publications and serval conference papers.

List of Abbreviation

ITU	International Telecommunication Union
ITU-R	International Telecommunication Union Recommendation
XPD	Cross Polar Discrimination
CPA	Co-Polar Attenuation
QAM	Quadrature Amplitude Modulation
QPSK	Quadrature Phase Shift Keying
SRAM	Static Random-Access Memory
PLL	Phase Lock Loop
CW	Continuous Waveform
WB	Wide Band
IF	Intermediate Frequency
LNA	Low Noise Amplifiers
TTL	Transistor-Transistor Logic
DDS	Direct Digital Synthesiser
FPGA	Field Programmable Gate Array
LPF	Low Pass Filter
PCI	Peripheral Component Interconnect
LOS	Line-of-Sight
NLOS	None-Line-of-Sight
DBSG3	Study Group 3 Data Banks
CCDF	Complementary Cumulative Distribution Functions
MLE	Maximum Likelihood Method
MOM	Mothed of Moments
NLSE	Non-Linear Least Square Error
WBS	Within-Boresight
OBS	Out-of-Boresight
CDF	Cumulative Distribution Function

Table of Contents

List of Figures

List of Tables

Chapter1 Introduction

1.1 Motivation and Objective

The millimetre wave is of increasing interest to communication service providers and many research groups due to the larger available bandwidth resource at this frequency range than in the lower frequency band. However, the transmission distance of millimetre wave is limited by the atmosphere (absorption by water vapour and oxygen) and the quality and stability of millimetre wave communication systems is strongly influenced by meteorological activities (precipitation like rain). Rainfall is a major source of attenuation for radio links operating at frequencies higher than 10 GHz [1] since the diameter of raindrops is similar to the wavelength at this frequency range. Raindrops absorb and scatter radio waves as a result which reduces the availability and reliability of the system. It is therefore very important to make an accurate prediction of attenuation when designing terrestrial communication systems. However, the complex meteorology events and regional variability of rain make the prediction hardly accurate.

Research on how rain influences radio wave propagation has been carried out for more than 70 years. It was first introduced by Wolff and Linder who measured the rain attenuation over a 2-mile path. Because of the resolution of equipment, no databased attenuation was observed [2]. Later in 1942, the Clarendan Laboratory group carried out the first positive measurement in this area and the experiment was followed by the Bell group [3]. From the 1970s, modelling of rain attenuation prediction methods became the most attractive topic in related researches. Various methods and effects have been studied from the characteristics of certain frequencies to rain drop size distribution in order to design an accurate and easy to implement model for rain attenuation calculation. In the meantime, research was focused on other relative problems caused by rain, for instance interference and depolarization, have some breakouts as well. In 1975, co-channel interference calculation was simplified by Bullington for most

engineering purposes [4]. The measurements of depolarization took place in New Jersey, America at frequency of 18 GHz in 1972 and different cross-polarization ratio between linear and circular polarized waves were discussed. [5]

1.2 Organization of Thesis

Chapter 1 establishes the scientific motivation and objectives of the study. It contextualizes the challenges posed by rain attenuation in mmWave bands (e.g., K-band at 25.84 GHz and E-band at 77.52 GHz) and points out the limitations of existing attenuation prediction models, particularly for short-range terrestrial links. By introducing historical research from early experimental studies by Wolff and Linder to modern ITU recommendations, the chapter highlights the need for region-specific and frequency-adaptive models.

Chapter 2 provides a systematic review of precipitation-induced attenuation mechanisms is presented, encompassing classical models (ITU-R P.530, Crane Global Model, Silva Mello-Pontes Model) and emerging approaches leveraging raindrop size distribution (DSD) data. The chapter critically evaluates the applicability of Rayleigh and Mie scattering theories across mmWave frequencies, demonstrating that conventional ITU models underestimate attenuation in short links due to oversimplified assumptions of uniform rain cell structure. Furthermore, it introduces the concept of wet antenna effects and discusses depolarization and interference mechanisms unique to mmWave frequencies.

Chapter 3 introduces the experiment set up of the project including: A PWS100 laser disdrometer for high-resolution DSD measurements which synchronized with meteorological sensors; A custom-built channel sounder operating in continuous-wave (CW) and wideband (WB) modes at 25.84 GHz and 77.52 GHz, featuring phase-locked loops, frequency multipliers, polarization-agile antennas; FPGA-based control units, and PCIe data acquisition cards to collect real-time signal attenuation and rain structure.

Chapter 4 provides the statistical analyses of precipitation data over one year, introduce the method to catalogue different types of rain events and also study several

particular rain events.

Chapter 5 shows three drop size distribution models, exponential distribution, lognormal distribution, and gamma distribution, are evaluated using maximum likelihood estimation and nonlinear least squares fitting. The superiority of Gamma distribution and the limitations of method of moments are discussed.

Chapter 6 analyses the recorded rain attenuation results, introduce formula derivation steps for Mie scattering and Rayleigh scattering to estimate the rain attenuation based on rain drop size distribution data. Wet antenna effects are also estimated by empirically derived attenuation.

Chapter 7 introduces a measurement of outdoor directional radio propagation in the V-band in urban canyons. Channel parameters like path loss exponents, delay spread, and angular spread are measured.

Chapter 8 summarizes the pervious chapters: experiments setting up, precipitation data analyses and rain attenuation modelling of the thesis. In the end, the potential of future research including new links with longer distance and longer term of data acquisition are listed.

1.3 References

[1] R. Crane, Electromagnetic wave propagation through rain. New York: Wiley, 1996.

[2] K. Nakamoto, Infrared and Raman spectra of inorganic and coordination compounds. New York: John Wiley, 1997.

[3] S. Joshi, A REVIEW ON RAIN ATTENUATION OF RADIO WAVES. 2019.

[4] "Rain Scatter", Mike-willis.com, 2019. [Online]. Available: http://www.mike-willis.com/Tutorial/rainscatter.htm. [Accessed: 29- Mar- 2019].

[5] Recommendation ITU-R P.838.3: “Specific attenuation model for rain for use in prediction methods” ITU-R P. Ser., Geneva, Switzerland, ITU International Telecommunications Union, 2005.

Chapter2 Precipitation Effects review

In this chapter, research background is given in four different significant areas: rain attenuation prediction models, depolarization effects introduced by rain, rain drop size distributions and interference caused by rain. For rain attenuation prediction models, there are several models designed for either earth-space links or terrestrial links. The following parts give brief introduction for the models which are suitable for terrestrial links.

2.1 Precipitation Attenuation Principles

Precipitation attention primarily refers to the path loss of radio wave caused by precipitation events like rain, snow and hail. The attenuation introduced by absorption and scattering of radio wave will become a vital part of total transmission losses [1]. In order to study how the precipitation events could influence radio wave propagation, the mechanism of how water molecules could impact radio waves need to be studied at first.

The absorption of electromagnetic radiation due to liquid water is basically caused by dielectric effects. Water molecules are electric dipoles and means the positive charge and negative charge are located at two opposite ends of the molecules [2]. In another word, water molecules are electrical directional. As a result, when radio waves trying to pass through water drops, water molecules will rotate and try to align with the alternating electronic-magnetic field of bypassing radio waves, and therefore energy of the radio wave is dissipated and causes part of the attenuation [3].

Scattering effect also plays an important role in precipitation attenuation. Two types of scattering are considered in this situation, Rayleigh scattering and Mie scattering. Rayleigh and Mie scattering depend on the relationship between the diameters of scattering particle d and the wavelength of incoming wave λ. If $d \ll \lambda$, Rayleigh scattering is suitable for that condition and if the ratio between particle diameter and wavelength is in the range of $1 \leqslant d/\lambda \leqslant 10$, Mie scattering should be

used in that case. However, it should be noticed that the Rayleigh and Mie scattering are not different mechanisms, the major difference between these two scattering models is when Mie scattering occurs, there is more forward scattering and a forward radiation lobe than Rayleigh scattering [4].

Since the frequency of this project is 72 and 24 GHz, the wavelengths are 4.17 and 10.71 mm respectively. Normally rain drops diameters changes from 0.1 mm to 5.5 mm, as a result, Mie scattering model is more accurate for the calculation of rain scattering parameters with large rain drop sizes.

2.2 Rain Attenuation Prediction Models

In this part different rain attenuation prediction models are introduced and comparison of advantages and disadvantages is given as well.

2.2.1 ITU models

ITU recommends two different rain attenuation prediction models depending on either statistical rain rate or one event rain rate. The ITU-R P.838 model is a basic model for rain attenuation predictions base on local rain rate [5]. It is widely used in system design because of its simple mathematical expression. In the recommendation, equations 2.1 and 2.2 are given below:

$$\gamma = kR^{\alpha} \tag{2.1}$$

$$A = \gamma d_{eff} \tag{2.2}$$

In these equations, specific attenuation γ (dB/km) is obtained from the rain rate R (mm/h) using the power-law relationship. The coefficients k and α are calculated by Rayleigh scattering equations 2.3 and 2.4

$$\log_{10} k = \sum_{j=1}^{4} \left(a_j e^{-\left(\frac{\log_{10} f - b_j}{c_j}\right)^2} \right) + m_k \log_{10} f + c_k \tag{2.3}$$

$$\alpha = \sum_{j=1}^{5} \left(a_j e^{-\left(\frac{\log_{10} f - b_j}{c_j} \right)^2} \right) + m_\alpha \log_{10} f + c_\alpha \tag{2.4}$$

where: f: frequency (GHz)

k: either k_H or k_V

α: either α_H or α_V

The effective length of the path d_{eff} in equation 2.2 is approximately equal to the distance between the transmitter and receiver when the distance factor r exceeds 2.5. The estimation equation of r in ITU-R P.530 is given by 2.5:

$$r = \frac{1}{0.477 d^{0.633} R_{0.01}^{0.073\alpha} f^{0.123} - 10.579\left(1 - e^{-0.024d}\right)} \tag{2.5}$$

Where f (GHz) is the frequency and α is the exponent in the table given by ITU-R P.838.

For the 77.52 GHz band is about 300 metre. The coefficients k and α which are derived from the *Rayleigh* scattering equations are tabulated in ITU-R P.838-3 with two sets of values for vertical and horizontal polarizations respectively. Though chosen for its simplicity, the empirical kR^α relation was tested in 1978 both theoretically and experimentally [6] and by far the frequency of tabulated k and α has been pushed up to 1000 GHz.

The ITU-R P.530 provides a statistical rain attenuation prediction algorithm based on long-term rain rate data and specific rain attenuation equations 2.1 to 2.5 [7]. Step-by-step implement procedure is listed below:

Step1: Depending on local rain rate measurement data, which need to be integrated every minute, or estimation based on global precipitation map given in ITU-R P.837, $R_{0.01}$ exceeded for 0.01% of the time need to be calculated first as an input for specific attenuation γ_R (dB/km).

Step2: Compute the attenuation using equation 2.1 and equation 2.2. The effective path length d_{eff} equals to actual distance between transmitter and receiver multiplied

by a length regression factor *r*.

Three different facts need to be noticed for the length regression factor. Firstly, in ITU-R P.530, the maximum value of *r* is recommended to be 2.5, which means for any denominator less than 0.4, *r* need to be picked as 2.5. Secondly, as mentioned before, if the value of d is very small for a short link, the effective path length should be considered as the actual path length. In conclusion, the estimated rain attenuation exceeded for 0.01% of the time is given by:

$$A_{0.01} = \gamma_R d_{eff} = \gamma_R dr \tag{2.6}$$

Step3: Regarding on the requirements of reliability from 99% of time to 99.999% of time, the derivation of predicted attenuation A_p is given by:

$$A_p = A_{0.01} C_1 p^{-(C_2 + C_3 \log_{10} p)} \tag{2.7}$$

with:

$$C_1 = (0.07^{C_0})\left[0.12^{(1-C_0)}\right] \tag{2.7a}$$

$$C_2 = 0.855C_0 + 0.546(1 - C_0) \tag{2.7b}$$

$$C_3 = 0.139C_0 + 0.043(1 - C_0) \tag{2.7c}$$

where:

$$C_0 = 0.12 + 0.4 \log_{10} \left(\frac{f}{10} \right)^{0.8} \tag{2.8}$$

when $f \geq 10\,\text{GHz}$, when $f < 10\,\text{GHz}$, $C_0 = 0.12$

The calculation steps given above by the ITU, are considered to be valid regardless of locations globally and for frequencies up to 100 GHz and maximum path lengths of 60 km.

The ITU-R P.838 and ITU-R P.530 specific rain attenuation prediction models can be a benchmark for other models to compare with and foundations of further models as well. Different adjustment factors are added to this equation based on different views of improvement. Some of the models try to increase the accuracy by transforming local rain rate into effective rain rate which has direct influence along the propagation path. Adjustment factors therefore are implemented to optimize rain rate. Some other models focus on changing the physical link length into effective path length which is covered

by rain rate which obeys certain distribution such as a uniform distribution along transmission path.

2.2.2 Crane model

The Crane global model is an attenuation prediction model which was developed for both Earth-space and terrestrial communication links. The unique design for that model is the prediction method which is based on global geophysical rainfall rate and rainfall structure [8]. Also none of the model constants was obtained from attenuation measurements. Instead, massive metrological data were acquired from different observatories all over the world in order to get a large number of samples for an accurate model. The equations that fit short range (less than 22.5km) terrestrial links are given below:

$$A\left(R_p, D\right) = \alpha R_p^{\beta}\left[\frac{e^{u\beta d}-1}{u\beta} - \frac{b^{\beta}e^{c\beta d}}{c\beta} + \frac{b^{\beta}e^{c\beta D}}{c\beta}\right] \tag{2.9}$$

Where

$$u = \frac{\ln[be^{ed}]}{d}$$

$$b = 2.3R_p^{-0.17}$$

$$c = 0.026 - 0.03\ln R_p$$

$$u = 3.8 - 0.6\ln R_p$$

The rainfall rate at the probability R_p can be obtained from either local measurements or weather stations. D is the distance between the transmitter and receiver. Coefficients α and β are both calculated from *Laws* and *Parsons* rain drop size distribution.

The Crane model also catalogued rain in 8 different types by climate and regions and provided an exceeded rain rate map [9]. If there is no local precipitation data, exceeded rain rate could be picked from the map for attenuation prediction. Comparing with the observations, this model's performance is reduced with increasing path length

for horizontal terrestrial links at frequencies of 10, 20 and 36.5 GHz. There is an evolution versions based on Crane global model as well. In 1982, the idea of path integrated technique was used to design a new model called the 2-component Crane model [10]. The two components are first, along the transmission path, rain is generated by some rain volume cells separated from each other and second, the rain rate measured by rain gauges alone the transmission path is provided by either rain volume cells or debris among them. Based on rain data collected from a 3-year radar measurement program, the author made an approximation that the attenuation introduced by debris roughly obeys a log-normal distribution function. Combined with the attenuation provided by independent volume cell, the two-component model is given by:

$$P(r \geq R) = P_c(r \geq R) + P_D(r \geq R) \tag{2.10}$$

$$P_C(r \geq R) = P_C e^{-\frac{R}{R_C}} \tag{2.11}$$

$$P_D(r \geq R) = P_D \eta \left(\frac{\ln R - \ln R_D}{\sigma_D} \right) \tag{2.12}$$

where $P(r \geq R)$ is the probability in percentage when observed rain rate r (mm/h) is larger than the specified rain rate R (mm/h) from global rain rate map in original Crane model. $P_C(r \geq R)$ and $P_D(r \geq R)$ are the distribution functions for volume cells and debris in percentage, P_C and P_D are the probability of a volume cell and debris occurs (percent) and R_C and R_D are the average rain rate of volume cells and debris respectively. σ_D is the standard deviation of the rain rate.

The Crane global model gave an alternative viewpoint of rain attenuation prediction since this model is focused on not only statistical meteorological data but also deeper analysis of precipitation processes. But it should also be noticed that the model was highly depending on empirical equations and historical data.

2.2.3 Silva Mello-Pontes model

The Silva Mello-Pontes model is different from the ITU model which assumes that the rain rate obeys uniform distribution along the propagation path. The experimental measurements were carried out in Brazil, which is considered to be a tropical climate

area, at 15, 18, 23 and 38 GHz [11]. This method uses the concept of an effective rainfall rate to represent the temporal and spatial variations of rain intensity along the path. It also performs better on predicting the attenuation at exceeded percentages from 1% to 0.001% than the ITU model and Crane model. Corrections were made for the underestimation by the ITU model in this gap. The equations are given:

$$A_p = kR_{eff}^{\alpha} \frac{d}{1+\frac{dR_p}{d_0}} \tag{2.13}$$

$$d_0 = 119R^{-0.244} \tag{2.14}$$

$$R_{eff} = 1.763R^{0.753+\frac{0.197}{d}} \tag{2.15}$$

The numerical coefficients in equation 2.13 to 2.15 were obtained by non-linear regression, based on the measured data in the ITU database. Effective rain-cell diameter d_0 and effective rain rate R_{eff} are introduced in this model. It is an alternative algorithm to use effective rain rate instead of effective path length. The attenuation changes caused by the rain-cell movement, which is mainly caused by wind, was included as well.

2.2.4 Drop Size Distribution model

The drop size distribution model uses raindrop size distribution and Mie scattering method to calculate the attenuation. Instead of using drop size distribution models, experimental distributions were measured by a Doppler radar [13]. Assumptions were made that only the first order scattering was involved in the attenuation estimation and the dielectric function of *Liebe* which covered the frequency range from 1 to 1000 GHz is used to calculate Mie extinction cross section [14][15]. The author also introduced "wet antenna effects", which is an additional attenuation caused by the water layer covered on the antennas [16]. The equations are given as:

$$\gamma = 4.343\int_0^\infty \delta_{ext}(D)N(D)dD \tag{2.16}$$

$$A_{sum} = A_p + A_a \tag{2.17}$$

In these equations, δ_{ext} is Mie extinction cross section for water drops of diameter D, N(D) is the drop size distribution value at diameter D. A_p stands for attenuation caused along the propagation path, which equals to γ multiplied by the distance between the transmitter and receiver for short links. A_a is the wet antenna attenuation which is proposed by the empirical relationship given in equation 2.18:

$$A_a = C(1-e^{-dA_p}) \tag{2.18}$$

C and d are model parameters. The parameter is estimated by inspection of the largest systematic differences between predictions and measurements, and is calculated by nonlinear regression of the model in the observation period. In practice, the wet antenna effect is around 2dB in links similar to this project (path length 840m, frequency 75-85 GHz, urban surrounding) [17]

Drop size distribution model is widely used because it could go deep into the micro structure of a rain event. Unlike the other models mention above which was based on rain rate to estimate the attenuation, drop size distribution is another parameter which could differentiate between different rain events with the same rain rate. For example, here listed three different rain events observed in this project in January 2018:

Table 2.1 Table of three different rain events in January 2018

	Event 1	Event 2	Event 3
Lasting Hours	4 hours	4 hours	2.5 hours
Peak Rain Intensity	2.84 mm/hr	9.12 mm/hr	2.05 mm/hr
Average Rain Intensity	0.5085 mm/hr	1.5816 mm/hr	0.6073 mm/hr
Standard Deviation	0.6371 mm/hr	1.9890 mm/hr	0.4558 mm/hr

Event1 lasted for 4 hours with a peak rain rate of 2.84 mm/hr, event 2 lasted for 4 hours as well with a peak rain rate of 9.12 mm/hr and event 3 lasted for 2.5 hours with a peak rain rate of 2.05 mm/hr. From the table, these three rain events were easy to

distinguish as event 2 had quite stronger peak rain intensity and larger standard deviation while event 3 was changing smoothly.

Figure 2.1 shows the percentages of drops at different diameters, It indicates that the peak of DSD of event 1 is shifted to smaller size around 0.5 mm for event 1 and droplets with diameters around 0.7 mm occupied most weight for event 2 and event 3:

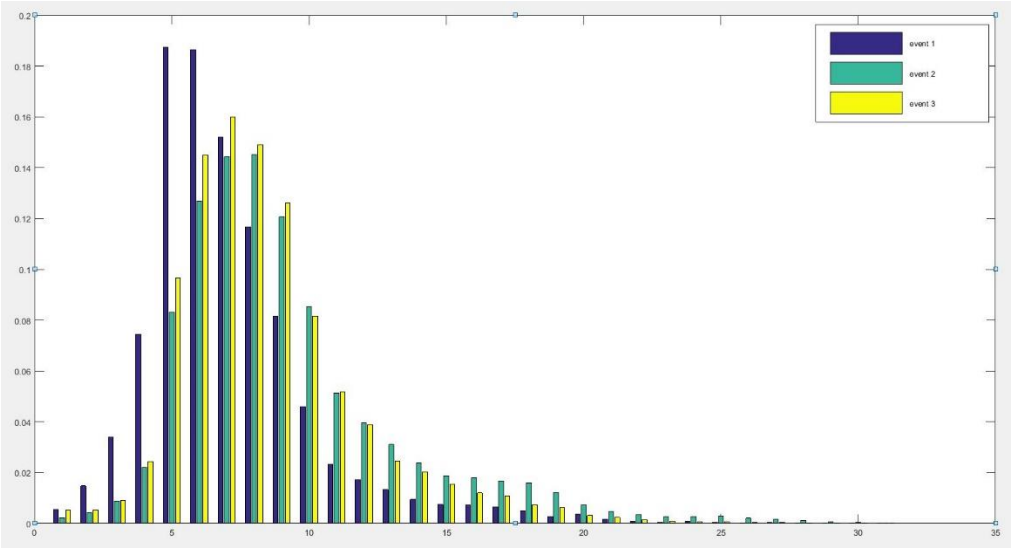

Figure 2.1 Percentages of drops distribution at different diameters

A reasonable explanation could be these three rain events were brought by different types of clouds, convective cloud or stratiform cloud. Meteorologists have indicated that droplets grow in two different ways in those two types of clouds. If the droplets grow in convective clouds, the primary procedure of collecting water will be coalescence and/or rimming. On the other hand in stratiform clouds droplets will grow by vapor diffusion.[18] The different generations of drops give rainfall different characteristics: stratiform rain normally has a lower rain rate and a lower standard deviation of rain rate statistic and convective rain normally has either a higher rain rate or a higher standard deviation of rain rate.[19] However if rain rate is the only parameter to describe the rain events, huge amount of detailed information of those events will be lost and it is not accurate considering the principle of how precipitation attenuates the millimetre wave.

2.2.5 Adjusted ITU model

The model proposed by China is a model with adjustment factor of rain rate [20]. It is proposed to revise the ITU-R P.530 model. The model can be expressed as

$$A(p) = k\left[r(p)R_0(p)\right]^{\alpha} L \tag{2.19}$$

Based upon the experimental data of ITU study group 3 databank (DBSG3), the rainfall rate adjustment factors have been obtained. For terrestrial line-of-sight links these are given by equation 2.20:

$$r = 0.059R_0^{-0.12+\frac{0.22}{L}}(1+32.9\frac{p^{0.065}}{1+0.12L}) \tag{2.20}$$

Research shows that the China_2012 model may get unseasonable results when the path length is shorter than 0.5 km. In order to solve the problem, a threshold is added to the model. When the rainfall rate adjustment factor is larger than 2.5, that is the maximum recommended is 2.5 both for the terrestrial line-of-sight links and the earth-space links. In 2017, the research group proposed an improvement of pervious model [21] to modify the unreasonable adjustment factor problem mentioned above with an additional part of wet antenna effect. The parameters of new model are derived by regression with experimental data in DBSG3 as follows:

$$A(p) = k\left[r(p)R(p)\right]^{\alpha} L + A_a \tag{2.21}$$

$$r(p) = \frac{1}{1+\frac{0.29L^{0.4}R(p)^{0.12}}{1+19.51p^{0.82}}} \tag{2.22}$$

$$A_a = 1.07f^{0.75}(1-e^{-0.04R(p)^{0.67}}) \tag{2.23}$$

With these new expressions, the application range on frequency of this model is extended up to 100 GHz and path length up to 60 km and also improves the accuracy for links with short distance (less than 1 km).

2.3 Depolarization Effect

Depolarization caused by rain is also a critical problem in millimetre wave

communication systems. The principle of depolarization effect is similar with the rain attenuation. When the wavelength is comparable with the diameter of the rain drops, the forward scattering wave have different phase shifts and attenuations which causes depolarization. Cross polar discrimination (XPD) which is the power ratio of transmitted signal and received signal in orthogonal polarization and co-polar attenuation (CPA) which is the power ratio of transmitted signal and received signal in same polarization can be used to present the influences of rain on depolarization and attenuation. Both of them depend on the structure of rain, including rain drop size distribution, drop shape and drop orientation. According to reported research, differential phase makes a large contribution to depolarization than differential attenuation does because the differential attenuation is quite small. But there are still many papers that consider both of them in XPD calculations [22].

2.3.1 ITU model

Different methods have been used to calculate XPD. In ITU-R P.530-17 [23], a method of computing depolarization outage due to clear-air and precipitation based on statistic rain rate are given respectively. The whole procedure is listed in the recommendation step by step and easy to implement. However, the method given by the ITU estimates XPD distribution by using the equal-probability relation:

$$XPD = U - V(f)\log CPA \tag{2.24}$$

The coefficients U and $V(f)$ are in general dependent on serval variables, including frequency f and empirical parameters and in situation of line-of-sight path with minor tilt angles, the estimated coefficients are given by:

$$U = U_0 + 30\log f \tag{2.25}$$

$$\begin{aligned} V(f) &= 12.8 f^{0.19} \\ V(f) &= 22.6 \end{aligned} \tag{2.26}$$

for $8 \le f \le 20\,\text{GHz}$ and $20 < f \le 35\,\text{GHz}$,respectively.

According to the recommendation, an average value of U_0 is around 15 dB.

A semi-empirical equation to rescaled long-term XPD statistics of one frequency to another frequency is also given in the recommendation. However it is limited by a small frequency range:

$$XPD_2 = XPD_1 - 20\log(\frac{f_2}{f_1}) \tag{2.27}$$

for $4 \le f_1, f_2 \le 30\,\text{GHz}$

All the results given above are based on measured or statistic CPA but these coefficients only have been validated up to 35 GHz which is a relatively low frequency. Therefore, improvements of two aspects could include: (1) find a direct way of calculation the XPD value not based on correlation relationships with CPA but based on metrological data and frequencies and (2) modify the equation for higher frequency bands.

2.3.2 Oguchi model

Besides the ITU method, which is focused on statistical data and empirical parameters, there are methods which are based on scattering of each individual rain drop and then integrate the depolarization effects to get the whole influence over a rain cell. In *Oguchi's* paper [24], differential attenuation and phase shift can be estimated from the forward scattering amplitudes:

$$\Delta A = 8.686\,\text{Im}(k_h - k_v)L \tag{2.28}$$

$$\Delta\Phi = \frac{180}{\pi}\text{Re}(k_h - k_v)L \tag{2.29}$$

where k_h and k_v stand for the horizontal and vertical components of actual propagation constants in the rain-filled medium respectively and L is the path length through the medium. k_h and k_v can be expressed as equation 2.31:

$$K_{h,v} = (\frac{2\pi}{k})\int f_{h,v} n(a)da \tag{2.30}$$

f_h and f_v are the forward scattering amplitudes in the horizontal and vertical direction due to rain drops having drop size distribution $N(a)$, stands for the radius

of the rain drops. The result will be different depending on which model of drop size distribution is implemented. In some papers, researchers measured raindrop size distributions and indicated the data are directly related to XPD and CPA.

2.4 Interference

Interference is another issue that could happen during rain events. When transmitted waves come across the droplets, both scattering and absorption occur at the same time. There is a high possibility for the transmitted wave to scatter away from the original direction and interrupt other nearby links. Though the power of scattered wave might be small, in some case it could not be ignored. Beside co-channel interference, dispersion of pulses occurs when radio waves propagate through a medium [25]. As a result, the pulse width is broadened and this distortion will cause an increasing on bit error rate therefore reduces the accuracy of communication links.

For this particular project, co-channel interference is the focus to face the industry and regulation needs. A general method derived from radar equation was given by *K. Bullington* by assuming that the rain cell is made up by a large number of small droplets [26]. All the droplets are spaced with an approximately uniform distribution along the common volume. Therefore, the rain cell could be considered as a reflector and scattered power can be calculated. Similar research has been done by *C.Enjamio* with improvement on rain cell model based on experimental data in multipoint to multipoint and cellular communication systems [27]. Simulation is also implemented in this research taking into account some multiple scattering to make the results more reasonable. Different coding technologies e.g. Reed Solomon and Convolutional Coding combined with different modulation methods e.g. Quadrature Amplitude Modulation (QAM) and Quadrature Phase Shift Keying (QPSK) were discussed and compared to show the interference tolerance of different combinations.

2.5 Summary

This chapter comprehensively reviewed the research background and modelling

methods related to the impact of precipitation on radio wave propagation, categorizing them into three main aspects: rain attenuation prediction models, depolarization effects, and interference.

Regarding to rain attenuation prediction models, several models applicable to terrestrial links were introduced. The ITU models, including ITU - R P.838 and ITU - R P.530, were widely used as benchmarks. The former was based on local rain rate and had a simple mathematical form, while the latter provided a statistical algorithm based on long - term rain rate data. However, they had limitations, such as the empirical nature of some coefficients and potential inaccuracies for short links. The Crane model, developed for both Earth - space and terrestrial links, was based on global geophysical rainfall rate and structure. It offered a different perspective but highly depended on empirical equations and historical data. The Silva Mello - Pontes model took into account the temporal and spatial variations of rain intensity using the concept of effective rainfall rate and performed well in predicting attenuation at certain exceeded percentages. The Drop Size Distribution (DSD) model used raindrop size distribution and Mie scattering method, considering the "wet antenna effects" and providing a more in - depth understanding of rain attenuation from the micro - structure of rain events. The Adjusted ITU model was a modification of the ITU - R P.530 model with adjustment factors for rain rate, aiming to improve accuracy, especially for short - distance links.

Depolarization caused by rain was another crucial issue in millimetre - wave communication systems. The ITU model calculated depolarization outage based on statistical rain rate, but its coefficients were only validated up to 35 GHz. The Oguchi model, on the other hand, estimated depolarization from the forward scattering amplitudes of individual rain drops.

Interference during rain events was also discussed. When radio waves interacted with raindrops, scattering and absorption occurred, which might lead to co - channel interference and pulse dispersion. A general method derived from the radar equation was used to calculate the scattered power, and different coding and modulation technologies were compared to show their interference tolerance.

In conclusion, this chapter systematically presented different modelling methods for the impact of precipitation on radio wave propagation. The performances of these methods were further compared in subsequent chapters to provide a comprehensive understanding and contribute to the development of more accurate prediction models and reliable communication systems. For each research interests, different modelling methods are introduced and the performances of different modelling methods will be compared in Chapter 4 and Chapter 5.

2.6 References

[1] R. Crane, *Electromagnetic wave propagation through rain*. New York: Wiley, 1996.

[2] K. Nakamoto, *Infrared and Raman spectra of inorganic and coordination compounds*. New York: John Wiley, 1997.

[3] S. Joshi, *A REVIEW ON RAIN ATTENUATION OF RADIO WAVES*. 2019.

[4] "Rain Scatter", *Mike-willis.com*, 2019. [Online]. Available: http://www.mike-willis.com/Tutorial/rainscatter.htm. [Accessed: 29- Mar- 2019].

[5] Recommendation ITU-R P.838.3: "Specific attenuation model for rain for use in prediction methods" ITU-R P. Ser., Geneva, Switzerland, ITU International Telecommunications Union, 2005.

[6] R. Olsen, D. Rogers, and D. Hodge, "The aRb relation in the calculation of rain attenuation," *IEEE Transactions on Antennas and Propagation,* vol. 26, no. 2, pp. 318–329, Mar. 1978.

[7] Recommendation ITU-R P.530-17: "Propagation data and prediction methods required for the design of terrestrial line-of sight systems" ITU-R P. Ser., Geneva, Switzerland, ITU International Telecommunications Union, 2017.

[8] R. Crane, "Prediction of Attenuation by Rain", *IEEE Transactions on Communications*, vol. 28, no. 9, pp. 1717-1733, 1980. Available: 10.1109/tcom.1980.1094844 [Accessed 29 March 2019].

[9] R. Crane, "Attenuation due to rain--a mini-review," *IEEE Transactions on Antennas and Propagation,* vol. 23, no. 5, pp. 750–752, Sep. 1975.

[10] R. Crane, "A two-component rain model for the prediction of attenuation statistics", *Radio Science*, vol. 17, no. 6, pp. 1371-1387, 1982. Available: 10.1029/rs017i006p01371.

[11] L. A. R. da Silva Mello, M. S. Pontes, R. M. de Souza, and N. A. Pérez García, "Prediction of rain attenuation in terrestrial links using full rainfall rate distribution," *Electronics Letters,* vol. 43, no. 25, p. 1442, 2007.

[12] L. da Silva Mello, M. P. C. Almeida, F. J. A. Andrade, and M. S. Pontes, "Influence of wind direction on rain attenuation in terrestrial line-of-sight links," *2013*

SBMO/IEEE MTT-S International Microwave & Optoelectronics Conference (IMOC), Aug. 2013.

[13] J. M. Garcia-Rubia, em. Riera, P. Garcia-del-Pino, and A. Benarroch, "Attenuation measurements and propagation modeling in the w-band," *IEEE Transactions on Antennas and Propagation,* vol. 61, no. 4, pp. 1860–1867, Apr. 2013.

[14] G. Mie, "Beiträge zur optik trüber medien, speziell kolloidaler metallösungen,"*Ann. Phys.*, vol. 25, pp. 377–445, 1908.

[15] H. J. Liebe, G. A. Hufford, and M. G. Cotton, "Propagation modelling of moist air and suspended water/ice particles at frequencies below1000 GHz," in *Proc. 542, Atmosph. Propag. Effects Through Natural Man-Made Obscurants Visible toMM-Wave Rad. AGARD Conf.,* 1993, pp. 3.1–3.10.

[16] J. M. Garcia-Rubia, J. M. Riera, A. Benarroch, and P. Garcia-del-Pino, "Estimation of rain Attenuation from experimental drop size distributions," *IEEE Antennas and Wireless Propagation Letters*, vol. 10, pp. 839–842, 2011.

[17] A. Benarroch, J. M. Garcia-Rubia, J. M. Riera, P. Garcia-del-Pino, and G. A. Siles, "Propagation measurements on terrestrial links in Madrid,"*2014 XXXIth URSI General Assembly and Scientific Symposium (URSI GASS)*, Aug. 2014.

[18] ITU-R Doc. 3M/28," China_2012 model improvement and additional analysis with other rain attenuation prediction models proposed to ITU-R P.618 and ITU-R P.530", Study Group 3, China,2016.

[19] A. Maitra and A. Adhikari, "Studies on some characteristics of rain-induced depolarization of Ku-band signal over an earth-space path at a tropical location," *Journal of Atmospheric and Solar-Terrestrial Physics*, vol. 121, pp. 83–88, Dec. 2014.

[20] ITU-R Doc. 3M/178, Proposed revision to Recommendation ITU-R P.530-16 - Analysis of wet antenna effect and rain attenuation prediction modelling, China, 2017.

[21] Recommendation ITU-R P.536.17: "Propagation data and prediction methods required for the design of terrestrial line-of-sight systems" ITU-R P. Ser., Geneva, Switzerland, ITU International Telecommunications Union, 2017

[22] T. Oguchi, "Electromagnetic wave propagation and scattering in rain and other hydrometeors," *Proceedings of the IEEE*, vol. 71, no. 9, pp. 1029–1078, 1983.

[23] K. Al-tabatabaie, J. Din, N. H. H. Khamis, and M. R. U. Islam, "Co-channel interference for site diversity during heavy rain in LMDS system," *2008 IEEE International RF and Microwave Conference*, Dec. 2008.

[24] K. Bullington, “Rain-scatter interference in terrestrial microwave systems,” *Bell System Technical Journal,* vol. 54, no. 1, pp. 177–187, Jan. 1975.

[25] C. Enjamio, E. Vilar, and F. Perez-Fontan, "Rain scatter interference in mm-wave Broadband fixed wireless access networks caused by a 2-D dynamic rain environment," *IEEE Transactions on Wireless Communications*, vol. 6, no. 7, pp. 2497–2507, Jul. 2007.

Chapter3 Experiment Set Up

In this chapter, the implementation of both radio propagation measuring and meteorological data acquired equipment are described. For radio propagation measurements, fixed link setting up and sounding system working at 77 GHz and 25 GHz are introduced with details including hardware design software programming, interconnections, data recording and real time performance monitoring in order to give a clear description of the system. For precipitation data recording, functions and specifications of the used laser disdrometer and supporting software is given. Summaries of the combining system will also be given later in the chapter.

Figure 3.1 shows the system diagram of the experiment set up, in order to study the impact of rainfall on electromagnetic wave propagation, a fixed communication link was designed and installed on the rooftop. An advanced channel sounder was used to acquire the attenuation data of electromagnetic wave propagation during rainfall, while a weather station was employed to monitor the precipitation data that affect the communication link. After obtaining these two types of data, the impact of rainfall on the propagation of electromagnetic waves at specific frequencies was studied by analysing the relationship between them.

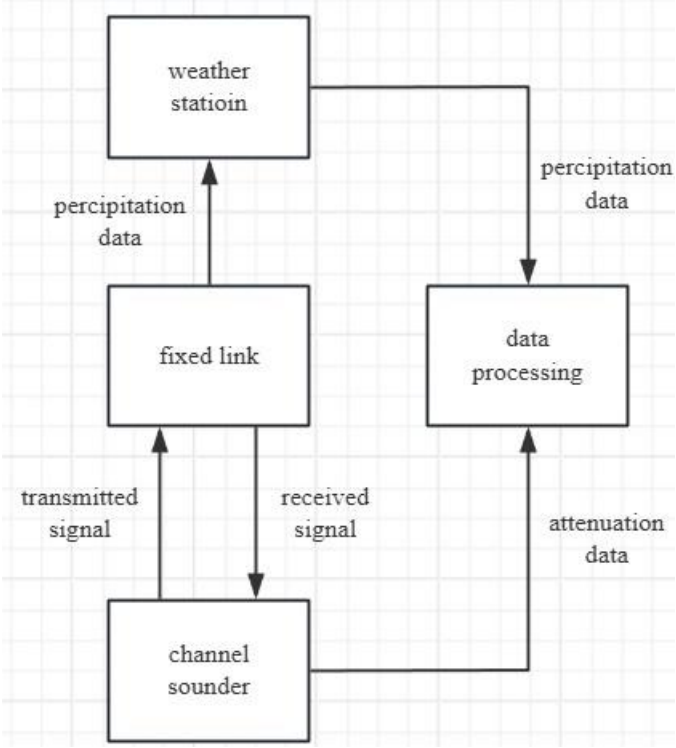

Figure 3.1 Block diagram of the experiment system

3.1 Weather Station

A laser disdrometer is installed on the roof top of the Bill Bryson Library to acquire the meteorology data including rain rate, temperature, rain drop speed and rain drop size distribution. Measured data are saved as text files every minute and transferred to a workstation through wireless network.

3.1.1 Specification of weather sensor and data logger

PWS100 weather sensor is used for this project [1]. It is a laser-based sensor with capability to measure accurate size and velocity of water drops in the air. Advanced algorithms are implemented as well to identify the particle type.

The weather sensor is mounted on top of the frame and it is assembled with one laser generator, two laser sensors and an embedded digital signal processor. The axes of laser sensors have a 20 degree angle with the axis of laser generator on vertical plane and horizontal plane, respectively. All of them are connected with the digital signal

processor which is fixed at the post beneath them. When a particle falls through the horizontal light sheets which are generated by the laser generator [2], part of the reflected light will be collected by laser sensors and transferred to the digital signal processor. Computations depending on the time difference between the received signals are carried out to give an output which contains drop diameters, falling speed and further results like rain rate and intensity. The processing procedure could also distinguish the types of sensed drops by their diameters and velocities and save into different catalogues like drizzle, rain, snow and hale. The algorithm also has a function of highlighting and removing suspicious and unknown particles to prevent possible errors occur in data recording. After initial processing, data are transferred to CR1000 data logger and then to the workstation located in the Department of Engineering through a wireless network.

Table 3.1 Measurement specification for PWS100 weather station

Particle Size	0.1 to 30 mm
Size Accuracy	±5%(for particles > 0.3mm)
Particle Velocity	0.16 to 30 m/s
Velocity Accuracy	±5%(for particles > 0.3mm)
Types of Precipitation Detected	Drizzle, rain, snow grains, snowflakes, Hail, ice pellets, graupel, mixed
Rain Rate Intensity Range	0 to 400 mm/h
Rainfall Resolution	0.0001 mm
Rain Total Accuracy	Typically: ±10%

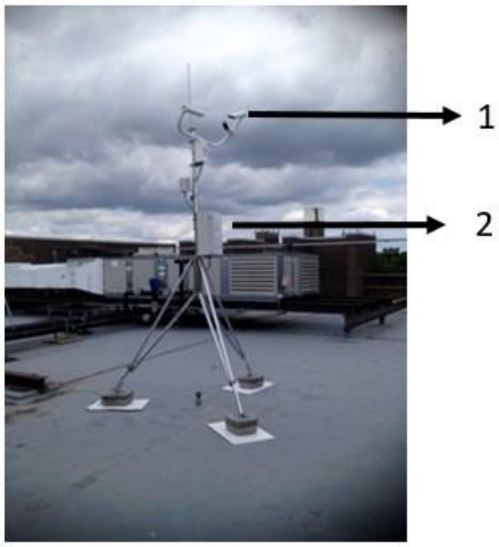

Figure 3.2 Weather station installed on the roof top

1: Laser sensors, 2: Data logger

3.1.2 Data transferring and supporting software

CR1000 measurement and control data logger and LoggerNet software are used combined with PWS100 sensor to record, transfer and save precipitation data. The CR1000 data logger has two main parts for the functions of measurement control and wiring /interconnections. It allows 16 single-ended or 8 differential data inputs and could drive outputs with different internet protocols for further data transmissions. Data acquired by laser sensors are reformatted and adding information including date and time and send to the workstation through internet. A 4 MB battery-backed SRAM is fixed inside the data logger as well to avoid data loss because of power shut down or unstable internet connections [3].

LoggerNet Software is installed on the workstation in the lab to control the data collections, monitor the working status of the weather station remotely from the field and save all collected data on a local hard drive. For the control of data acquisition, a custom program is written in CRBasic language to configure the weather station collect data every minute and save the data in ASCII format for further processing. The working status could be checked in real time and collected data files could be viewed

and graphed using real-time viewer for monitoring and troubleshooting [4].

3.2 Channel Sounding System

An advanced channel sounding system is used for radio propagation data collections in this project. It contains the following parts: a clock source and a control unit, two sets of Phase Lock Loops (PLL) to generate either Continuous Waveform (CW) or chirp signal for Wide Band (WB) measurements, one transmission unit and two receiving units for direct link and side link respectively and a workstation with data acquisition card for data collections and storage. The frequency of signals generated by PLLs is around 2.5 GHz, through several frequency up-converters and amplifiers, the output signal frequencies at the transmitter are increased to 77 GHz and 25 GHz for E-band and K-band respectively and signal will then transmit through a fixed path which has a length of 35 metres and reach both receivers. By comparing the signal strengths of clear sky propagation and the power levels after transmission through precipitation droplets, the relative attenuation, cross-polarisation effect and scattering energy is collected. A block diagram of the system is given in Figure 3.2 and detailed introductions will be given later in this chapter.

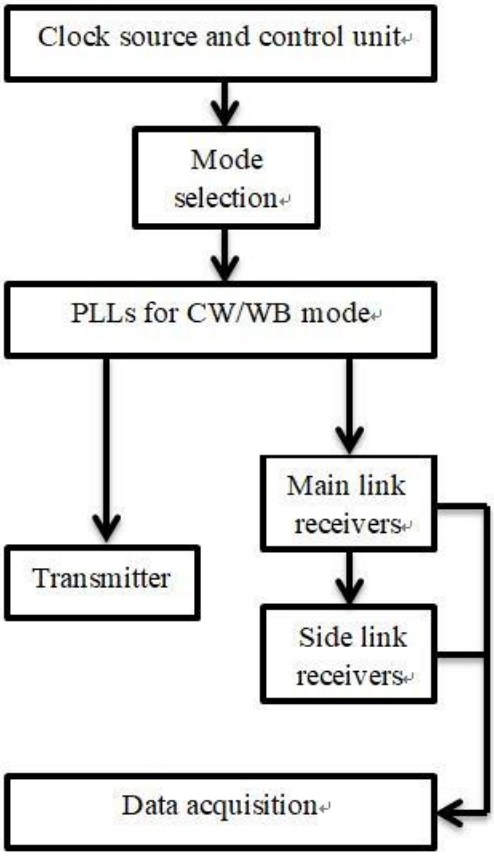

Figure 3.3 Block diagram of the channel sounding system

3.2.1 Clock source

The clock source of the sounding system is generated by a rubidium clock [5]. It provides the global clock for the whole system. To make the clock source capable to do so, the output of the rubidium clock, which is 10 MHz, is multiplied and amplified into 10 different phase coherent reference clocks from 10 MHz to 80 MHz by a clock distribution circuit [6].

Table 3.2 Summary of reference clocks

Frequency (MHz)	Waveform Type	Voltage levels (max, min) (V)	Number of Outputs
10	Square	(+3.3, 0)	2
10	Sine	(+1.2, -1.2)	2
20	Sine	(+1.2, -1.2)	2
40	Sine	(+1.2, -1.2)	2
80	Sine	(+1.2, -1.2)	2

A metallic unit is assembled to pack the rubidium clock and clock distribution

circuit together with power transformer to make the unit suit for both AC mains and 12 V DC supply. A set of rechargeable battery is also put in this unit to maintain its working temperature and its locking status when there is no power source connected.

3.2.2 Phase Lock Loops

Two sets of PLL units are prepared for this project. By choosing different PLL units at the first Intermediate Frequency (IF) stage, the sounding mode is changing for CW mode and WB mode without interrupting further connections or transmitter and receivers.

3.2.2.1 CW mode

When working in the CW mode, two outputs local oscillator which contains two PLLs is modified to give two outputs at 2.5 GHz and 2.501 GHz with 1 MHz difference. Both PLLs are locked to the 20 MHz signal from the rubidium clock. These two outputs are then transferred to transmitter and receiver units respectively after amplification and filtering.

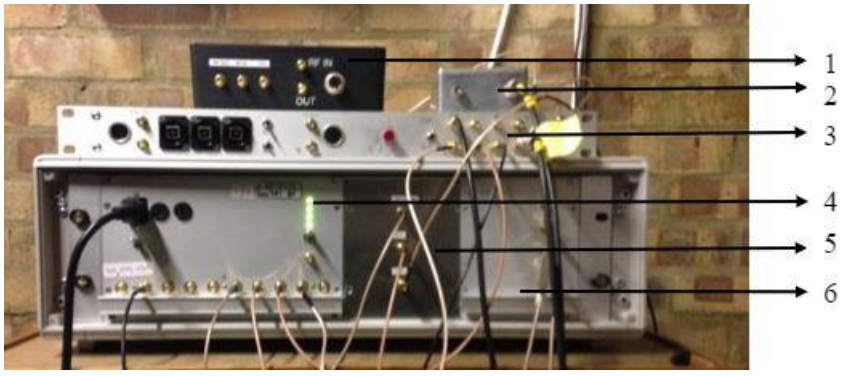

Figure 3.4 Front view of CW mode unit

1: Amplification unit, 2: Frequency divider, 3: Control unit,
4: Rubidium clock unit, 5: CW mode local oscillator, 6: Filter unit

The outputs of PLLs is first fed to the amplification unit which contains two Low Noise Amplifiers (LNA) to increase the signal power level because the signals are going through a long cable (around 25 metres to the transmitter and 60 meters to the receiver) and the signal should be strong enough to drive the second IF after subtracting the loss introduced by the cables. A switch is assembled inside the amplification unit and controlled by a 500 Hz Transistor-Transistor Logic (TTL) level square wave which is

generated by the control unit in order to change the transmitting polarizations. Then the amplified signals are going through the filter unit to remove the noise brought by the amplification unit to make the signals clean. At the output of the filter unit the signal powers are 15 dBm and 18 dBm for 2.5 GHz and 2.501 GHz respectively and these two outputs are connected to the transmitter unit and the receiver unit to drive the second IF units.

3.2.2.2 WB mode

Instead of the two outputs local oscillator mentioned above, two Direct Digital Synthesiser (DDS) units are used for the wideband test. The DDS boards are commercial boards and the units were assembled at Durham University. With a USB interface and supported program written in C++ on the PC, these units could generate frequency sweeps from 2.15 GHz to 3 GHz with programmable parameters including start frequency, end frequency and step size. In this project, these units are set of to generate frequency sweeps starting from 2.25 GHz to 3 GHz with a bandwidth of 750 MHz and sweep duration of 1.6 msec.

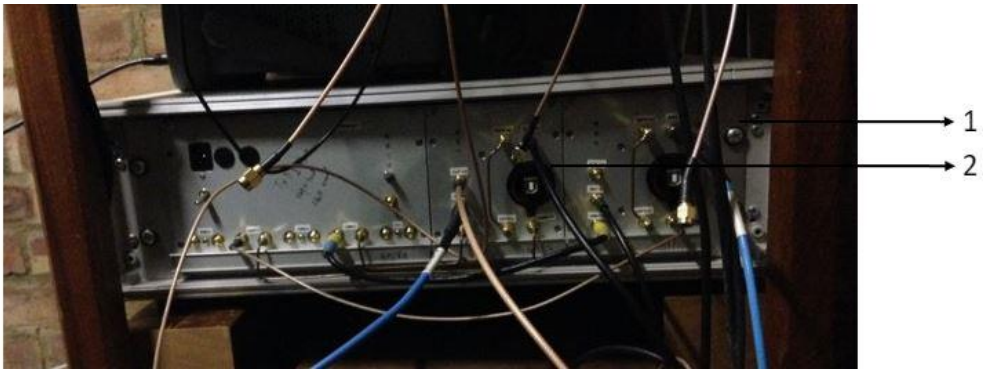

Figure 3.5 Front view of WB mode unit

1: DDS unit for transmitter, 2: DDS unit for receiver

The DDS units are working in “trigger mode” which means each sweep is activated when there is a positive edge detected at the trigger input port on the front panel of the units. Both trigger signals for these units are generated by the control unit and there is a fixed time delay between them. Because the sweeps have the same start and stop frequencies and same sweep durations, the frequency difference between the outputs of the two units is fixed and the different value could be adjusted by changing the time delay parameter when programing the control unit. For this project the

frequency difference is set at 1.6 MHz and a referencing signal with frequency of 1.0498 MHz is also connected to the front panel and further connected to the control unit to generate the trigger signal. Figure 3.5 shows how the frequencies of both DDS units' outputs are changing when triggers with fixed time delay Δt are implemented.

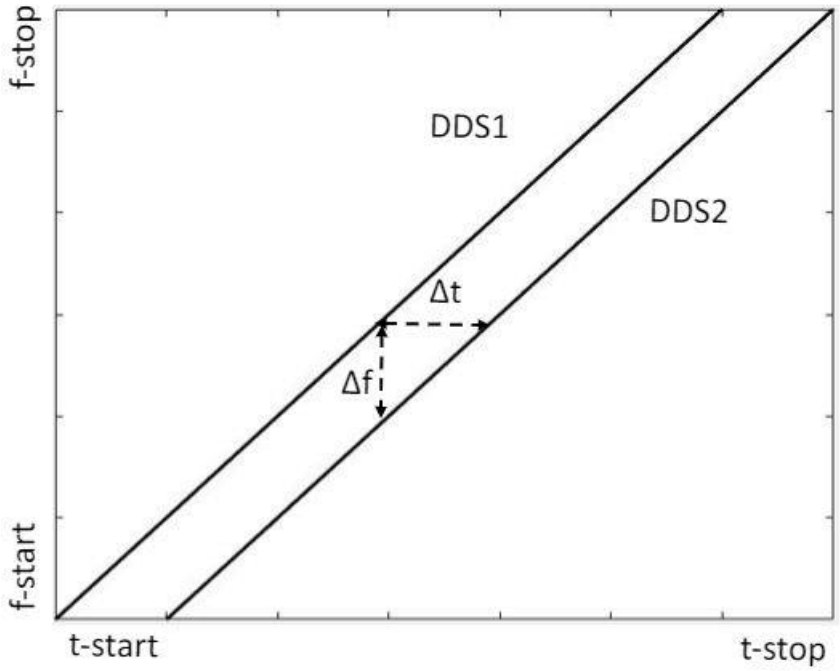

Figure 3.6 frequencies against time figure for DDS1 and DDS2 with fixed time delay Δt

As the figure shows, when the time delay Δt is fixed, the frequency difference between the sweeps of the two DDS units Δf is a constant. As a result, the frequency of the baseband signal at the data collecting end will be a multiple of Δf depending on the number of frequency multipliers the signal goes through to reach the RF frequencies.

3.2.3 Control unit

A control unit with a Field Programmable Gate Array (FPGA) is used to control the signal transmission. Three main functions are achieved by this unit, first function is to generate control waveforms for switches in order to control signal transmission polarization for both CW and WB modes. Second function is to trigger the DDS units with two trigger signals which have a fixed time delay between them. Third function is to feed the second IF units with a 70 MHz clock. The first two functions are accomplished by coding in Verilog and programming the FPGA using Quartus II and

the third function is done by adding a frequency converter inside the unit that generate 70 MHz clock from 10 and 80 MHz clock of the clock source.

The FPGA board is a commercial FPGA training platform which contains an Altera Cyclone IV EP4CE6E22C8N chip. It has 6272 logic elements and maximum 179 user I/O which provides enough capability for programming to achieve the necessary functions [7]. In order to generate control wave forms for polarization switches, one of the 10 MHz outputs from the clock source is connected to the FPGA as a clock input and a frequency divider is programmed to generate a low frequency TTL output based on the 10 MHz clock to control the switches inside amplification unit and the transmitter unit. The transmission pattern then is set to four sections with the same time duration: “Vertical, Horizontal, Off, Off”, for clarifying and simplifying when processing the saved data. By changing the parameters of the frequency divider and connections at the front panel of the control unit, the transmitting time duration could be changed for each polarization and if necessary, transmission pattern can be changed to always on for one specific polarization or remove the “Off” sections and change to “Vertical, Horizontal” alternately.

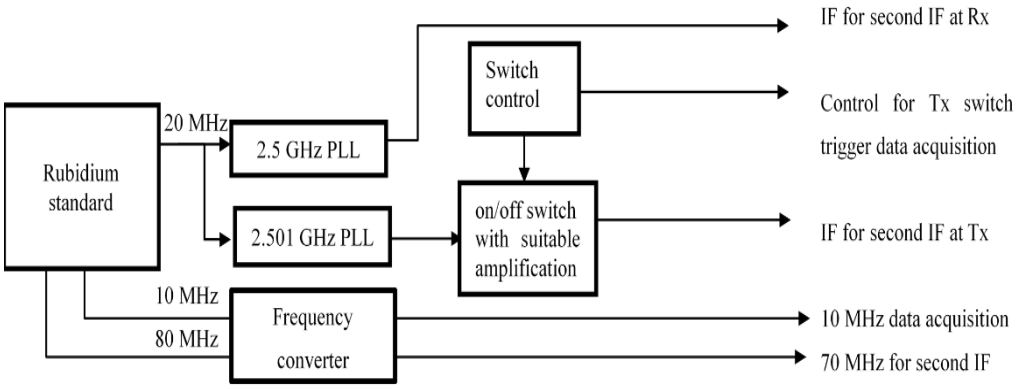

Figure 3.7 Block Diagram for CW mode before second IF

To generate the trigger signals for the DDS units with fixed time delay, the referencing signal from one DDS unit is connected to the FPGA as an input of the frequency divider. The reason not to use clock source as input is because the mechanics of sweep generation of the DDS chip is binary based. Due to this limitation, the

frequency of a sweep is increasing by steps and could cause problems when subtract one from the other at the end of data acquisition if the start of each sweep is not aligned with the working clock of the DDS chip. To avoid this potential risk, the referencing signal is used as the input. By setting the time delay by integer times of the referencing signal's period time, the start times of sweeps generated by the DDS units are synchronised with the working clock of the DDS units. Also the time delay between triggers could be re-programmed to move the spectrum of received signal to different frequencies, however the value is fixed at 4 MHz for K-band and 12 MHz for E-band to get a clean spectrum and reduce the sampling frequency and the size of data. For extensions and upgrading purpose of potential remote sites, a function to align the trigger generation to the Pulse Per Second (PPS) of Global Positioning System (GPS) is added in the program. It will give higher reliability for data transmission between two sites.

.

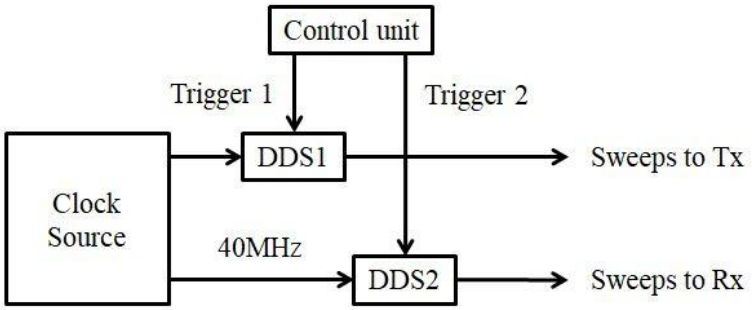

Figure 3.8 Block Diagram for WB mode connections

Two buffer chips are added between the ports on the front panel and FPGA board to protect FPGA from over driving and damaging the FPGA chip. A switch is added on the front panel to change different working modes without re-programming the FPGA and make adjustments on cables and connections. The Verilog program of the FPGA will be listed in appendix.

3.2.4 Transmitter

The transmitter unit contains two parts, second IF unit to up-convert the signal

frequency from 2 to 3 GHz to 12-18 GHz, RF unit to up-convert the signal from 12-18 GHz to 24 GHz for K-band and 72 GHz for E-band and suitable antennas to transmit the signal.

A commercial microwave wideband synthesizer ADF5355 is used as the frequency up-converter in this project [8]. With the 70 MHz output of the control unit as a referencing signal, the Voltage-Controlled Oscillator (VCO) could up-convert the 2.5 GHz signal, either for CW mode or WB mode, to 12 GHz to 18 GHz frequency range. The frequency band and the output power level of the VCO are programmable to give flexibilities to reach different frequencies. The RF units for the E-band and K-band were built in Durham University as well, the E-band unit contains a frequency multiplier which multiplies the signal frequency by 6 times and for the K-band unit a multiplied by 2 frequency multiplier is mounted inside. The frequency changing is showed in the Figure 3.8:

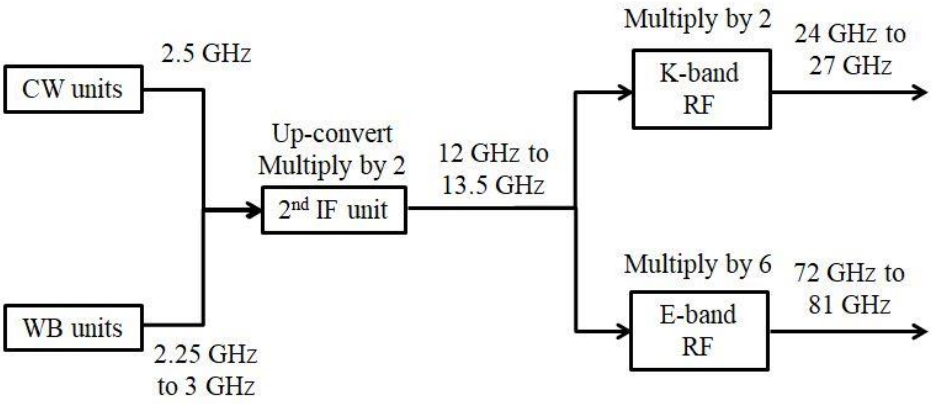

Figure 3.9 Diagram of frequency up-converting

Figure 3.9 shows the inside installation and front view of the transmitter.

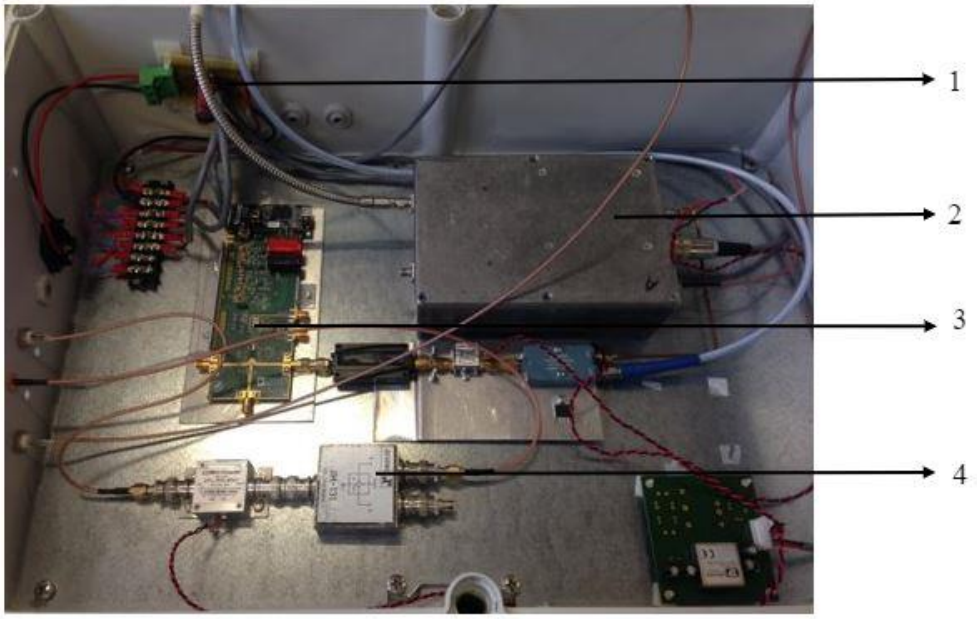

Figure 3.10 Inner view of transmitter

1: Power module, 2: RF unit for K-band transmission, 3: Second IF unit 4: Splitter

Figure 3.11 Installed view of transmitter

1: E-band antennas for both polarizations, 2: Dual-polarization antenna for K-band, 3: Second IF unit

The plastic box is weather-proofed and gets power from an indoor power supply. The components are mounted on a metallic plate which is fixed inside the plastic box. A bag of desiccant is placed inside the box to absorb water vapour and small holes are

drilled at the bottom of the box in order to avoid liquefaction of water vapour and damage the components. These boxes are then mounted on a metallic frame on the roof of the Engineering Department, Durham University.

The part number of antennas used for the E-band is Ainfoinc LB-12-10. These single polarization antennas are suitable for frequency range from 60 GHz to 90 GHz and have 12 dB gain and 45 degrees beam width at the operating frequency [9]. Two antennas are connected to the E-band RF unit for vertical and horizontal polarization respectively and mounted in parallel on the box with the same height to the ground. For K-band, antenna from Ainfoinc is used. The part number is LB-SJ-180400. This antenna is a dual polarization horn antenna working between 18 GHz to 40 GHz with 10 dB gain and 55 degrees beam width at the operating frequency [10]. Vertical and horizontal polarization ports of the antenna are connected with standard RF cables to the RF unit of the K-band. The K-band antenna is mounted at the middle on the front panel of the weather-proofed box.

All the antennas are weather-proofed with radomes made of plastic foam. However, to make a better weather-proofing effect, several pieces of fabrics are coated with super hydrophobic material and covered the front of the antennas. The fabrics are tested in the lab first to prevent possible attenuation on radio wave propagation. When rain hits the fabric cover, water tend to gather to a lager drop and fall to the ground quickly so that the influence of antenna wetness will be reduced. Figure 3.11 shows the installation for the super hydrophobic cover on the E-band antenna for the transmitter.

Figure 3.12 Weather-proofed fabrics with super hydrophobic coating

3.2.5 Receivers

Two receivers are assembled for this project for the main link and side link respectively. Similar with the transmitter, it also contains a second IF unit to up-convert the signal frequency from 2 to 3 GHz to 12-18 GHz and two RF units to up-convert the signal from 12-18 GHz to 24 GHz for K-band and 72 GHz for E-band for both the main link and the side link. One difference between transmitter and receivers setting up is the output from the second IF unit is feeding both the main link and side link receivers. The main link receiver is a dual polarization receiver and the side link receiver is only working on the vertical polarization. The weather-proofed case and antennas are identical with the transmitter. Figure 3.12 shows the installed view of the main link receiver.

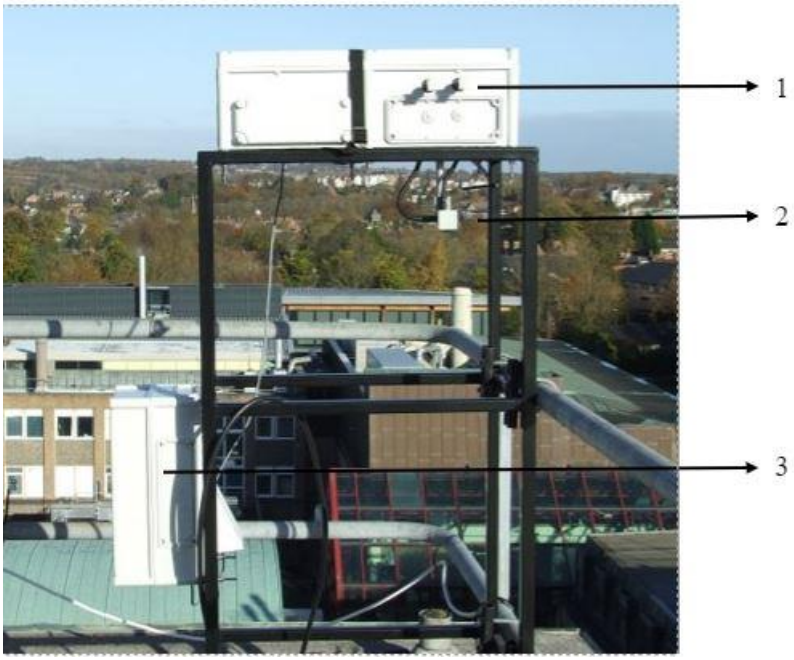

Figure 3.13 Installed view of main receiver

1: E-band antennas for both polarizations,
2: Dual-polarization antenna for K-band, 3: Second IF unit

There are 6 different received signals: vertical and horizontal signals for the E-band and K-band at the main link receiver and vertical signals at the side link. Because of the high frequencies of the transmitted signal, it is hard for the data acquisition card to sample and record the data at their original frequencies, which are around 25 GHz and 77 GHz. In this case, mixers and Low Pass Filters (LPF) are added in the receivers. The received signals are first mixed with signals which have a small difference in frequency, and then the mixed signals are led through a LPF to get the lower peaks of the spectrum. The frequency difference is set on CW mode and WB mode and fixed. After that, the lower frequency signals (base band signals) are connected to the data acquisition card for recording and further processing.

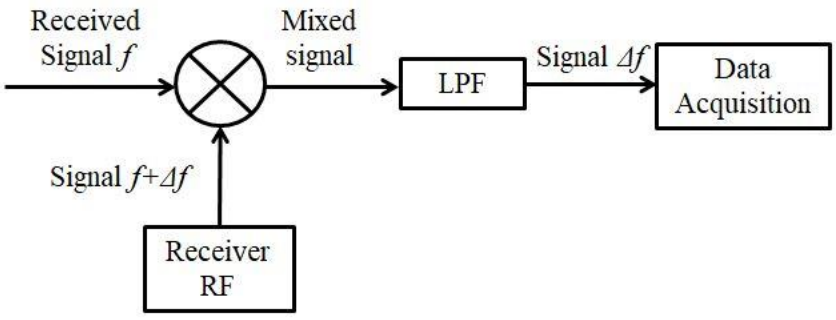

Figure 3.14 Block diagram of receiving procedure

3.2.6 Data acquisition

A workstation with two data acquisition cards installed is placed at the plant room on the roof to save the received data. The part number of the data acquisition cards is PX14400. It is a dual channel data acquisition card with a highest sampling rate of 400 MHz [11]. As mentioned in 3.2.5, there are 6 receiving signals that need to be record from the receivers. Because the frequencies of the received signals are different (4 MHz for K-band and 12 MHz for E-band), three combiners are used to reduce the number of inputs to the data acquisition cards to three. For the main receiver and side receiver, the E-band received signals and K-band received signals with the same polarization are combined together as an input to one of the channels. The cards are working on Master-Slave mode and both channels of master card are connected to the signals for the main receiver and one channel of the salve card is used for the side receiver. Considering the size and the frequencies of the received signal, the master card is working with a 10 MHz reference clock from the rubidium at 40 MHz sampling rate and the slave card is getting the same sampling clock by bridging with the master card. Figure 3.14 shows the connections to the data acquisition cards.

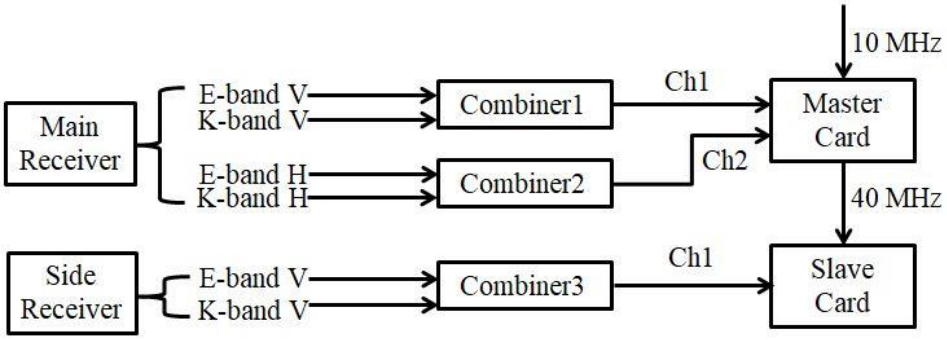

Figure 3.15 Block diagram of data acquisition connections

The signals received by the data acquisition card are transferred to the workstation by Peripheral Component Interconnect (PCI) bus. It could be monitored in both time domain and frequency domain at the workstation with the supporting software. The software also gives manual save function to save real-time data by certain time duration. However it does not give a function of automatically saving data at certain time. So an

application is written in C language to take control of the data recording. The application successfully achieves the function of recording data every minute and saves them into a certain folder and name them by numerical order. At the start of each minute, the received signal is collected for 1 second time duration and saved as an independent file for further processing using other software like Matlab. The figure below shows the frequency spectrum of the received signal in the CW mode after processing.

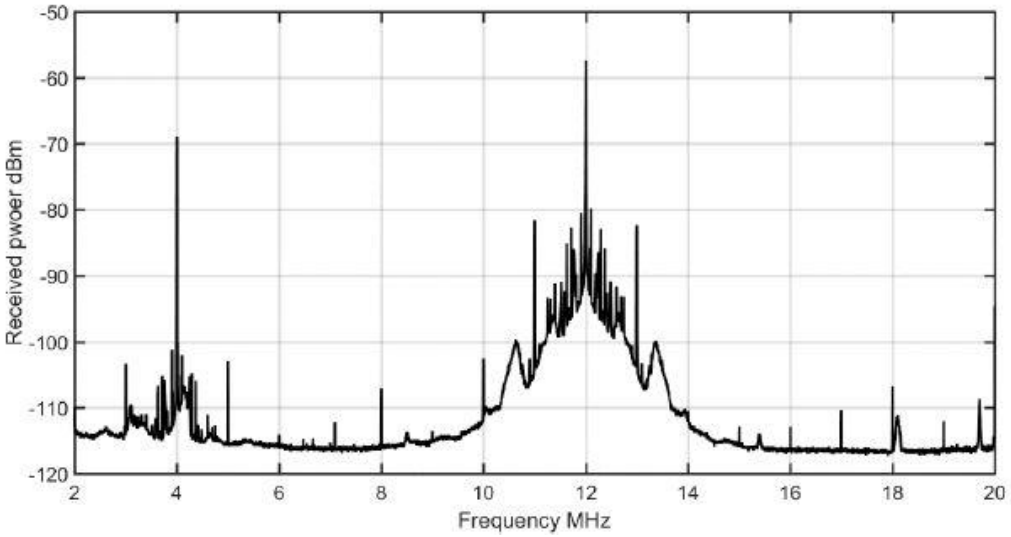

Figure 3.16 Frequency spectrum of received signal for one channel

3.2.7 Advantages and innovations of the Channel Sounder

This channel sounder has tremendous advantages compared to other competitors because of its wide bandwidth, high resolution, high sensitivity and dynamic range, and flexible configurability. It supports a continuous bandwidth of 750 MHz (covering 250 MHz–1 GHz and 2.2 GHz–2.95 GHz), significantly exceeding traditional spectrum analysers and software-defined radio platforms. Its temporal resolution could be as high as 204.8 μs which enables detection of short-duration signals, outperforming conventional spectrum analysers whose resolutions are around second-level and earlier channel sounders and its frequency resolution of 200 kHz could effectively distinguish narrowband signals and avoiding possible overestimation in frequency domain. Its ability to detect signals weak to -90 dBm and an instantaneous dynamic range larger than 29 dB surpass most of the commercial devices.[6]

3.3 Fixed Link Design

According to ITU recommendations, the measurement should last for at least one year in order to get statistical reliable results [12]. So the transmitter and receivers are fixed and mounted on the roof of Department of Engineering, Durham University for a long-term measurement. Two links are designed, a main link to study the attenuation and depolarization effect and a side link to study the scattering effects. Figure 3.16 shows the diagram of the fixed links.

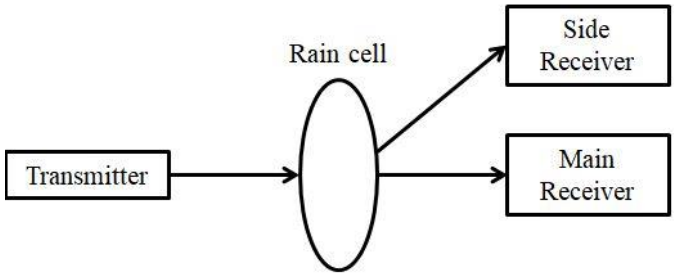

Figure 3.17 Diagram of main link and side link

The idea of the link design depends on several aspects. Firstly the links should be better mounted on a university owned property so that it is easy to get access to for data collections and maintenance. Secondly the main link should be a clear Line-Of-Sight (LOS) link without any blockage in the middle of the propagation route of the signal, so the attenuation will be introduced by precipitation events only besides the free space path loss. Finally the side link should be a None-Line-Of-Sight (NLOS) link to make sure the results of measured signals are only provided by the scattering effect by rain cells. Considering of all the requirements above, the links are set as the photo shows in Figure 3.17.

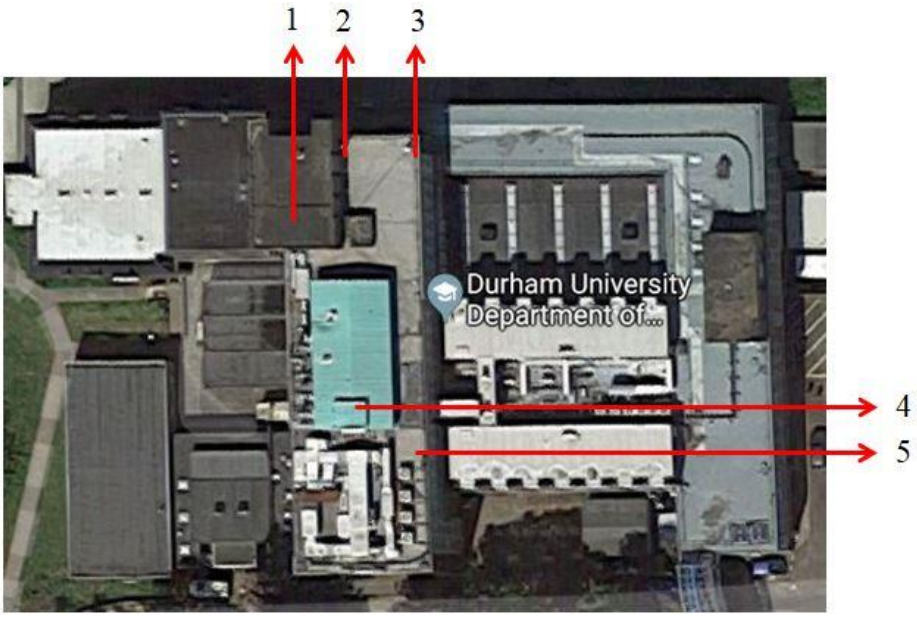

Figure 3.18 Satellite photo of the measure system [13]

1: Plant room A, 2: Side receiver, 3: Main receiver, 4: Plant room B, 5: Transmitter

All the devices before the second IF units are placed in the plant room A and the workstation with data acquisition cards is place in plant room B in Figure 3.17. It provides a convenient location for the technicians to maintain the system. The distance between the transmitter and main receiver is 35 metres and the distance between the main receiver and side receiver is 7 meters. With the relative short distance of the links, the rain drops could be considered uniformly distributed along the propagation path which makes it easy for data processing and modelling. The height and facing direction of the transmitter and main receiver are finely adjusted to make sure the receiving signal power level reaches highest for co-polarization transmission and reduce the influence caused by alignment on cross-polarization transmission. For the side receiver, the facing direction is also adjusted to make sure it receives the pure scattered signals by the rain cell without any direct signals directly form the transmitter. The longest distance for signals to travel along cables is around 50 metres, in order to secure the reliability of the systems. High quality cables are used for the connections between units and all the connectors are protected by water-proofed tape.

3.4 Summary

This chapter described details of the experimental setup employed in this research, encompassing the implementation of radio propagation measuring and meteorological data acquisition equipment. A significant amount of work was dedicated to ensuring the accuracy and reliability of the entire experimental system, with a focus on both hardware design and software programming aspects.

For meteorological data recording, a PWS100 laser disdrometer was installed on the roof top of the Bill Bryson Library. This device was tasked with collecting comprehensive meteorology data, including rain rate, temperature, rain drop speed, and rain drop size distribution. The weather sensor was assembled with a laser generator, two laser sensors, and an embedded digital signal processor. The data collected were initially processed and then transferred to a CR1000 data logger and further to a workstation through a wireless network. LoggerNet software, installed on the workstation, was utilized to control data collection, monitor the weather station's working status remotely, and save the data in a format suitable for further analysis. A custom program was written in CRBasic language to configure the weather station to collect data every minute.

For attenuation measurements, an advanced channel sounding system was utilized. This system consisted of multiple components, each of which required careful setup and calibration. A rubidium clock served as the clock source, generating a global clock for the system and being multiplied and amplified into 10 different phase - coherent reference clocks. Two sets of phase lock loops were prepared to generate either continuous waveform or chirp signals for wide band measurements. An FPGA which programmed to control signal transmission polarization was embedded in the control unit, trigger the DDS units, and provide a 70 MHz clock to the second IF units.

The transmitter unit was designed to up convert the signal frequency to the desired bands. It incorporated a commercial microwave wideband synthesizer and custom built RF units for the E-band and K-band. The antennas used for transmission were carefully selected and weather proofed to minimize the impact of environmental factors. Similar

to the transmitter, the receivers were designed to receive and process the signals. Mixers and Low Pass Filters (LPF) were added to down convert the high frequency received signals for data acquisition.

A fixed link was designed according to ITU recommendations to ensure statistical reliability. Two links, a main link for studying attenuation and depolarization effects and a side link for studying side scattering effects, were set up on the roof of the Department of Engineering. The distance between the transmitter and main receiver was 35 metres, and the distance between the main receiver and side receiver was 7 meters. The height and facing direction of the transmitter and receivers were finely adjusted to optimize signal reception, and high quality cables were used for connections, with all connectors protected by water proofed tape.

3.5 References

[1] "PWS100: Present Weather Sensor", 2019. [Online]. Available: https://www.campbellsci.eu/pws100. [Accessed: 25- Feb- 2019].

[2] A. Gires, I. Tchiguirinskaia and D. Schertzer, "Two months of disdrometer data in the Paris area", Earth System Science Data, vol. 10, no. 2, pp. 941-950, 2018. Available: 10.5194/essd-10-941-2018.

[3] "CR1000: Measurement and Control Datalogger", 2019. [Online]. Available: https://www.campbellsci.eu/cr1000. [Accessed: 25- Feb- 2019].

[4] "LOGGERNET: Datalogger Support Software", 2019. [Online]. Available: https://www.campbellsci.com/loggernet. [Accessed: 20- Apr- 2019].

[5] "PRS10 - Rubidium Frequency Standard", Thinksrs.com, 2019. [Online]. Available: https://www.thinksrs.com/products/prs10.html. [Accessed: 25- Feb- 2019].

[6] CHEEMA, ADNAN,AHMAD (2015) Homogeneous Test-bed for Cognitive Radio, Durham theses, Durham University. Available at Durham E-Theses Online: http://etheses.dur.ac.uk/11209/

[7] Altera Corporation, Cyclone IV Device Handbook, Volume 1, Chapter 1. 2016.

[8] Analog Devices, ADF5355 Data Sheet. 2017.

[9] Ainfonic, LB-12-10 Data Sheet. 2017

[10] Ainfonic, LB-SJ-180400 Data Sheet. 2017

[11] "PX14400A – 400 MS/s, 14 bit, AC Coupled, 2 Channel, Xilinx Virtex-5 FPGA, PCIe x8, High Speed Digitizer Board", 2019. [Online]. Available: http://www.signatec.com/products/daq/high-speed-fpga-pcie-digitizer-board-px14400.html. [Accessed: 25- Apr- 2019].

[12] Recommendation ITU-R P.536.17: "Propagation data and prediction methods required for the design of terrestrial line-of-sight systems" ITU-R P. Ser., Geneva, Switzerland, ITU International Telecommunications Union, 2017

[13] "Google map", 2019. [Online]. Available: https://www.google.com/maps/@54.7673422,-1.5708595,127m/data=!3m1!1e3. [Accessed: 11- May- 2019].

Chapter4 Precipitation Analysis

In this chapter, analysis for different type of precipitation events is given. Not only annual statistics are focused on, but also specific events with identical characteristics are discussed. Comparisons are made among such events to make sure enough information has been considered.

4.1 Annual Statistics Analysis

The system introduced in chapter 3 was used for a long-term measurement which started from January 2018. Based on the requirement of the ITU recommendation [1], at least one year of data needs to be considered in order to get reliable statistical results. The data collected from January 2018 to January 2019 are processed at a high standard to meet the submission requirements of the ITU Study Group 3 databanks (DBSG3) and contribute to evaluation of statistics of rain intensity, rain event duration and rain drop size distributions [2].

4.1.1 Rain intensity

Rain intensity is a standard parameter to describe rain events and a widely used parameter for rain attenuation research because it shows intuitively how strong a rain event is. As a result, the majority of models that were discussed in chapter 2, use rain intensity as an input for the calculation of attenuation. Figure 4.1 shows the rain intensity over the 2018-year period on different dates.

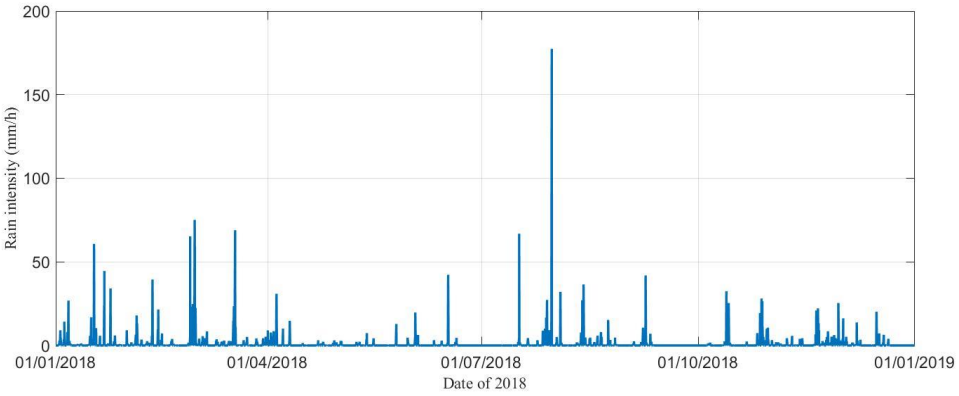

Figure 4.1 Rain intensities across 2018

To study the statistical properties of rain intensity, complementary cumulative distribution functions (CCDF) of rain intensity are the basic tool to use for a time scale of years. It has become a vital index for the prediction of attenuation by rain to a radio wave communication system [3].

In probability theory and statistics, the CCDF of a real-valued random variable X is given by equation 4.1 [4]:

$$F_x(x) = P(X > x) \tag{4.1}$$

where the right side of the equation represents the probability that the random variable X is larger than x. When applied to rain intensity analysis, the CCDF of rain intensity R evaluated at values of P stands for the probability that R will take a value larger than P. Figure 4.2 shows the CCDF curves from January 2018 to December on a monthly basis.

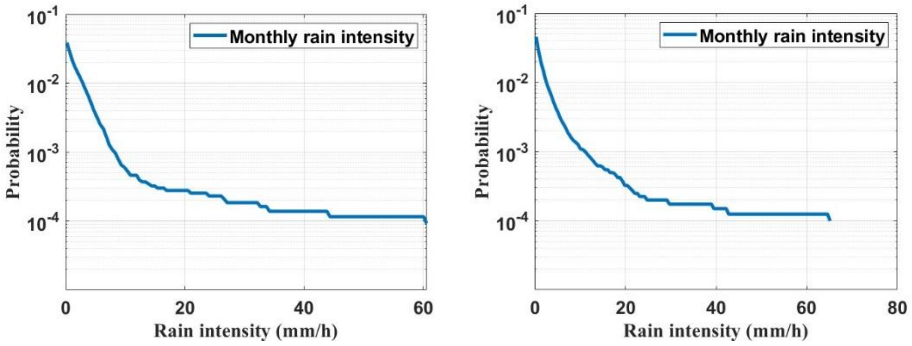

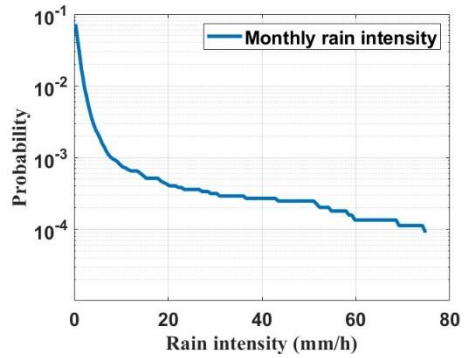
Monthly rain intensity
Probability
Rain intensity (mm/h)

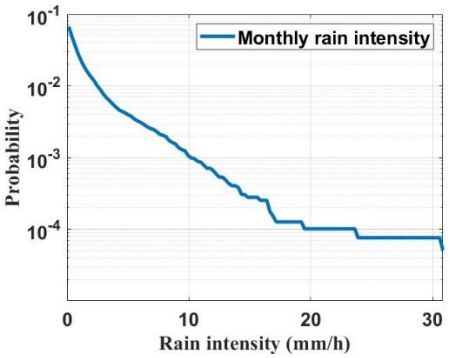
Monthly rain intensity
Probability
Rain intensity (mm/h)

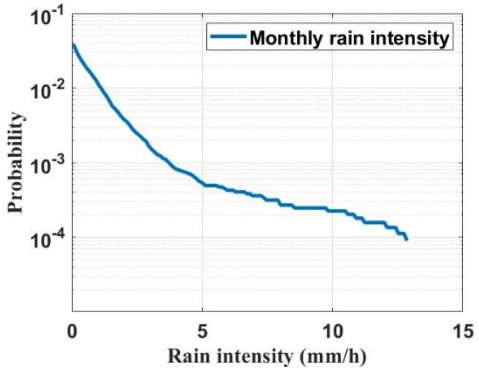
Monthly rain intensity
Probability
Rain intensity (mm/h)

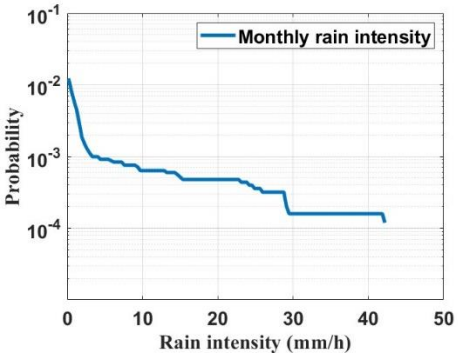
Monthly rain intensity
Probability
Rain intensity (mm/h)

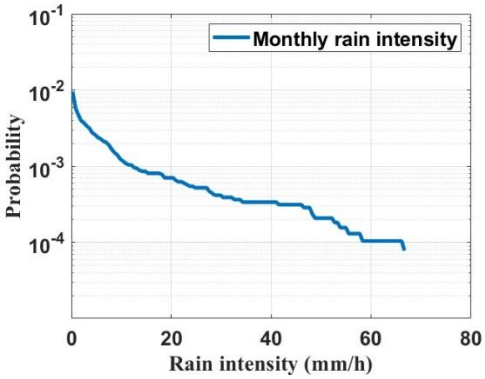
Monthly rain intensity
Probability
Rain intensity (mm/h)

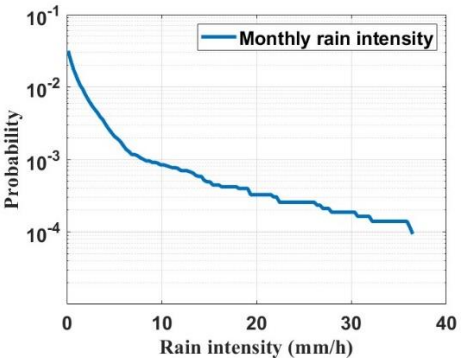
Monthly rain intensity
Probability
Rain intensity (mm/h)

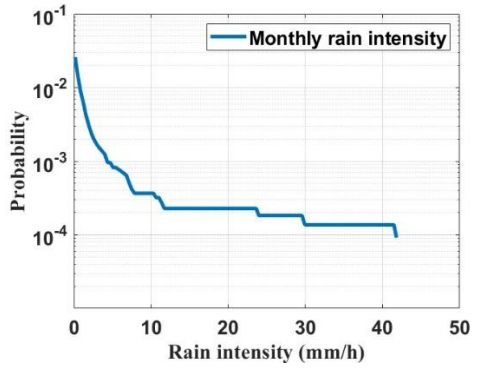
Monthly rain intensity
Probability
Rain intensity (mm/h)

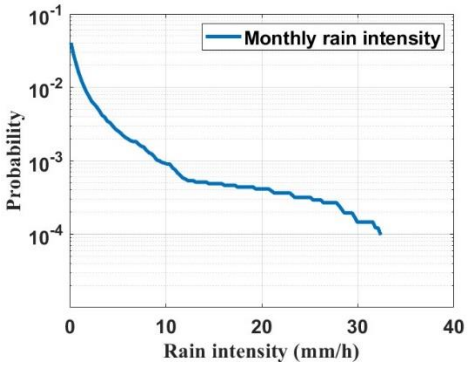
Monthly rain intensity
Probability
Rain intensity (mm/h)

Monthly rain intensity
Probability
Rain intensity (mm/h)

Monthly rain intensity
Probability
Rain intensity (mm/h)

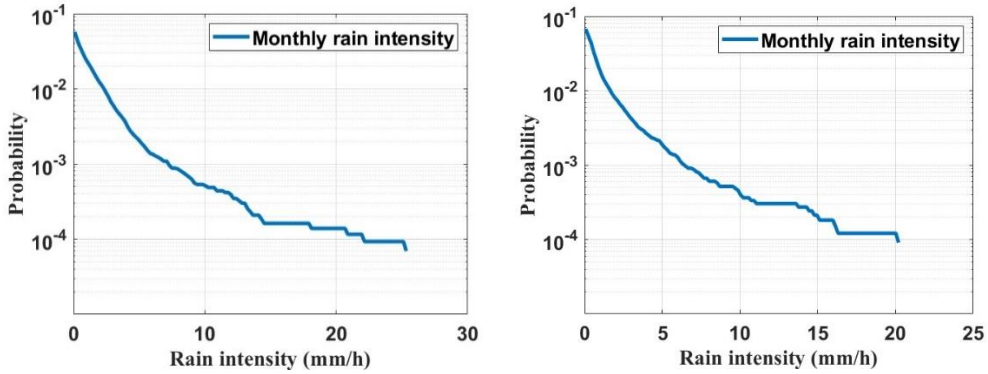

Figure 4.2 CCDF curve from Jan 2018 to Dec 2018

From the figure the rain intensities distribution for each month in 2018 can be observed. To design a communication system with high reliability, the worst case of a year with a highest exceeded probability needs to be considered to ensure that the system has reliable working condition for more than a certain percentage of time (95% to 99.9%). For that purpose, the worst month analysis and annual rain intensity analysis are needed. Annual rain intensity analysis sums the rain events all year and give a result from abundant samples.

The definition of a worst month is given in ITU-R P.581.2 [5]. For rain intensity analysis, is for a preselected threshold of rain intensity CCDF, a month of a year in a period of twelve consecutive calendar months has the longest time which the threshold is exceeded for. That month is then the worst month of the year with respect to rain intensity. It should be noticed that the worst month could be different for different kinds of parameters and even for the same type of parameters, depending on the values of the thresholds. Thus, the worst month is not necessarily the same month. Figure 4.3 shows the CCDF curves of annual rain intensity and worst month. For most of the time, the maximum rain intensity is less than 70 mm/h in year 2018. The worst month happened in July 2018 with a maximum rain intensity that exceeds 150 mm/h.

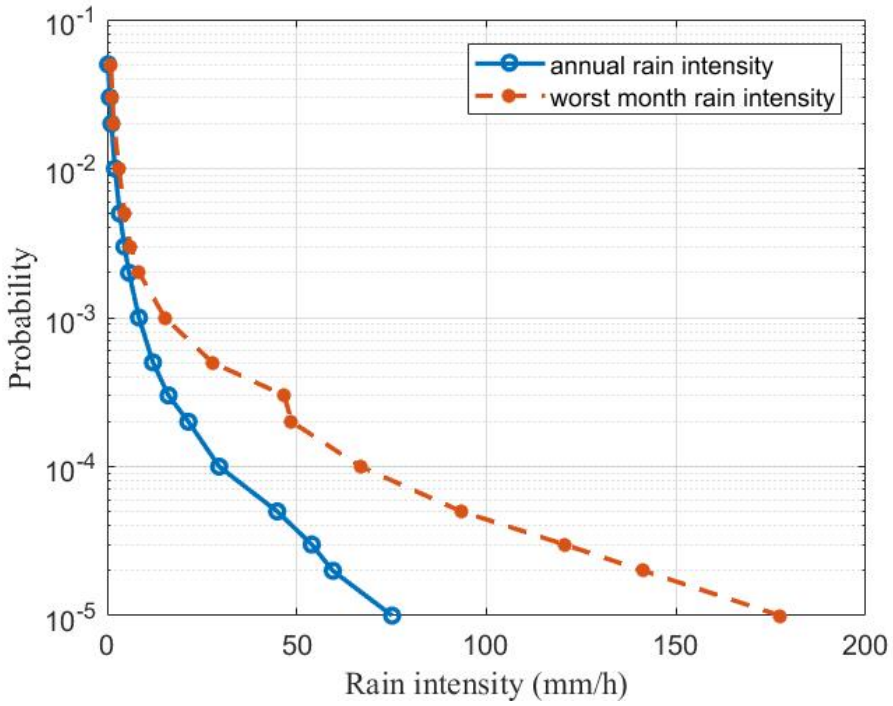

Figure 4.3 CCDF curves of the yearly rain intensity and worst month rain intensity

4.1.2 Rain duration

The time duration of rain events is another important parameter for rain statistical analysis. The relationship between rain intensity and duration is usually inversed which means a long duration precipitation event is more likely to have a low intensity. However, with the global climates changing, the uncertainty of rain durations and return period is increasing [6]. It makes rain duration statistics a more vital value to record and analyse. Although data sets from one-year observation is not enough to make predictions, the time duration information is still valid and helpful to understand the features of rain events. Figure 4.4 indicates the total duration of rain events across year 2018 at different rain intensities.

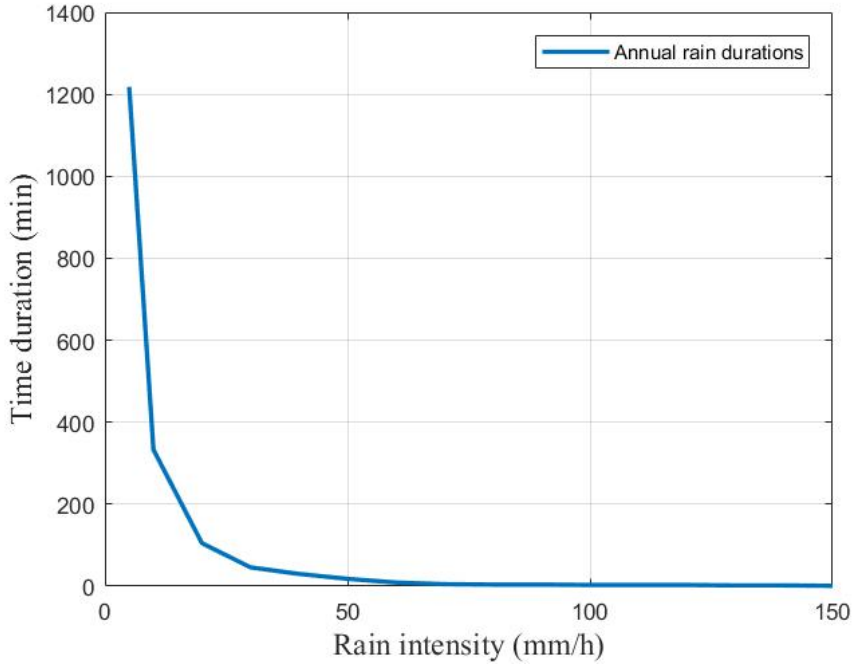

Figure 4.4 Total rain duration of 2018 on different rain intensities

The total time duration of rain events observed in year 2018 with the rain intensities lager than 0.2 mm/h is 24931 minutes. The rain intensities are separated into 16 different bins with 10 mm/h bin width. From the figure, it can be seen that during the majority of the time, rain intensity is less than 50 mm/h. With the intensity increasing, the time duration decreases.

In addition to the time duration of rain events, the number of rain events across the year 2018 is analysed. The definition of rain events adopted in this study is if there are consecutive minutes of data with rainfall detected between two minutes of data without rainfall detected, these consecutive minutes are combined as an individual rain event. The total number of rain events with average rain intensity higher than 5 mm/h is 420. Among all the rain events, the same trend is found similar with the rain durations, 60% of total detected rain events have average rain intensity between 5mm/h to 10 mm/h. Only 7% of total rain events have average rain intensity higher than 40 mm/h. The pie chart in Figure 4.5 shows the percentages of rain events related to different rain intensity range.

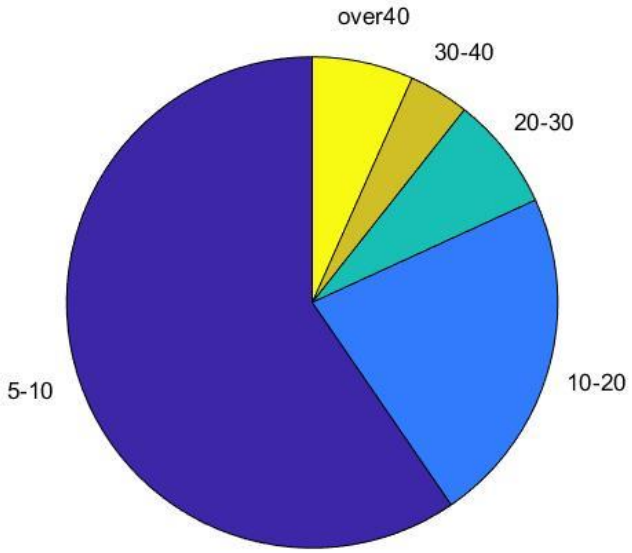

Figure 4.5 Rain events in different intensity catalogues (mm/h)

4.1.3 Rain drop size distributions

Rain drop size distribution is a powerful tool for precipitation research and attenuation models based on DSD as discussed in chapter 2. It is the distribution of the number of rain drops based on their size. It gives detailed and micro-structure information while rain intensity gives information of general strength. In the collected weather data, the number of raindrops is recorded and separated into 300 slots based on diameter differences. Each slot has a slot size of 0.1 mm. A total of 300 slots cover a diameter range from 0.1 mm to 30 mm.

The DSD can be calculated using equation 4.2:

$$N(D_i) = \sum_{j=1}^{300} \frac{n(D_i, v_j)}{v_j} \cdot \frac{1}{S \cdot \Delta t \cdot dD_i} \tag{4.2}$$

where S = 40 cm^2 is the measurement surface of the laser beam of the PWS100 disdrometer, Δt = 60 s is the integration time for one minute, $n(D_i, v_j)$ is the number of rain drops with average diameter D_i (mm) and average speed v_j (m/s), and dD_i(mm) is the bin width associated to the diameter D_i. Appropriate unit conversions

are implemented to deliver the result in $(\mathrm{m}^{-3}\mathrm{mm}^{-1})$.

The average velocity of all particles at each minute has been recorded. However, the velocities of each particle are not. As a result, the theoretical relationship between the terminal fall velocity and the drop diameter is adopted for the DSD computation to estimate the falling speeds for drops with different sizes. Specifically, the following relation is used:

$$v(D_i) = \begin{cases} 3.78D_i^{0.67}, & D_i < 0.8 \\ 9.65 - 10.3e^{-0.6D_i}, & D_i \geq 0.8 \end{cases} \tag{4.3}$$

which is a combination of two widely used equations to achieve a nonnegative and monotonous relation between drop diameter and the terminal fall velocity [7]. Figure 4.6 shows the DSD from January 2018 to December 2018 on a monthly basis with drop diameters between 0.05 mm to 10 mm.

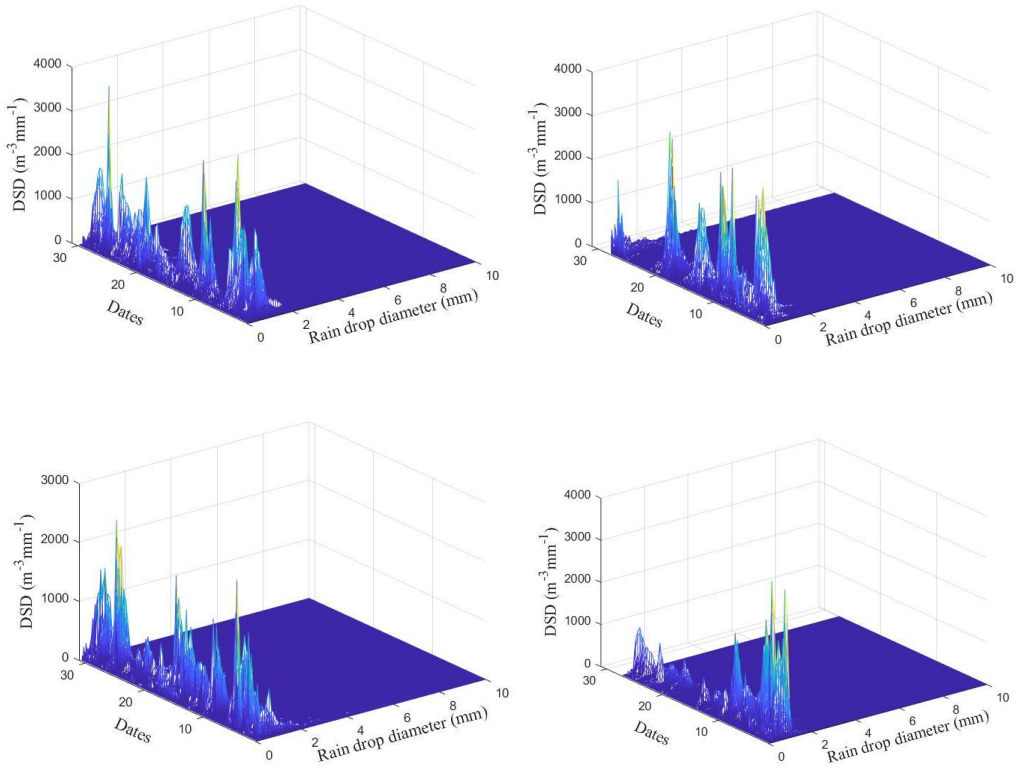

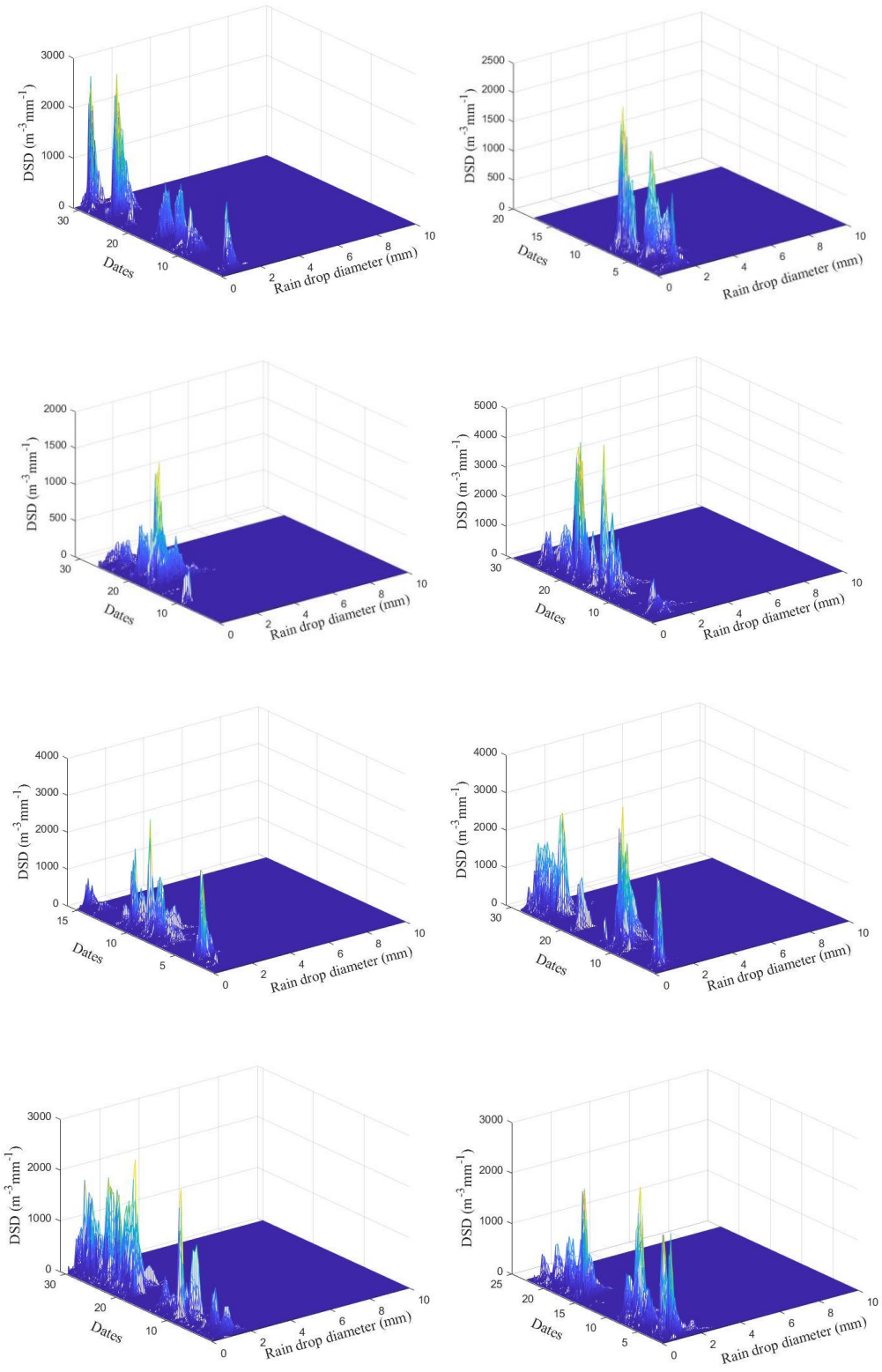

Figure 4.6 DSD on a monthly basis across year 2018

Figure 4.7 shows the total DSD across year 2018 intensities with the diameters of rain drops between 0.05 mm to 10 mm. The peak DSD achieves around rain drop size of 0.7 mm.

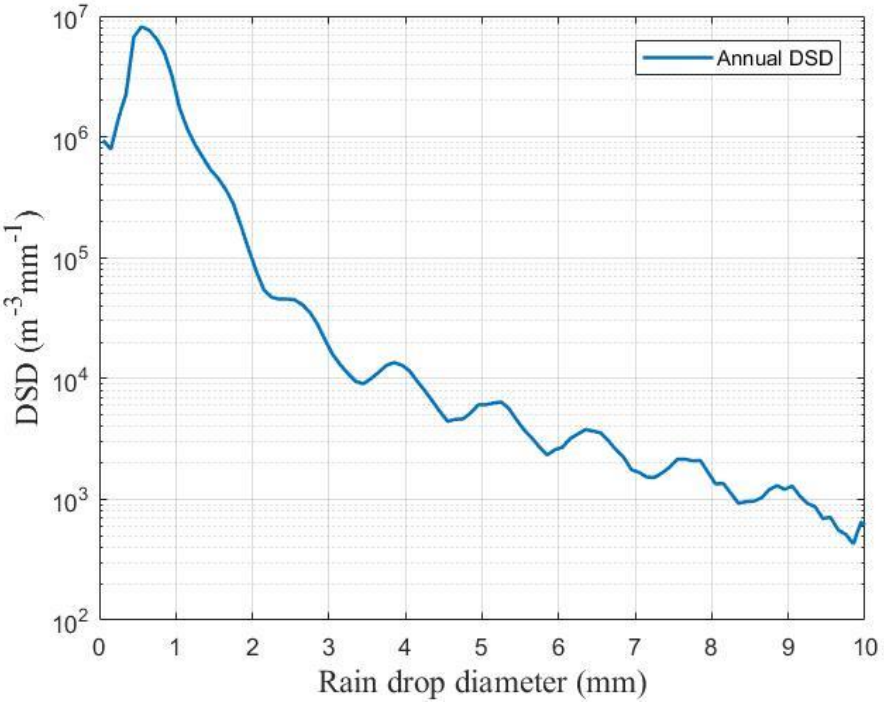

Figure 4.7 Total DSD across year 2018

Figure 4.8 shows the rain DSD under different rain intensities.

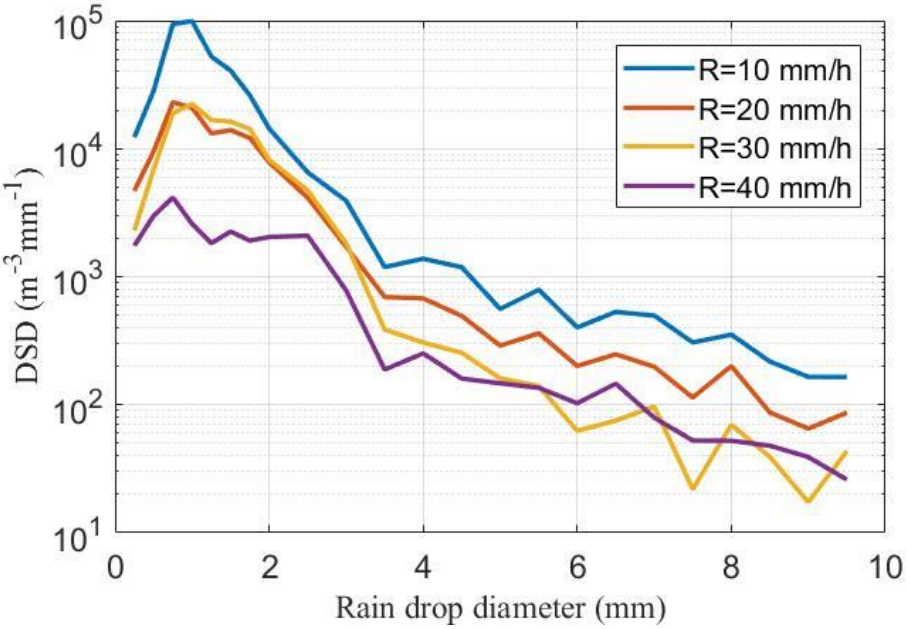

Figure 4.8 DSD under different intensity year 2018

4.2 Drop Size Distribution Analysis

Several different distribution models have been applied to simulate measured DSD,

in this part three of the existing models are compared: Marshall and Palmer Model (semi-experimental exponential distribution), log-normal distribution model and gamma distribution model (in which exponential distribution is a special case).

4.2.1 Marshall and Palmer distribution model

The first model introduced is the Marshall and Palmer Model or named exponential distribution model [8]. It was published in 1948 and has been used for years. The mathematical expression is given in equation 4.4:

$$N(D) = N_0 e^{-\Lambda D} \tag{4.4}$$

$$\Lambda = 41R^{-0.21} cm^{-1}$$

$$N_0 = 0.08 cm^{-4}$$

where D is the diameter, $N(D)$ is the number of drops per unit volume per unit interval of drop diameter D and R is the rain intensity. N_0 is the value of $N(D)$ for $D = 0$. The author estimated the values of N_0 and Λ based on historical data collected from Ottawa, Canada. Figure 4.9 shows the Marshall and Palmer distribution curve with different rain intensities

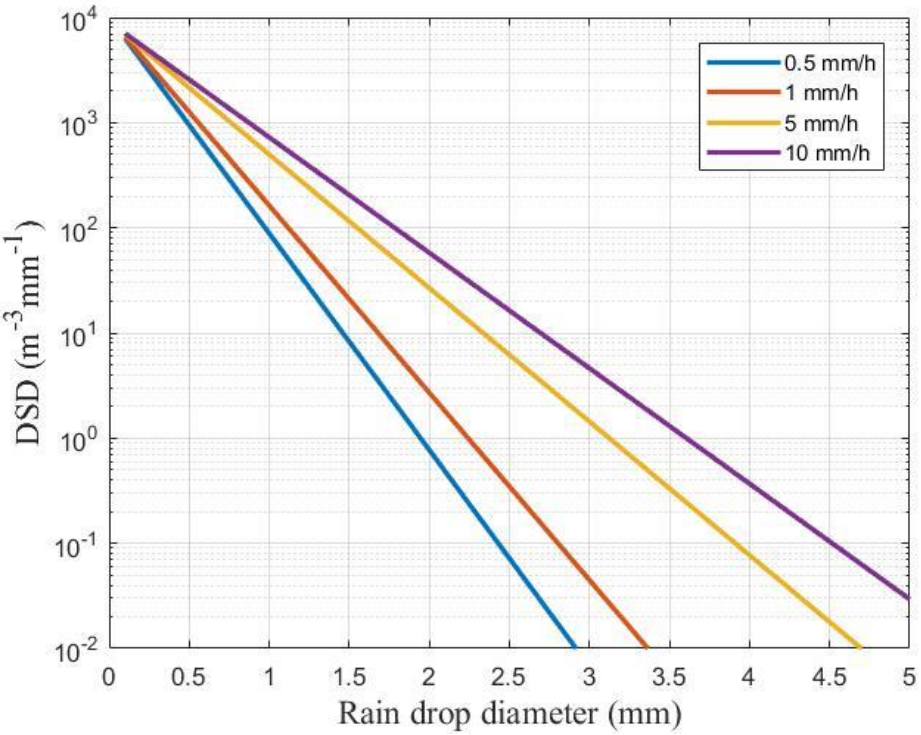

Figure 4.9 Marshall and Palmer distribution under different rain intensities

Though the exponential distribution model is relatively easy for calculations, it is not that accurate to present the account of small rain drops with diameters less than 1.5mm when compared to the Laws-Parsons data [9].

The Marshall-Palmer distribution model provides a simple way for understanding and analysing raindrop size distribution. However, it should be noticed that the empirical relationship between Λ and R might exhibit slight variations in the different observing locations. Furthermore, a single exponential distribution model may not be capable to present the full complexity of raindrop size distribution for specific rain types or under extreme weather conditions.

Figure 4.10 shows the comparison between the Marshall and Palmer estimated drop size distribution based on recorded rain intensities of May 2018 and the actual measured drop size distribution when particles' diameters are larger than 1.5 mm. it can be seen that the Marshall and Palmer fitting is relatively good with large drop sizes.

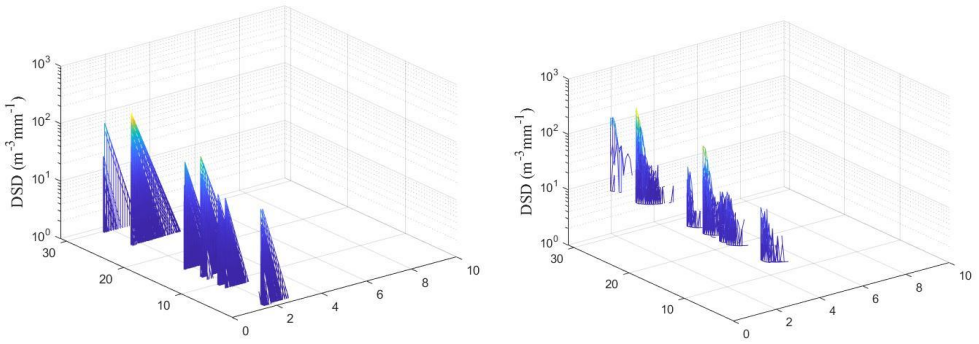

Figure 4.10 Comparison of Marshall and Palmer distributions (left) and measured DSD (right)

4.2.2 Log-normal distribution model

The log-normal distribution is a well-known positive unimodal statistical distribution. In general, a variable X is log-normally distributed if log(X-θ) is normally distributed with mean μ_g and standard deviation σ_g for some θ. When it is used to present the raindrop size distribution, θ=0 is often implemented and the distribution is multiplied by a scaling parameter. The log-normal distribution for the number of drops in each volume in the general form is given in equation 4.5:

$$N(D) = \frac{N_T}{\sqrt{2\pi}\sigma_g (D-\theta)} \cdot e^{-\frac{(\ln(D-\theta)-\mu_g)^2}{2\sigma_g^2}} \tag{4.5}$$

where N_T is the total number of drops per cubic metre and D is the diameter. It should be noticed that mean μ_g and standard deviation σ_g are geometric mean and geometric standard deviation [10]. It is also labelled as 3-P lognormal distribution means three-parameter lognormal distribution because of the three parameters above.

The log-normal distribution model for rain drop size distribution has advantages in mainly three aspects. Firstly, it is mathematically convenient since if the number of drops per unit volume per unit size category obeys lognormal distribution, then the higher moments of the distribution obey lognormal distribution as well. Secondly, the log-normal model captures the skewness of raindrop size distributions effectively, where there are many small drops, fewer medium-sized drops, and even fewer large drops. This skewness could be presented in the normal distribution of the log-transformed diameters. Finally, the three parameters used in equation 4.5 stand for

geometric average diameters, geometric standard deviations and total number of drops. This means that all these parameters have physical meanings. The several advantages for this distribution model to explain the fitting results of precipitation events are outlined in [11]. Figure 4.11 shows the fitted drop size distribution curves of the lognormal distribution model and the recorded drop size distributions for May, 2018.

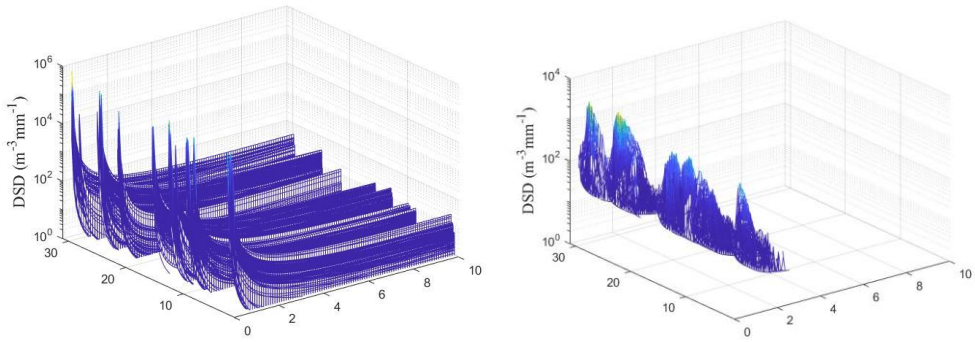

Figure 4.11 Comparison of lognormal distributions (left) and measured DSD (right)

It needs to be highlighted that the lognormal distribution curves are derived using equation 4.5 based on the measured data from the weather station. It is not directly fitting the measured data into a lognormal distribution.

4.2.3 Gamma distribution model

Another widely used distribution model is the gamma distribution. Early in 1984, *Ulbrich and Atlas* claimed that the gamma distribution performed better to present the rain drop size based on rain rate computation [12]. The expressions of gamma distribution model are given in equation 4.6:

$$N(D) = N_0 D^{\mu} e^{-\Lambda D} \tag{4.6}$$

where D is the drop diameter, Λ and μ are the slope and shape parameters, respectively. These parameters are used for adjusting the shapes especially the breadth of the distribution curves. If μ increases, the breadth of the drop size distribution will decrease. If Λ increases, the slope of the large size portion of the distribution will increase. These allow for the characterization of a wide range of precipitation scenarios. Also, it should be noticed that the exponential distribution is a special case of the

gamma distribution when μ=0. There is a disadvantage for this expression because the parameters do not have direct physical meaning since they are not related to any particular scaling. To solve this issue, several equations are given to relate the rain parameters and the gamma drop size distribution parameters. Here equations 4.7 to 4.9 could be used for computing these distribution parameters as proposed in [13]:

$$\Lambda = \frac{3.67 + \mu}{D_0} \tag{4.7}$$

$$\frac{D_m}{D_0} = \frac{4 + \mu}{3.67 + \mu} \tag{4.8}$$

$$N_0 = 6 \times 10^4 e^{3.2\mu} \tag{4.9}$$

where D_0 is the median drop diameter and D_m is the mass-weighted drop diameter. From equation 4.9 it could be found that in the gamma distribution model $N_0$is depending on the value of μ and the physical dimensions of N_0 vary with μ [14]. It has the risk of having unreal value of N_0 with high value μ (*i.e.* $\mu > 10$). To solve this problem, some modifications are proposed such as replacing the intercept parameter $N_0$with total number of particles N_T, however it can only partially reduce the influence. The normalized gamma distribution is considered as a more satisfactory presentation of rain drop size distribution. The formulations are given in equation 4.10 [15]:

$$N(D) = N_w f(\mu)(\frac{D}{D_m})^{\mu} e^{-(\mu+4)\frac{D}{D_m}} \tag{4.10}$$

where N_w, μ and D_m are the scaled intercept, shape, and mass-weighted mean diameter parameters, respectively. It can be calculated using the method of moments. The nth moment of the drop size distribution at time instant t is defined in equation 4.11:

$$m_n(t) = \int_0^{\infty} D^n N(D,t) dD \tag{4.11}$$

Substitution in the normalized presentation of gamma distribution, $D_m$and N_w can be calculated if N (D, t) is a gamma distribution from equation 4.12 and 4.13:

$$D_m = \frac{m_4}{m_3} \tag{4.12}$$

$$N_w = \frac{4^4 m_3^5}{6m_4^4} \tag{4.13}$$

f(μ), a function of the shape parameter, μ, is defined in equation (4.14):

$$f(\mu) = \frac{6(\mu+3.67)^{\mu+4}}{3.67^4 \Gamma(\mu+4)} \tag{4.14}$$

where Γ is the complete gamma function.

This normalized presentation of the gamma distribution model is very useful when comparing the shape of drop size distributions because it is dependent on two parameters. However, it should be noted that it just adjusts the used parameters, but the distribution itself is not changed.

4.3 Specific Precipitation Analyses

Three rain events in January 2018 are picked to analyse as these events exhibited differences on lasting time, rain rate and DSD. Rain events 1 and 2 happened on the 2nd of January from 10:40 to 14:30 and 20:00 to 23:55. Rain event 3 took place on the 3rd of January from 3:20 to 6:10. Figure 4.12 displays the diagrams that present the rain intensities changing with time for these three rain events:

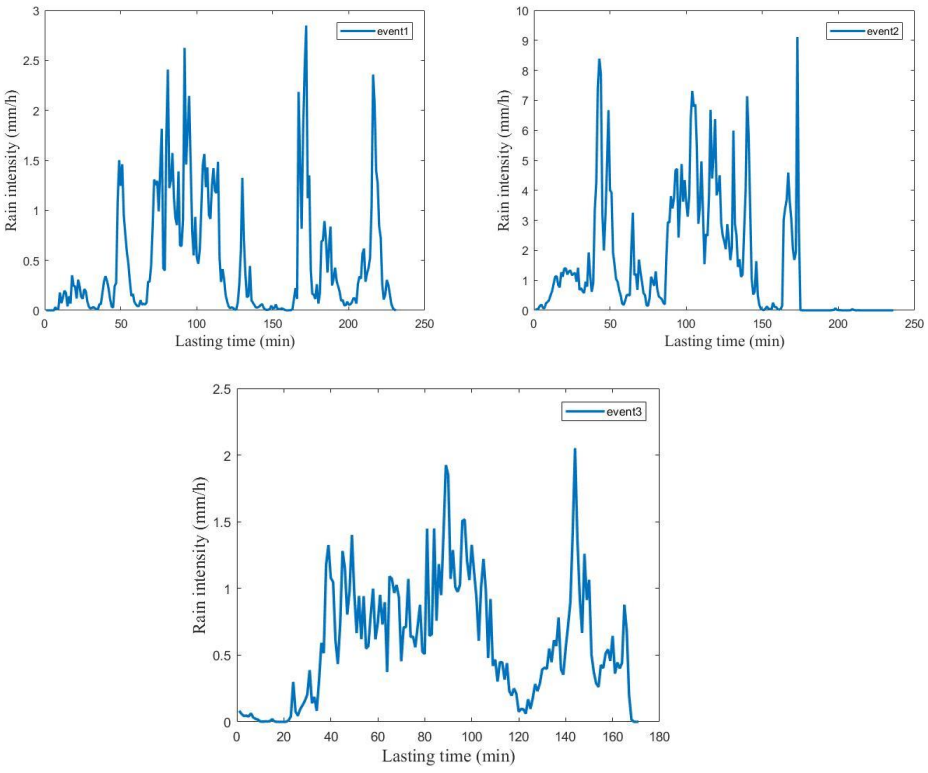

Figure 4.12 Rain intensities of three rain events of January 2018

Critical meteorology parameters are listed in table 4.1:

Table 4.1 Comparison of three rain events of January 2018

	Event 1	Event 2	Event 3
Lasting Time	230 minutes	235 minutes	170 minutes
Peak Rain Intensity	2.84 mm/hr	9.12 mm/hr	2.05 mm/hr
Average Intensity	0.5085 mm/hr	1.5816 mm/hr	0.6073 mm/hr
Standard Deviation	0.6371 mm/hr	1.9890 mm/hr	0.4558 mm/hr

Event1 lasted for 4 hours with a peak rain rate of 2.84 mm/hr, event 2 lasted for 4 hours as well with a peak rain rate of 9.12 mm/hr and event 3 lasted for 2.5 hours with a peak rain rate of 2.05 mm/hr. From the table, these three rain events were easy to distinguish as event 2 had quite stronger peak rain intensity and larger standard deviation while event 3 was changing smoothly.

Figure 4.14 shows the percentages of drops at different diameters. It indicates that most rain droplets of event 1 have smaller sizes around 0.5 mm and for events 2 and event 3 the diameters of raindrops are around 0.7 mm

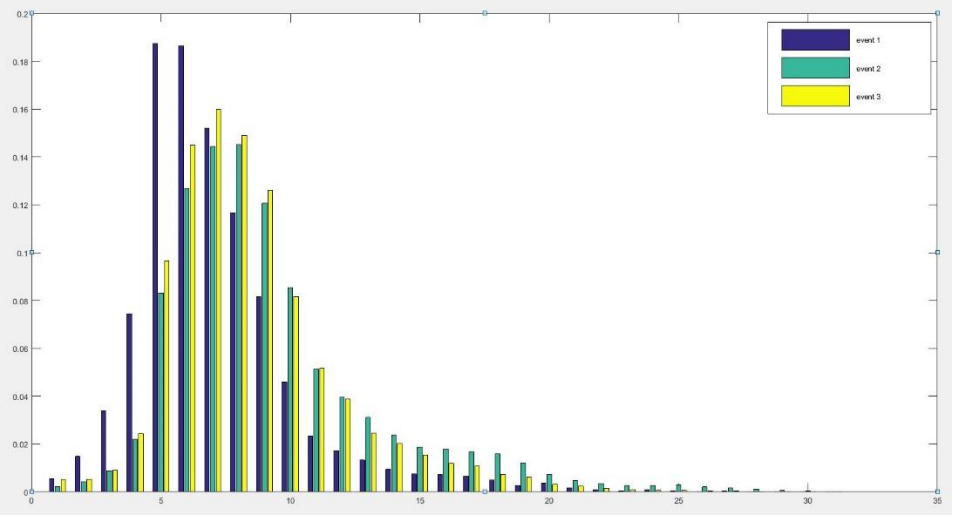

Figure 4.13 Percentages of drops distribution at different diameters

Figure 4.15 shows the drop size distributions of all three rain events:

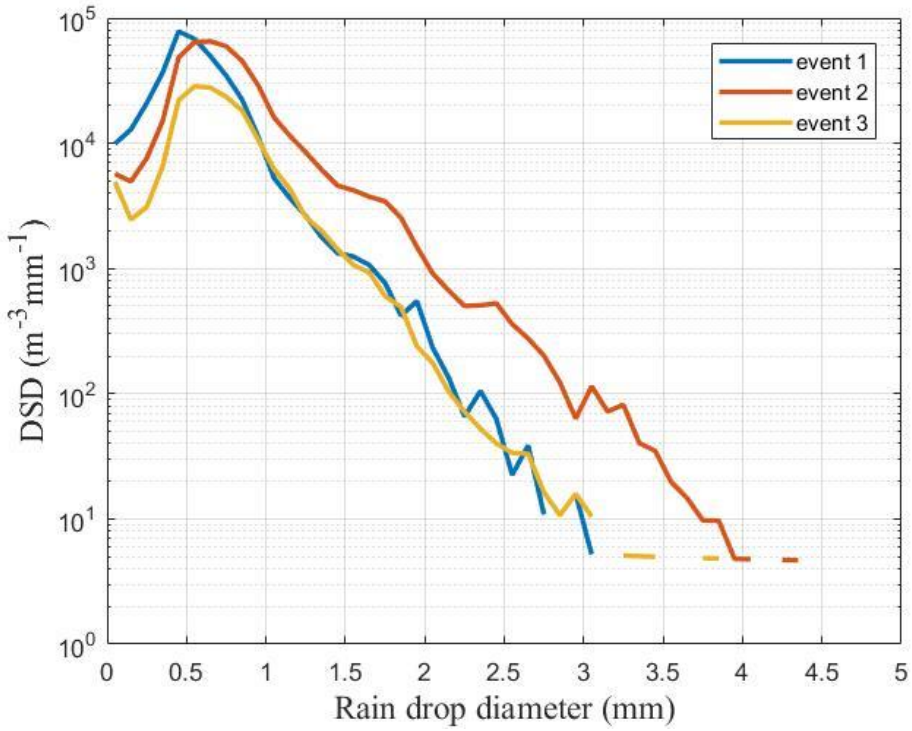

Figure 4.14 Drop size distributions of all the events

The peaks of DSD curve at each minute changes with the same trend as the rain intensities curves. However, the distribution of drops larger than 1.5 mm is not strictly related to rain intensity as event 3 has more percentages of drops with diameters larger than 1.5 mm than event 1 and event 2.

A reasonable explanation could be these three rain events were brought by different types of clouds, convective cloud or stratiform cloud. Meteorologists have indicated that droplets grow in two different ways in these two types of clouds. If the droplets grow in convective clouds, the primary procedure of collecting water will be coalescence and/or rimming. On the other hand, in stratiform clouds droplets will grow by vapor diffusion [16]. The different generations of drops give rainfall different characteristics: stratiform rain normally has a lower rain rate and a lower standard deviation of rain rate statistic and convective rain normally has either a higher rain rate or a higher standard deviation of rain rate [17]. The catalogues of rain events could be done by analysis of the drop size distributions of each particular rain event and compare the parameters. Detailed results will be given in Chapter 5.

4.4 Summary

This chapter conducted a comprehensive analysis of precipitation data collected over the year 2018, focusing on annual statistics and specific rain events to characterize rainfall patterns in the Durham region, UK. Key parameters such as rain intensity, duration, and drop size distribution (DSD) were systematically evaluated using high-resolution measurements from a laser disdrometer. Annual rainfall statistics revealed that the majority of rain events exhibited intensities below 50 mm/h, with a worst-month analysis identifying July 2018 as having the highest recorded rain intensity of 150 mm/h. Catalogued rain events based on intensity and duration were shown, highlighting distinct characteristics between stratiform and convective precipitation. Stratiform rain events, characterized by lower intensities and longer durations, demonstrated a dominance of smaller drop sizes (<1.5 mm), while convective events exhibited higher intensities with broader DSD curve. Three specific rain events in January 2018 were analysed, revealing how variations in DSD influenced attenuation dynamics despite similar rainfall rates.

The evaluation of three DSD models: Marshall-Palmer exponential, log-normal, and gamma distributions were introduced using nonlinear least squares fitting. The gamma distribution demonstrated superior adaptability to the observed DSD data, particularly in capturing the skewed drop populations of convective rain and the narrow spectrum of stratiform events. This finding indicated the necessity of region-specific model calibration, especially in temperate climates with mixed precipitation types. By correlating DSD variations with rain microphysics, this chapter provided foundational insights into the interplay between raindrop characteristics and meteorological conditions, fully preparing for improved rain attenuation modelling in subsequent chapters. The annual DSD statistics and event-specific analyses increased the understanding of regional precipitation patterns, offering valuable empirical data for validating and refining communication system designs in millimetre Wave bands.

4.5 References

[1] Recommendation ITU-R P.536.17: “Propagation data and prediction methods required for the design of terrestrial line-of-sight systems” ITU-R P. Ser., Geneva, Switzerland, ITU International Telecommunications Union, 2017

[2] Recommendation ITU-R P.311.17: “Acquisition, presentation and analysis of data in studies of radiowave propagation” ITU-R P. Ser., Geneva, Switzerland, ITU International Telecommunications Union, 2017

[3] R. K. Crane, “Estimating Risk for Earth-Satellite Attenuation Prediction”, Proceedings of the IEEE, vol. 81, no. 6, pp. 906- 913, 1993.

[4] K. Park, Fundamentals of probability and stochastic processes with applications to communications. Cham: Springer, 2018.

[5] Recommendation ITU-R P.581.2: “The concept of worst month” ITU-R P., ITU International Telecommunications Union, 1990.

[6] C. Tfwala, L. van Rensburg, R. Schall, S. Mosia and P. Dlamini, "Precipitation intensity-duration-frequency curves and their uncertainties for Ghaap plateau", Climate Risk Management, vol. 16, pp. 1-9, 2017.

[7] D. Atlas and C.W. Ulbrich, “Path- and area-integrated rainfall measurement by microwave attenuation in the 1-3 cm band,” J. Appl. Meteorol., vol. 16, pp. 1322–1331, 1977.

[8] Marshall, J.S.; Palmer, W.M. The distribution of raindrops with size. J. Meteor. 1948,5, 165–166.

[9] J. Laws and D. Parsons, "The relation of raindrop-size to intensity", Transactions, American Geophysical Union, vol. 24, no. 2, p. 452, 1943.

[10] E. Baltas, D. Panagos and M. Mimikou, "Statistical Analysis of the Raindrop Size Distribution Using Disdrometer Data", Hydrology, vol. 3, no. 1, p. 9, 2016.

[11] G. Feingold and Z. Levin, "The Lognormal Fit to Raindrop Spectra from Frontal Convective Clouds in Israel", Journal of Climate and Applied Meteorology, vol. 25, no. 10, pp. 1346-1363, 1986.

[12] Ulbrich, C. W., 1983: Natural variations in the analytical form of the raindrop size

distribution. J. Climate Appl. Meteor., 22, 1764–1775

[13]C. Ulbrich and D. Atlas, "Microphysics of Raindrop Size Spectra: Tropical Continental and Maritime Storms", Journal of Applied Meteorology and Climatology, vol. 46, no. 11, pp. 1777-1791, 2007.

[14]J. Testud, S. Oury, R. Black, P. Amayenc and X. Dou, "The Concept of “Normalized” Distribution to Describe Raindrop Spectra: A Tool for Cloud Physics and Cloud Remote Sensing", Journal of Applied Meteorology, vol. 40, no. 6, pp. 1118-1140, 2001.

[15] Testud, J., E. Le Bouar, E. Obligis, and M. Ali Mehenni. 2000. The rain profiling algorithm applied to polarimetric weather radar. J. Atmos. Oceanic Technol. 17:332–356.

[16]R. Houze, "Stratiform Precipitation in Regions of Convection: A Meteorological Paradox?", Bulletin of the American Meteorological Society, vol. 78, no. 10, pp. 2179-2196, 1997.

[17]C. You, D. Lee, M. Kang and H. Kim, "Classification of rain types using drop size distributions and polarimetric radar: Case study of a 2014 flooding event in Korea", Atmospheric Research, vol. 181, pp. 211-219, 2016.

Chapter5 Drop Size Distribution Fitting

In this chapter, collected rain drop size distribution data will be fitted to theoretical distribution models in order to explore the micro-structures of precipitation events. Fitting methods will be introduced and explained in detail. The fitting results will be compared in two different categories. Firstly, the drop size distribution of every minute with the same rain intensity will be compared and secondly the average drop size distribution of individual rain events will be compared.

5.1 Fitting Methods

Three analytical distribution models suitable for drop size distributions including Marshall and Palmer Model, log-normal distribution model and gamma distribution model have been introduced in Chapter 4. To fit a set of measured drop size distribution data to an analytical distribution model, different fitting methods need to be used and different tests and criteria need to be applied as well to judge the goodness of each fitting methods in order to get ideal fitting results. Brief introductions of several fitting methods will be given below including Maximum Likelihood Method, Method of Moments and Least Squares Fitting Method.

5.1.1 Maximum Likelihood Method

The Maximum Likelihood Method (MLE) is a distribution fitting method based on likelihood function $L(\theta;x)$. For a given statistical distribution

$$\{ f(\bullet;\theta) \mid \theta \in \Theta \} \tag{5.1}$$

where θ stands for the parameters of the distribution model, if there is a value of θ to maximize the likelihood function $L(\theta;x)$, then this value or set of values is most suitable for the distribution models to fit the given distribution. In practice, natural logarithm of the likelihood function, also called the log-likelihood, is normally used because of the convenience of calculation:

$$l(\theta; x) = \ln L(\theta; x) \tag{5.2}$$

The likelihood function *L(θ;x)* and the log-likelihood function $l(\theta; x)$ will reach the maximum value at the same value of θ since the logarithm is a monotonic function.

The first step for maximum likelihood method is to select a suitable mathematical model to fit and in case of this research, the models which have been discussed in Chapter 4. The second step is to define the likelihood function based on the selected model. This function mathematically represents the probability density function (PDF) of observing the specific data points given different values of the unknown parameters. Then by maximize the likelihood function, to modify the model's prediction to maximally align with the observed data. Since the diameter of the droplets is mathematical discrete and the weight of smaller drops is relatively large because of the setting of size bin widths, the result was biased by the smaller drops when using this method of fitting. It should be noticed that the fitted probability distribution function which is converted by drop size distribution function shown a centre movement towards smaller size direction. And it should also be mentioned that the log-normal distribution introduced in Chapter 4.2.2 which has a general form as:

$$N(D) = \frac{N_T}{\sqrt{2\pi}\sigma_g (D-\theta)} \cdot e^{-\frac{(\ln(D-\theta)-\mu_g)^2}{2\sigma_g^2}} \tag{4.5}$$

could be divided by this method. It established a dependency for $(D-\theta)$ and μ_g.[1]

5.1.2 Method of Moments

The Method of Moments (MOM) is a well-known fitting method and has been briefly introduce in Chapter 4.2.3 in calculations of Gamma distribution model. The basic principle of this method is picking known value or parameters of given data and creating a list of equations which could be expressed by the values of higher moments like variance, skewness and kurtosis. In case of a rain drop size distribution the

moments could be defined by:

$$m_n(t) = \int_0^\infty D^n N(D,t) dD \tag{4.11}$$

Considering the diameters for particles are discrete, it could be rewritten as

$$m_n(t) = \sum_{i=1}^{n_c} D_i^n N(D_i,t) \Delta D_i \tag{5.3}$$

where n is the order of the moment and n_c is the number of bins for droplet observation.[2]

The moments of different chosen models can be derived by functions of its parameters. Compare the empirical moments with the corresponding expressions derived from the model, the model parameters which fit best could be found.

Method of moments is simpler for implementing compared to methods like maximum likelihood estimation. However, the estimation made by the method of moments may be inaccurate if the sample size is too small and in some cases, it may not take all the relevant information of the sample into account. [3]

5.1.3 Non-linear Least Square Error fitting method

Non-linear Least Square Error (NLSE) fitting method is another widely used regression method to fit observed data set with an existing model that has a non-linear mathematical expression. To implement NLSE, objective function which is the sum of squared difference between the observed data and estimated data is listed below:

$$f(\theta) = \sum_{i=1}^{N} (N_{ob,i} - N_{m,i}(\theta))^2 \tag{5.4}$$

where $N_{ob,i}$ and $N_{m,i}$ stand for the number of raindrops in size bin i observed and predicted by the model respectively[3]. Then an optimization algorithm is used to adjust the model parameter θ to minimize the objective function.

NLSE has a clear advantage compared to MOM because this method is less sensitive to noise and outliers and practical collected data have little possibility obeying arbitrary nonlinear functions. For example, the average drop size distribution at 10 mm/h over 2018 is shown in Figure 5.1.

In this project, the collected rain drop size distribution data are fitted into exponential distribution model, log-normal distribution model and gamma distribution model. The details of how these distribution models are designed was introduced in Chapter 4.2.

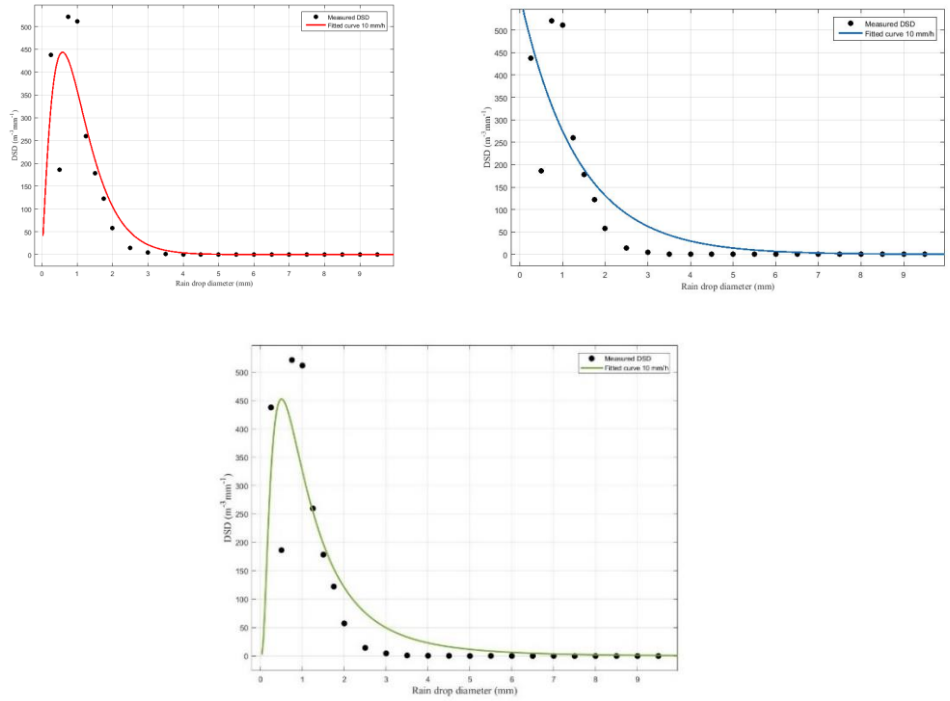

Figure 5.1 Fitting results for log-normal, exponential and gamma distribution model DSD for rain rate higher than 10mm/h of 2018.

The fitting results above are created by Matlab curve fitting tool using NLSE method and it shows the differences of the three models. The curves of log-normal distribution and gamma distribution model have peaks which fit the trend of raw data well, on the other hand, exponential distribution function is monotonically decreasing. However, for the fitting results across all different rain rates, log-normal distribution and gamma distribution are sometime monotonically decreasing as well. All fitting results are reported in Section 5.2.

5.2 Fitting Results

In this section, all the DSD fitting results in specific rain rate for year 2018 are presented. Fitting parameters are also give in Table 5.1.

5.2.1 exponential distribution model

The fitting results for exponential distribution fitting are shown below. The curve of exponential model is a single-tailed, monotonically decreasing curve, which could not present more detailed information like peaks or skewness.

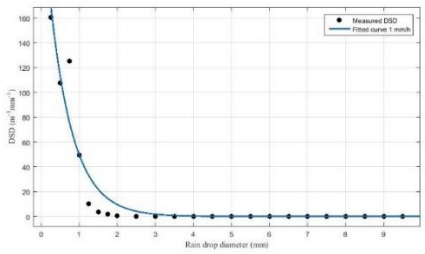

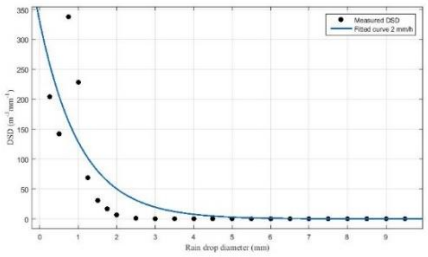

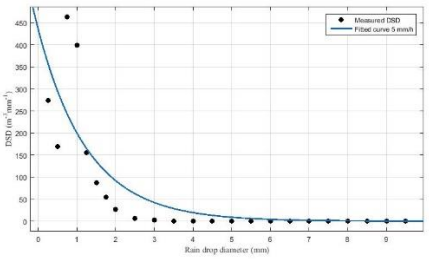

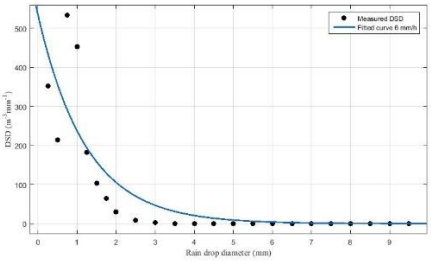

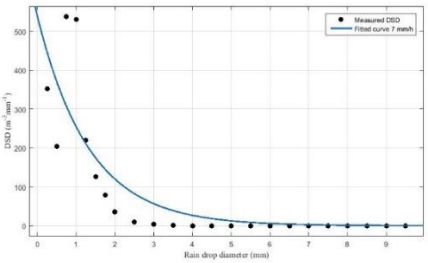

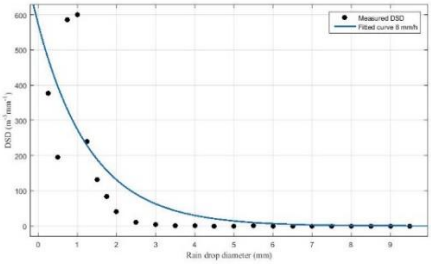

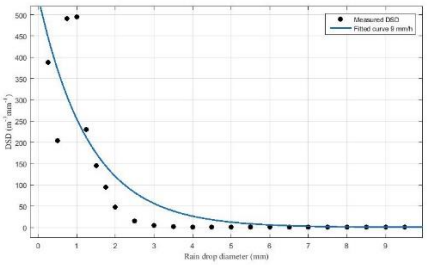

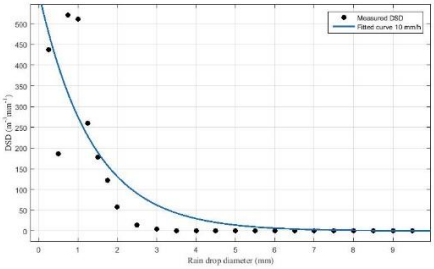

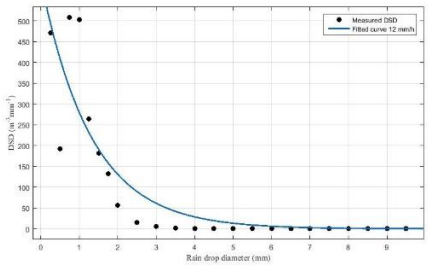

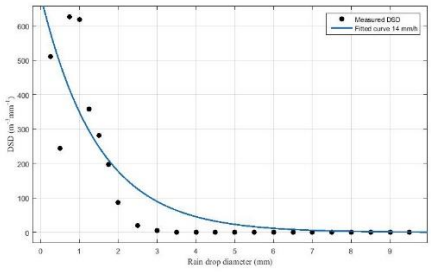

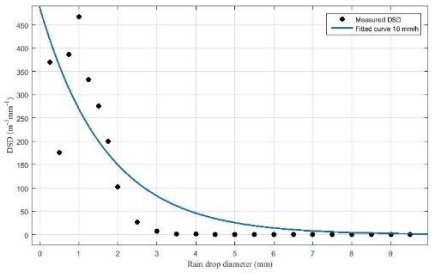
Measured DSD
Fitted curve 16 mm/h
DSD (m^{-3}mm^{-1})
Rain drop diameter (mm)

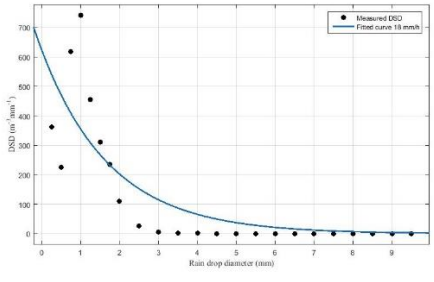
Measured DSD
Fitted curve 18 mm/h
DSD (m^{-3}mm^{-1})
Rain drop diameter (mm)

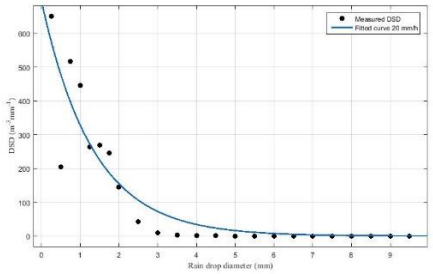
Measured DSD
Fitted curve 20 mm/h
DSD (m^{-3}mm^{-1})
Rain drop diameter (mm)

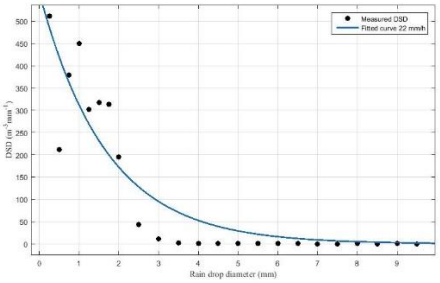
Measured DSD
Fitted curve 22 mm/h
DSD (m^{-3}mm^{-1})
Rain drop diameter (mm)

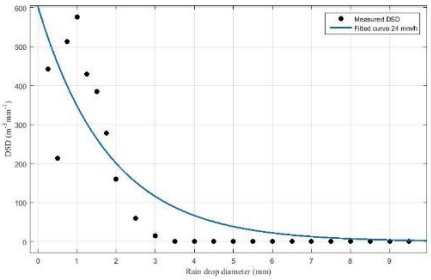
Measured DSD
Fitted curve 24 mm/h
DSD (m^{-3}mm^{-1})
Rain drop diameter (mm)

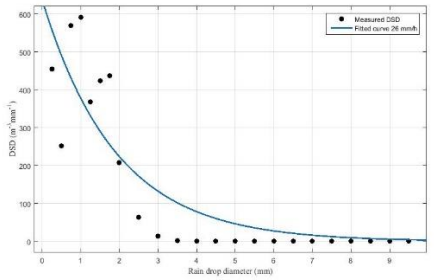
Measured DSD
Fitted curve 26 mm/h
DSD (m^{-3}mm^{-1})
Rain drop diameter (mm)

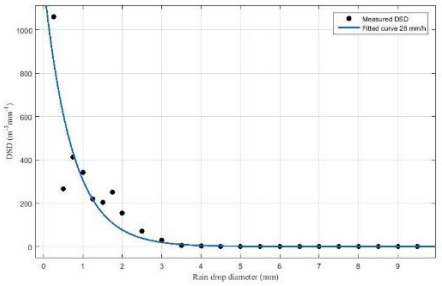
Measured DSD
Fitted curve 28 mm/h
DSD (m^{-3}mm^{-1})
Rain drop diameter (mm)

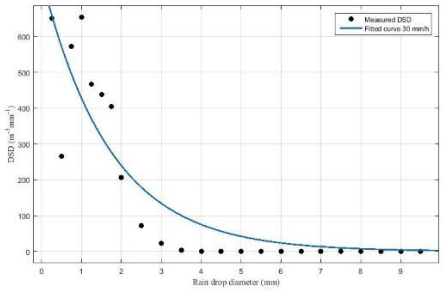
Measured DSD
Fitted curve 30 mm/h
DSD (m^{-3}mm^{-1})
Rain drop diameter (mm)

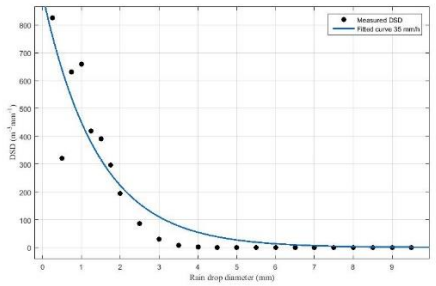
Measured DSD
Fitted curve 36 mm/h
DSD (m^{-3}mm^{-1})
Rain drop diameter (mm)

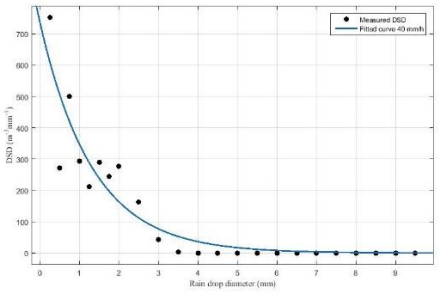
Measured DSD
Fitted curve 40 mm/h
DSD (m^{-3}mm^{-1})
Rain drop diameter (mm)

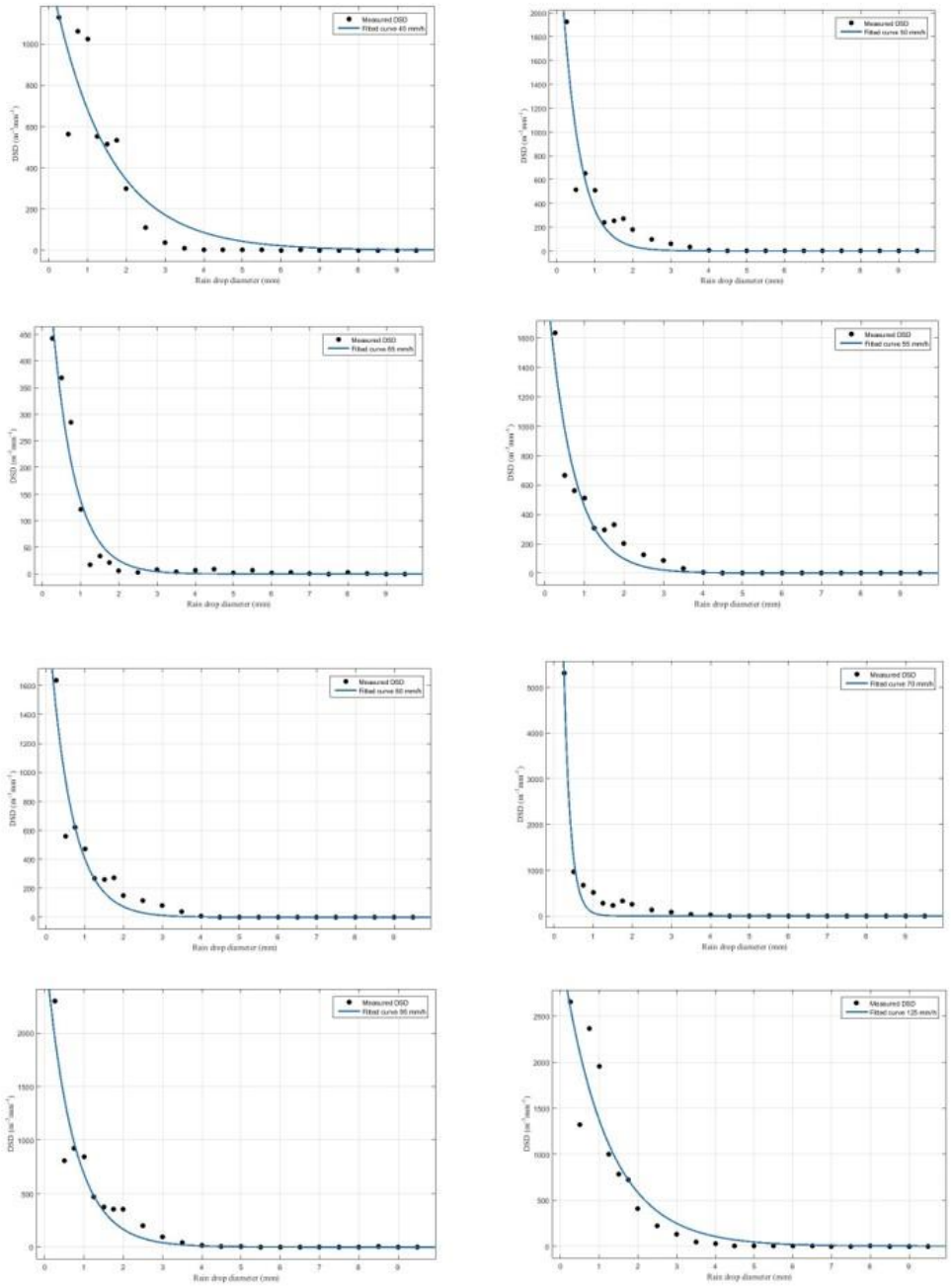

Figure 5.2 Fitting results for exponential distribution model DSD for different rain rate of 2018.

The NLSE-fitted exponential model provides a basic approach to analysing DSDs. Its simplified format is convenient for calculations but might not capture the full complexity of observed raindrop size distributions compared to other models. Also, for raindrops whose diameters between 1 mm to 2 mm, the predicted value of exponential model shifts a considerable large distance from the collected distribution data which could be critical since raindrops belong to that diameter range have higher possibility in a rain event and the volume is high as well.

5.2.2 log-normal distribution model

The fitting results for log-normal distribution fitting are shown below. Majority of the log-normal model curves present a skewed distribution with more small raindrops, it fits the collected raindrop size distribution more accurately than the exponential distribution curves. However, at certain rain rate the fitted models are single tailed like exponential model, the reason could be the pre-processing procedure is not accurate enough to eliminate outliers of some unique data points.

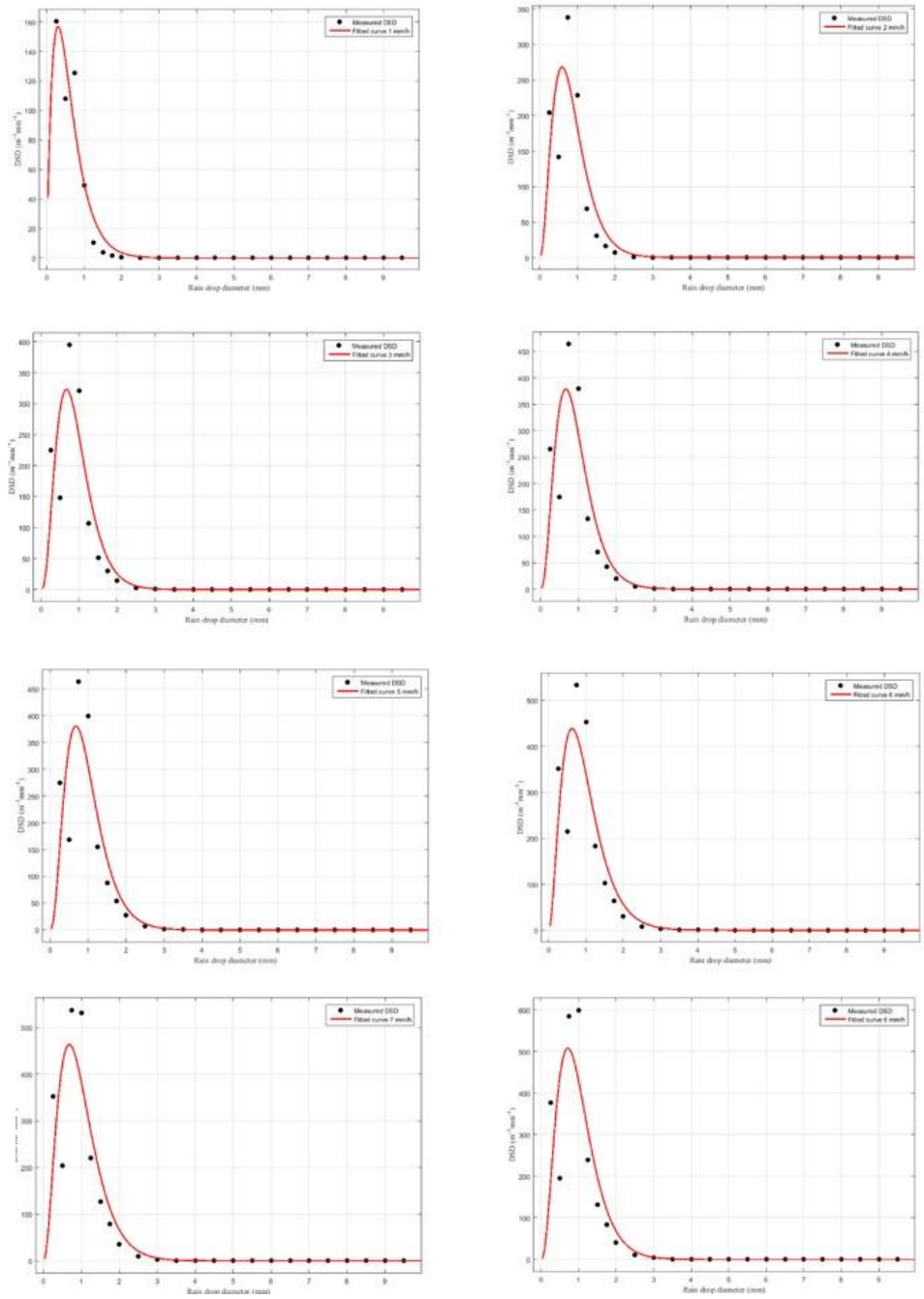

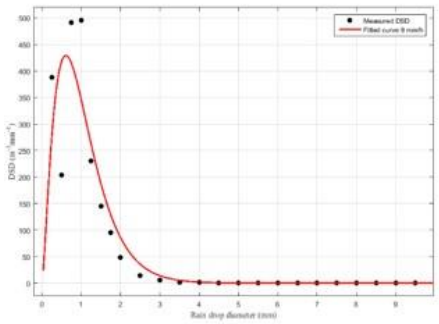
Measured DSD
Fitted curve 9 mm/h
Rain drop diameter (mm)

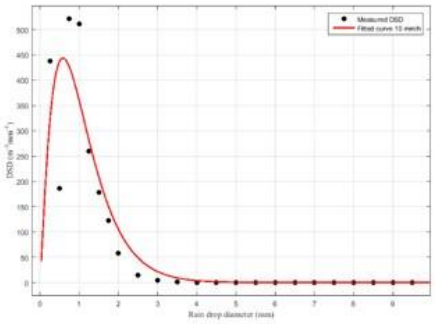
Measured DSD
Fitted curve 10 mm/h
Rain drop diameter (mm)

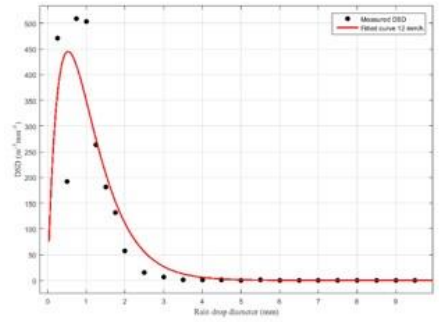
Measured DSD
Fitted curve 12 mm/h
Rain drop diameter (mm)

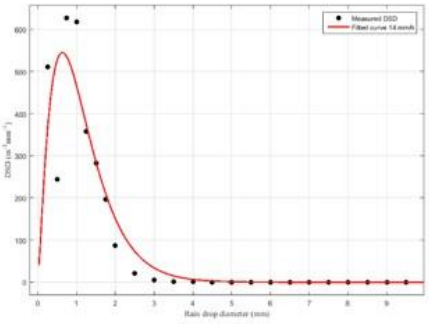
Measured DSD
Fitted curve 14 mm/h
Rain drop diameter (mm)

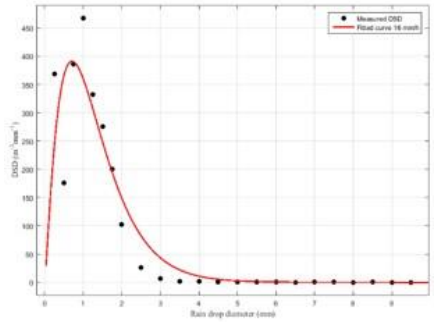
Measured DSD
Fitted curve 16 mm/h
Rain drop diameter (mm)

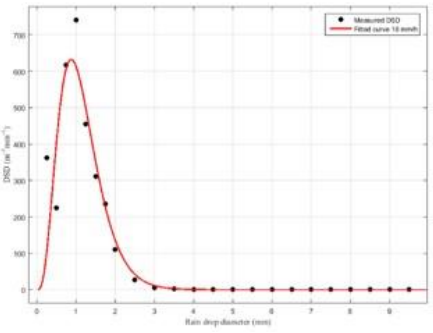
Measured DSD
Fitted curve 18 mm/h
Rain drop diameter (mm)

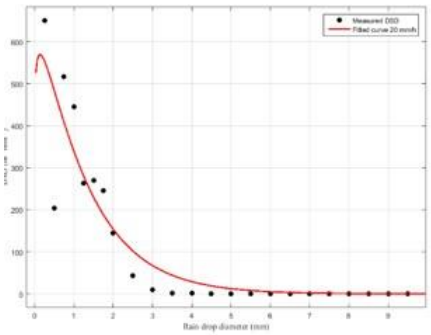
Measured DSD
Fitted curve 20 mm/h
Rain drop diameter (mm)

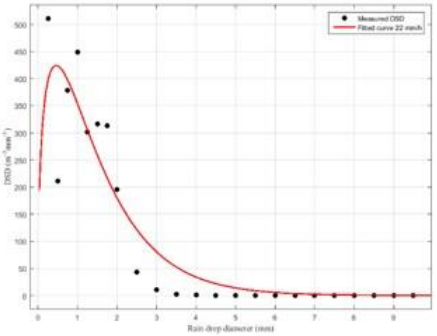
Measured DSD
Fitted curve 22 mm/h
Rain drop diameter (mm)

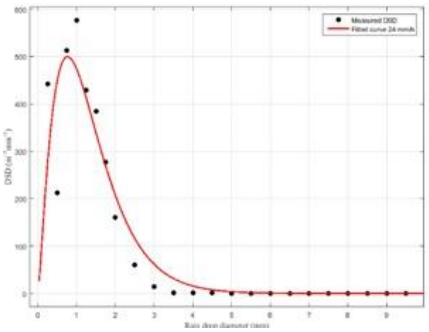
Measured DSD
Fitted curve 24 mm/h

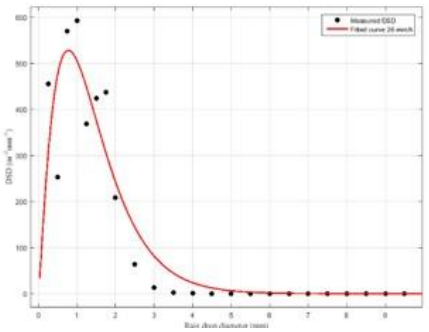
Measured DSD
Fitted curve 26 mm/h

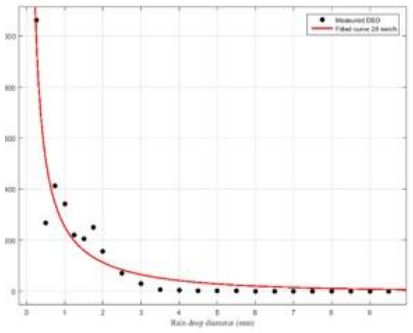
Measured DSD
Fitted curve 28 mm/h
Rain drop diameter (mm)

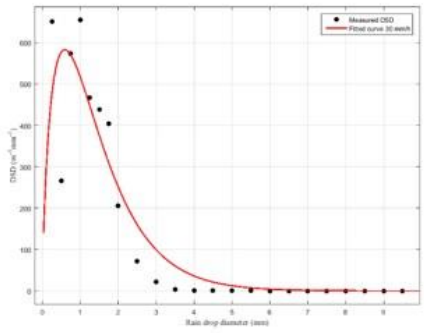
Measured DSD
Fitted curve 30 mm/h
Rain drop diameter (mm)

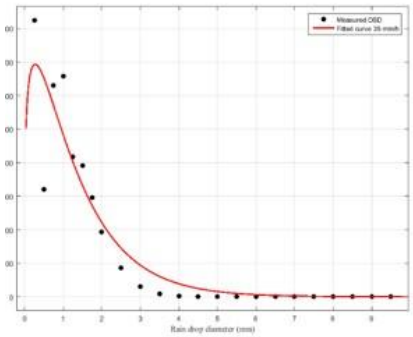
Measured DSD
Fitted curve 26 mm/h
Rain drop diameter (mm)

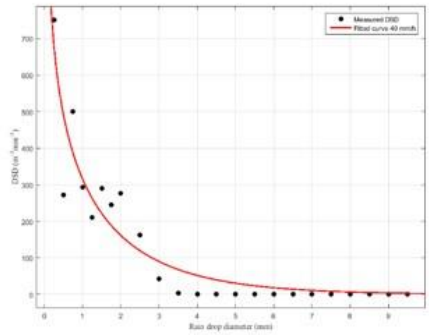
Measured DSD
Fitted curve 40 mm/h
Rain drop diameter (mm)

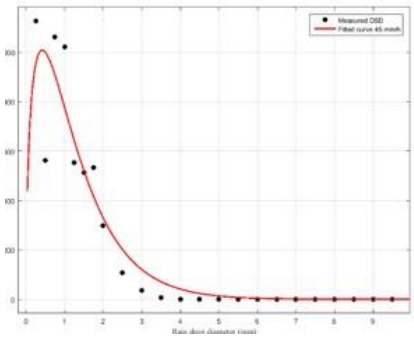
Measured DSD
Fitted curve 45 mm/h
Rain drop diameter (mm)

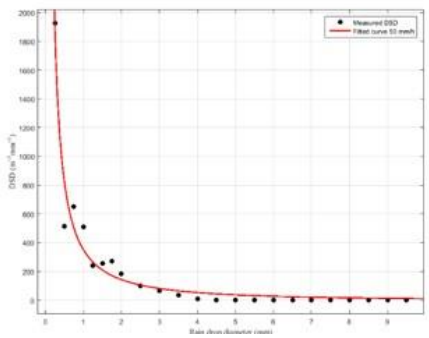
Measured DSD
Fitted curve 50 mm/h
Rain drop diameter (mm)

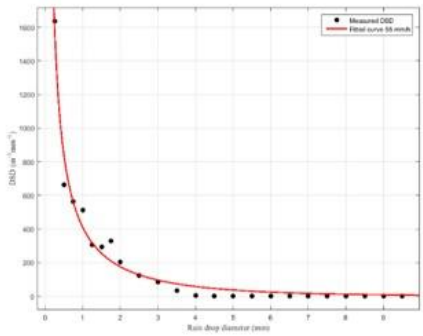
Measured DSD
Fitted curve 55 mm/h
Rain drop diameter (mm)

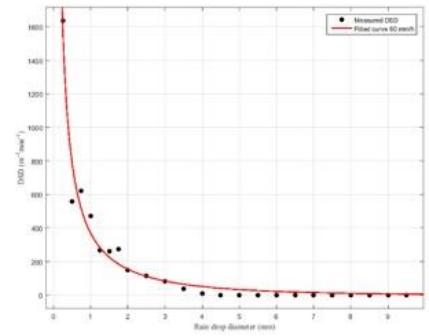
Measured DSD
Fitted curve 60 mm/h
Rain drop diameter (mm)

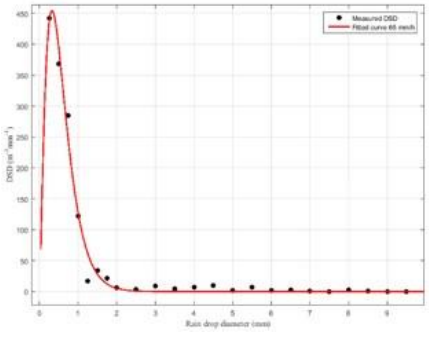
Measured DSD
Fitted curve 65 mm/h
Rain drop diameter (mm)

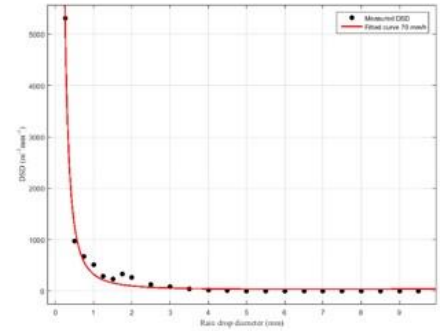
Measured DSD
Fitted curve 70 mm/h
Rain drop diameter (mm)

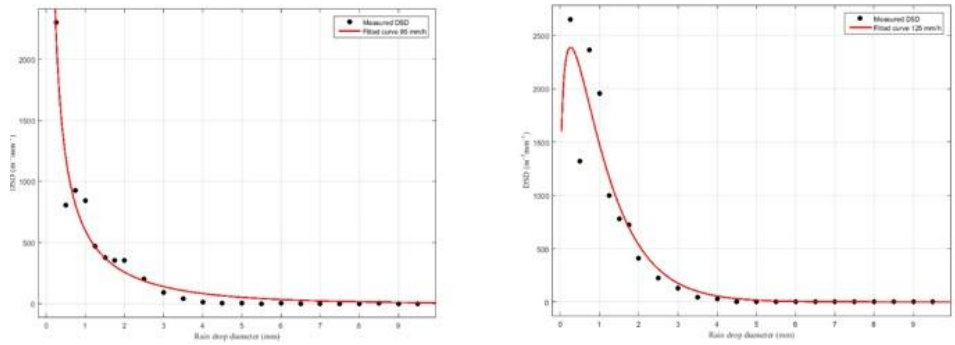

Figure 5.3 Fitting results for log-normal distribution model DSD for different rain rate of 2018.

The NLSE-fitted log-normal model offers a significant improvement over the exponential model, capturing the skewed nature of raindrop size distributions and providing parameters with real physical meanings related to the median diameter and spread. Log-normal model presents a balance of accurate representation and interpretability.

5.2.3 Gamma distribution model

The fitting results for gamma distribution fitting are shown below. It shows some similarity with log-normal model because it could be considered as a log-normal distribution model introduced with gamma function. With the help of gamma function, the shape of gamma model curve is relatively flexible compared to log-normal distribution model. However, the fitted model does not perform well at maximum value, the peak, of the curve. the reason could be the pre-processing procedure is not accurate enough to eliminate outliers of some unique data points and the gamma function to modify the shape of the curve is not fine enough and could be adjusted.

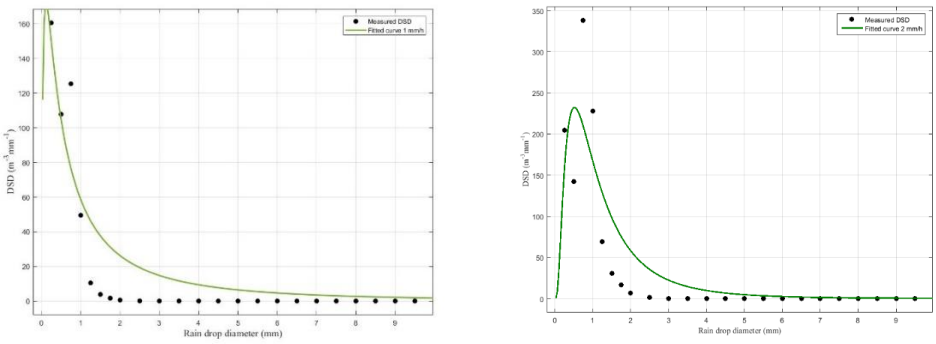

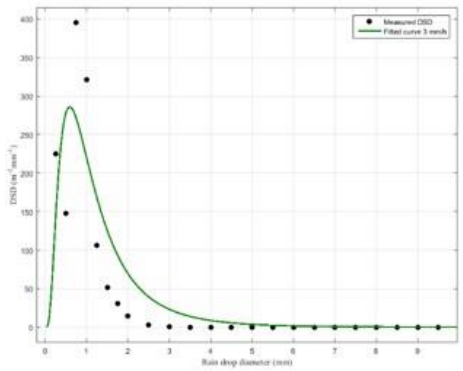
Measured DSD
Fitted curve 3 mm/h
DSD (m^{-3}mm^{-1})
Rain drop diameter (mm)

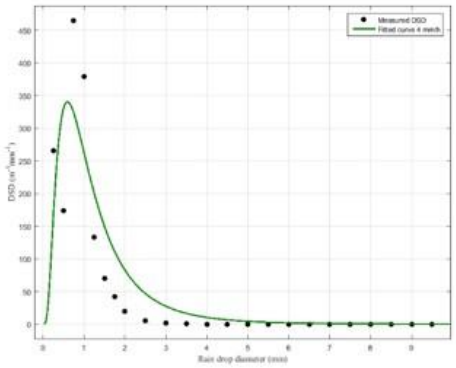
Measured DSD
Fitted curve 4 mm/h
DSD (m^{-3}mm^{-1})
Rain drop diameter (mm)

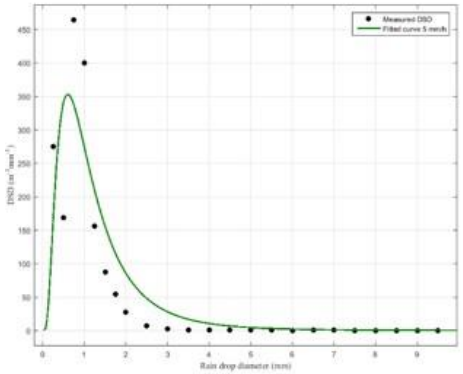
Measured DSD
Fitted curve 5 mm/h
DSD (m^{-3}mm^{-1})
Rain drop diameter (mm)

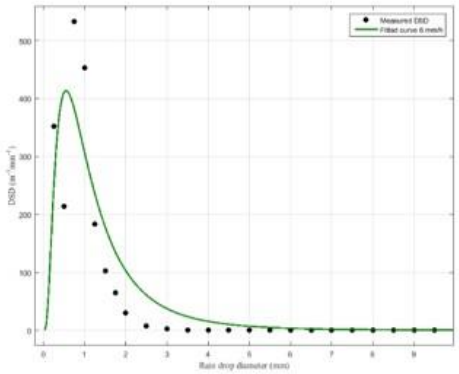
Measured DSD
Fitted curve 6 mm/h
DSD (m^{-3}mm^{-1})
Rain drop diameter (mm)

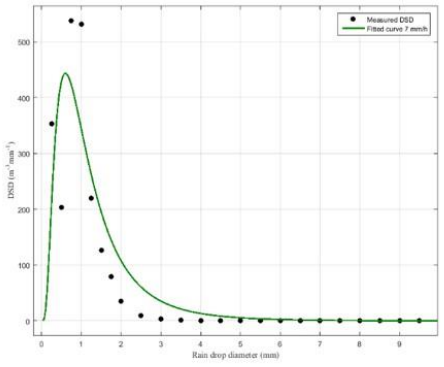
Measured DSD
Fitted curve 7 mm/h
DSD (m^{-3}mm^{-1})
Rain drop diameter (mm)

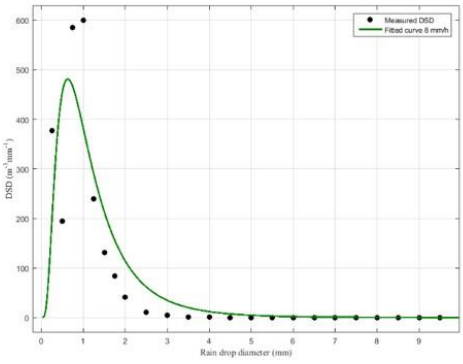
Measured DSD
Fitted curve 8 mm/h
DSD (m^{-3}mm^{-1})
Rain drop diameter (mm)

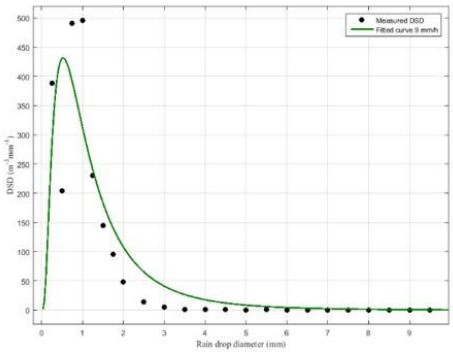
Measured DSD
Fitted curve 9 mm/h
DSD (m^{-3}mm^{-1})
Rain drop diameter (mm)

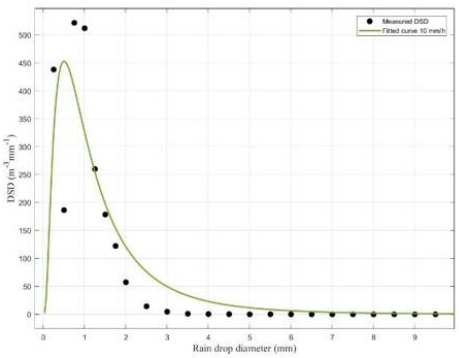
Measured DSD
Fitted curve 10 mm/h
DSD (m^{-3}mm^{-1})
Rain drop diameter (mm)

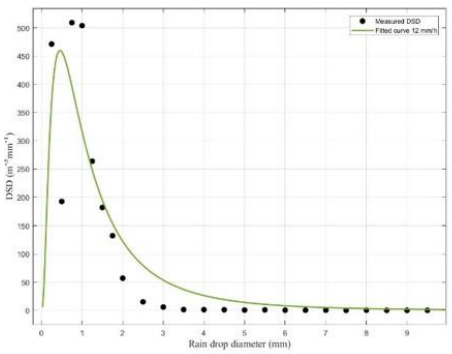
Measured DSD
Fitted curve 12 mm/h
DSD (m^{-3}mm^{-1})
Rain drop diameter (mm)

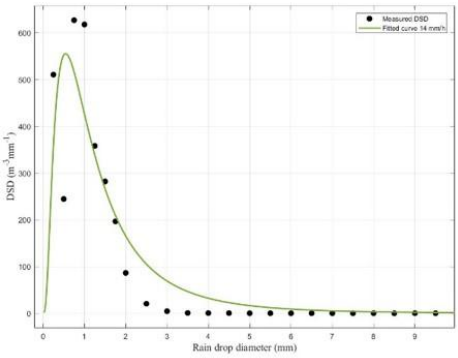
Measured DSD
Fitted curve 14 mm/h
DSD (m^{-3}mm^{-1})
Rain drop diameter (mm)

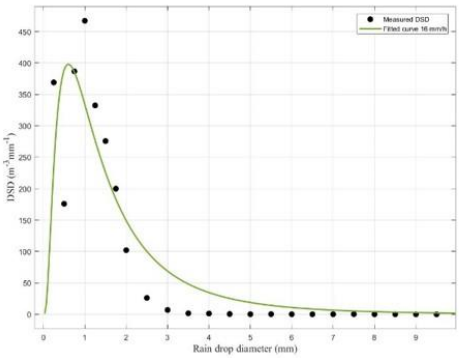
Measured DSD
Fitted curve 16 mm/h
DSD (m^{-3}mm^{-1})
Rain drop diameter (mm)

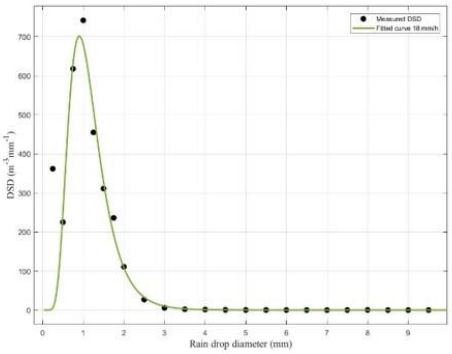
Measured DSD
Fitted curve 18 mm/h
DSD (m^{-3}mm^{-1})
Rain drop diameter (mm)

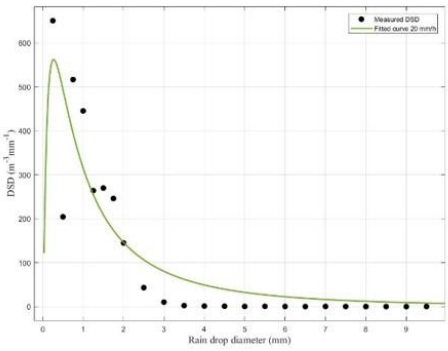
Measured DSD
Fitted curve 20 mm/h
DSD (m^{-3}mm^{-1})
Rain drop diameter (mm)

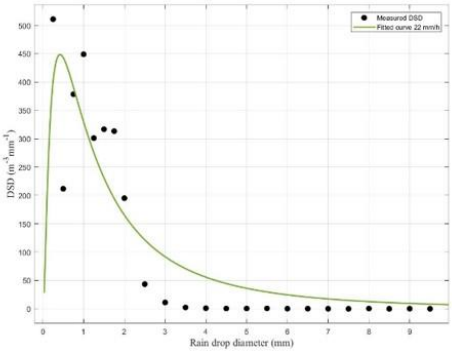
Measured DSD
Fitted curve 22 mm/h
DSD (m^{-3}mm^{-1})
Rain drop diameter (mm)

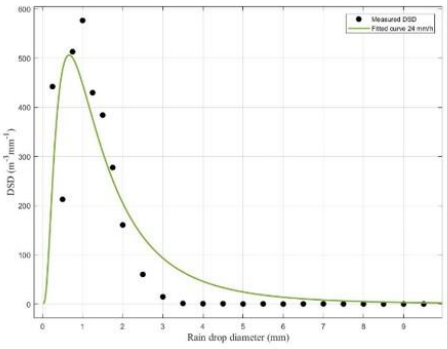
Measured DSD
Fitted curve 24 mm/h
DSD (m^{-3}mm^{-1})
Rain drop diameter (mm)

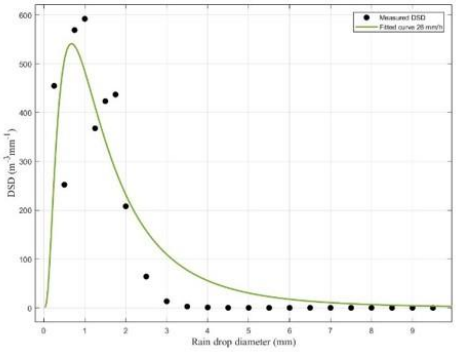
Measured DSD
Fitted curve 26 mm/h
DSD (m^{-3}mm^{-1})
Rain drop diameter (mm)

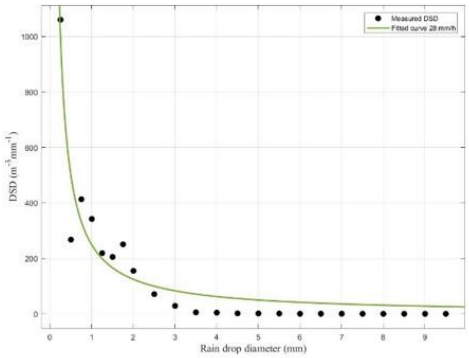
Measured DSD
Fitted curve 28 mm/h
DSD (m-3mm-1)
Rain drop diameter (mm)

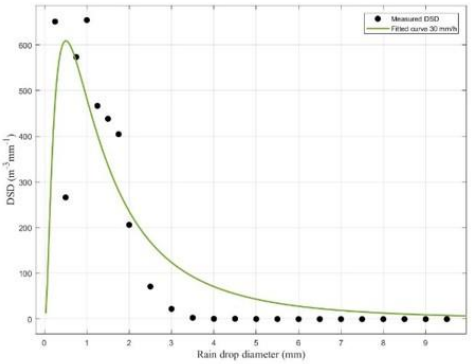
Measured DSD
Fitted curve 30 mm/h
DSD (m-3mm-1)
Rain drop diameter (mm)

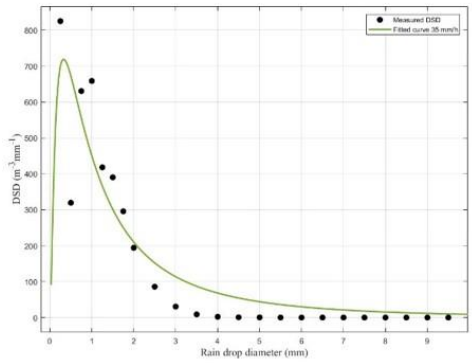
Measured DSD
Fitted curve 35 mm/h
DSD (m-3mm-1)
Rain drop diameter (mm)

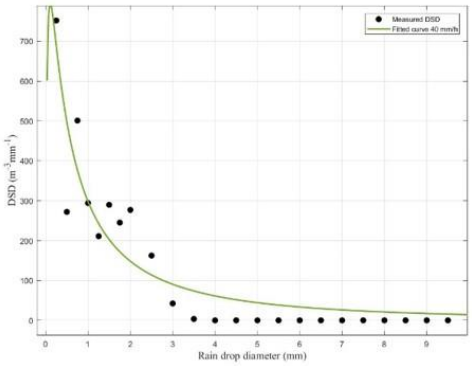
Measured DSD
Fitted curve 40 mm/h
DSD (m-3mm-1)
Rain drop diameter (mm)

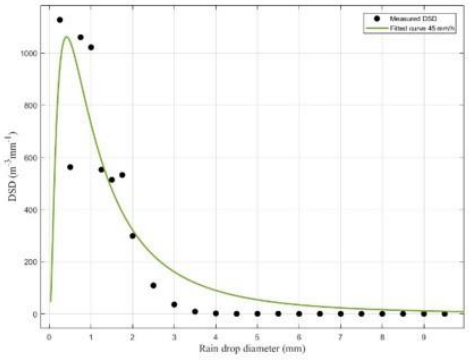
Measured DSD
Fitted curve 45 mm/h
DSD (m-3mm-1)
Rain drop diameter (mm)

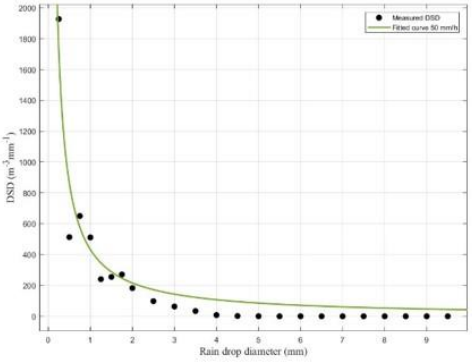
Measured DSD
Fitted curve 50 mm/h
DSD (m-3mm-1)
Rain drop diameter (mm)

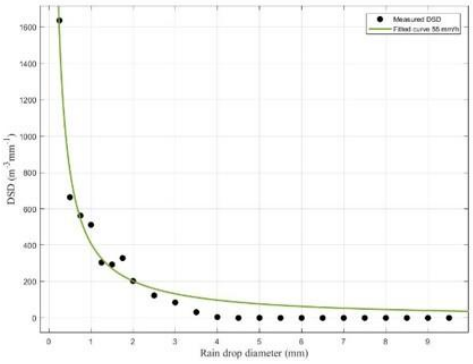
Measured DSD
Fitted curve 55 mm/h
DSD (m-3mm-1)
Rain drop diameter (mm)

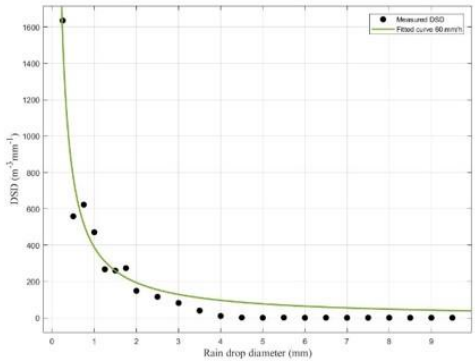
Measured DSD
Fitted curve 60 mm/h
DSD (m-3mm-1)
Rain drop diameter (mm)

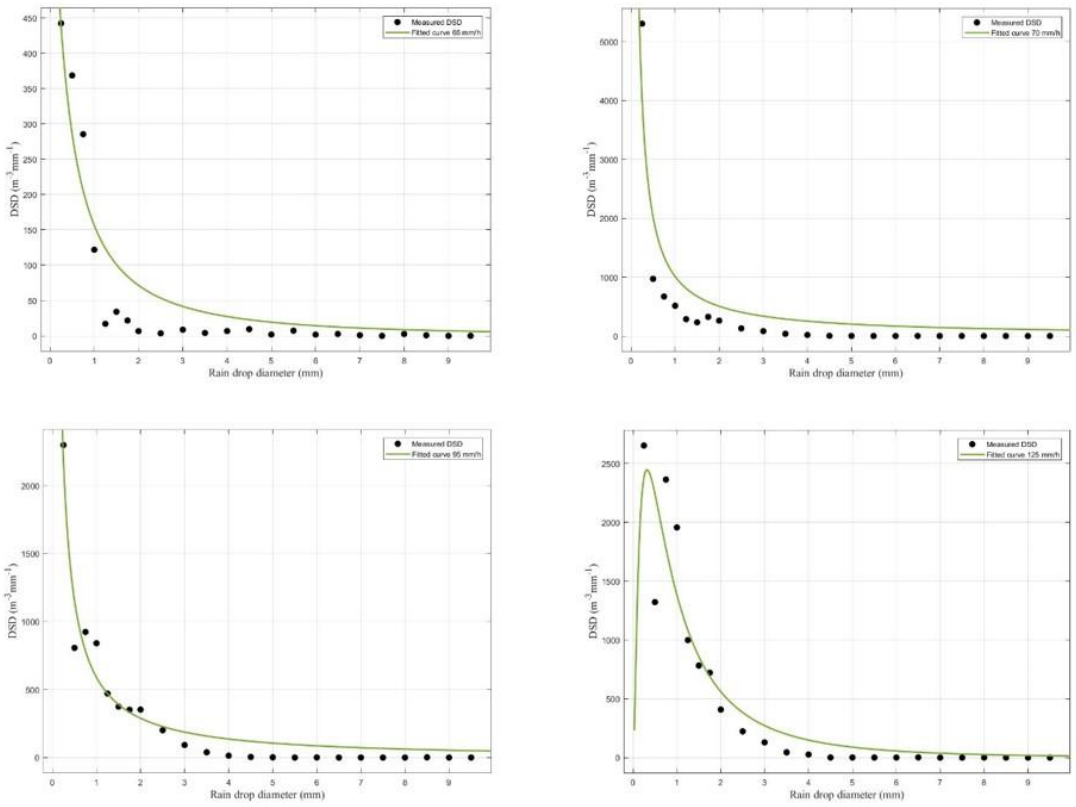

Figure 5.4 Fitting results for gamma distribution model DSD for different rain rate of 2018.

Table 5.1 shows the fitted parameters for gamma exponential and log-normal distribution models of the figures presented above.

Table 5.1 Fitted parameters for different drop size distribution models

Rain rate (mm/h)	Gamma distribution			Exponential distribution		Lognormal distribution		
	N0	mu	lambda	N0	lambda	NT	mu	sigma
1	1423	1.0	3.337	257	1.643	125	-0.611	0.738
2	8970	2.3	3.896	328	0.939	288	-0.217	0.668
3	1.68*10^4	2.8	4.220	366	0.831	264	-0.146	0.314
5	1.24*10^4	2.5	3.704	434	0.776	334	-0.113	0.332
10	2830	1.2	2.064	576	0.740	480	-0.020	0.404

20	810	0.12	0.871	696	0.752	978	0.181	1.224
40	498	-0.3	0.459	737	0.753	1225	0.327	1.606
60	465	-0.93	0.230	2206	1.706	2358	-1	2.349
70	232	-2.19	-0.331	6000	2.177	2650	-1	0.855

5.3 Rain Catalogues Analysis

In meteorology, considering how a rain event could occur, there are two different types of rain: Convective rain and Stratiform rain. It should be noticed that in nature, these two types of rain cannot be strictly distinguished from one another, but the classification method is still wildly accepted by meteorology researchers. The rain intensity of convective rain is generally higher than stratiform rain and the time duration is normally shorter. The reason for these behaviours is because convective clouds usually have limited horizontal extent. On the other hand, stratiform rain events are caused over surface cold fronts or over and ahead of warm fronts. As a result, these rain events tend to have a long duration and influence a large spatial area. [4]

In theory it could be distinguished from DSD curves as well. The DSD curves of convective rain events tend to have wider peaks and they normally hit the peak at larger drop diameters compared to the DSD curves of stratiform rain events, on the other hand the DSD curves of stratiform rain events usually have sharp peaks and the peaks normally happen at smaller diameters which means stratiform rain events contains more small drops compared with convective rain events [5]. Some researchers in meteorology argued that the threshold for “larger diameter” is around 3.0 mm, which means the number of droplets whose diameter are higher than 3.0 mm is quite less in stratiform rain events compared to convective rain events [6].

It should be noticed that although DSD provides valuable information for distinguishing rain types, it is not the only determining factor. Other factors like rainfall intensity, wind speed, and atmospheric temperature also contribute to shaping the

overall characteristics of precipitation events.

5.4 Summary

This chapter discusses fitting rain drop size distribution (DSD) data to theoretical distribution models to explore the micro-structures of precipitation events. Fitting methods are introduced and detailed, with results compared in two catalogues: DSDs at the same rain intensity and average DSDs of individual rain events. The chapter also concludes that while DSD provides valuable information for distinguishing rain types.

This chapter focused on fitting the collected rain drop size distribution (DSD) data to theoretical distribution models, in order to exploring the micro structures of precipitation events. A series of analyses and comparisons were involved.

Three analytical distribution models: Marshall and Palmer Model, log - normal distribution model, and gamma distribution model, were selected for the fitting process. To fit the measured DSD data, different fitting methods were employed, including the Maximum Likelihood Method, Method of Moments, and Non - linear Least Square Error fitting method. Each method had its own characteristics and limitations. For example, the Maximum Likelihood Method was based on the likelihood function, but the result was biased by smaller drops; the Method of Moments was relatively simple to implement but might be inaccurate with small sample sizes; and the NLSE fitting method was less sensitive to noise and outliers, which was beneficial for fitting the collected data.The fitting results of the three distribution models were compared in two categories: the drop size distribution of every minute with the same rain intensity and the average drop size distribution of individual rain events. The exponential distribution model, a special case of the gamma distribution, provided a basic approach to DSD analysis. However, its single - tailed, monotonically decreasing curve could not capture the full complexity of the observed raindrop size distributions, especially for raindrops with diameters between 1 mm and 2 mm. The log - normal distribution model, on the other hand, presented a skewed distribution that fit the collected raindrop size distribution more accurately than the exponential model in most cases. It also had

parameters with real physical meanings related to the median diameter and spread, offering a balance of accurate representation and interpretability. The gamma distribution model, with the help of the gamma function, had a relatively flexible curve shape. But it did not perform well at the peak of the curve, likely due to issues in the pre - processing procedure and the adjustment of the gamma function.

This chapter also analysed the DSD curves of different rain catalogues. In meteorology, rain is generally classified into convective rain and stratiform rain. Although these two types cannot be strictly distinguished in nature, the DSD curves can provide some clues for differentiation. Convective rain events tend to have wider peaks and larger drop diameters at the peak, while stratiform rain events usually have sharp peaks at smaller diameters. However, it was noted that DSD was not the only factor in distinguishing rain types, and other factors like rainfall intensity, wind speed, and atmospheric temperature also played important roles.

This chapter provided a deeper understanding of the micro - structures of precipitation events by fitting DSD data to theoretical models and comparing the results, it provided The evaluation of different distribution models and fitting methods helped to determine which model was more suitable for representing the rainfall patterns in the studied area. This was crucial for accurately predicting rain attenuation and understanding the impact of precipitation on millimetre wave propagation. Moreover, the analysis of rain catalogues based on DSD curves added a new perspective to the classification of rain events, which could potentially improve the accuracy of weather forecasting and communication system design in the face of different precipitation conditions.

5.5 References

[1] T. Adrian, "A Study of the Raindrop Size Distribution and its effect on Microwave Attenuation", Ph.D, University of Bath,2011.

[2] Andrieu, C., Creutin, J. D., Durand, Y., & Lang, M. (2004). “Use of a rain gauge network for validation of the TRMM 3B42 product”. Journal of Geophysical Research: Atmospheres, 109(D20).

[3] MathWorks. "Curve Fitting Toolbox Documentation." [Online]. Available: https://www.mathworks.com/help/curvefit/ Accessed on: Dec 6, 2023.

[4] Tokay, A., & Habib, E. (2005). “Rainfall rate and drop size distribution from disdrometer measurements in Kastamonu”, Turkey. Turkish Journal of Engineering and Environmental Science, 29(2), 151-159.

[5] Wang, Y., & Zhang, G. (2013). “A global survey of raindrop size distribution parameters from disdrometer observations”. Journal of Geophysical Research: Atmospheres, 118(17), 10017-10031.

[6] Tuerpe, A., & Simard, M. (2009). “Testing rain gauge performance using disdrometer measurements”. Journal of Hydrometeorology, 10(6), 1183-1190.

Chapter6 Rain Attenuation Modelling

In this chapter, analysis for different type of precipitation events is given. Not only annual statistics is focussed on, but also specific events with identical characteristics are listed. Comparisons are made among these events to make sure enough information has been considered.

6.1 Recorded Rain Attenuations

The system introduced in chapter 3 is used for a long-term measurement which started from January 2018. Based on the requirement of ITU recommendation [1], at least one-year data need to be considered to get reliable statistical results. To do this, the data collected from January 2018 to January 2019 are processed for analysis. The data are processed at a high standard to meet the submission requirements of the ITU DBSG3 and contribute to evaluation of statistics of rain intensity, rain event duration and rain drop size distributions. The recorded rain attenuation data were analysed and processed using MATLAB. Data for both horizontal and vertical polarizations of E-band and K-band signals were recorded during the measurements for the purpose of investigating the impact of rainfall on electromagnetic waves at different frequencies and with different polarization modes.

A clear correlation between the attenuation of received signal power and the precipitation data especially rain rate recorded at the observation station was observed. During periods of precipitation, the received signal power exhibited noticeable attenuation and the attenuation value increased with the intensity of precipitation. Figure 6.1 shows the relationship between the received signal power and precipitation intensity in a rain event in Jan 2018.

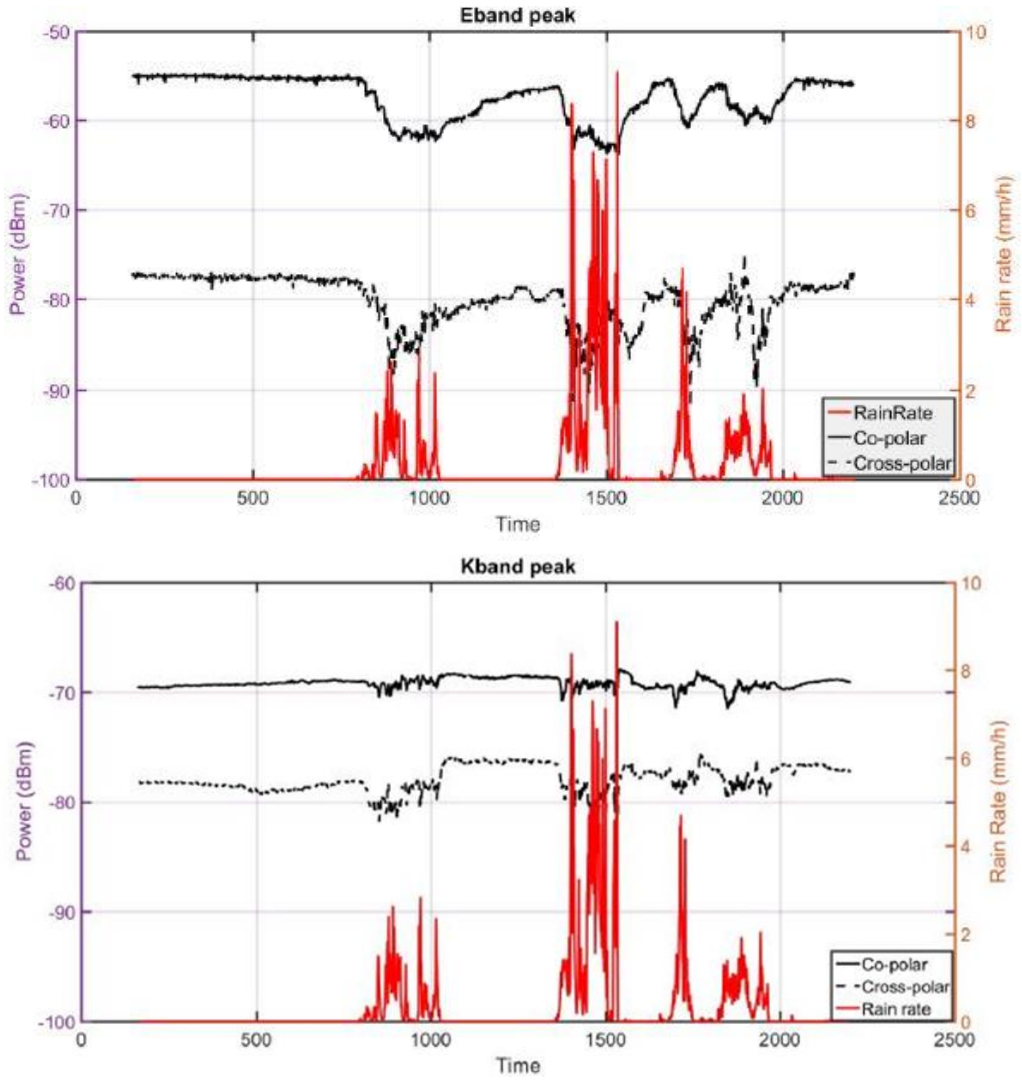

Figure 6.1 Relationship of received power and rain during a rain event in Jan 2018

In this project, the E-band and K-band frequencies were set to 77.52 GHz and 25.84 GHz, respectively. The collected received signal power data were put through an initial processing, including outlier removal and noise reduction using a moving average filter. This processing aimed to obtain the received signal power under clear sky conditions, which was the baseline for calculating the attenuation during precipitation events. Under clear skies with no precipitation, the received signal power at the E-band receiver was -59 dBm, while the K-band receiver measured -69 dBm. Figure 6.2 shows the attenuation data collected in three separate months: January, March and June to present the attenuation variation during different precipitation types and weather conditions.

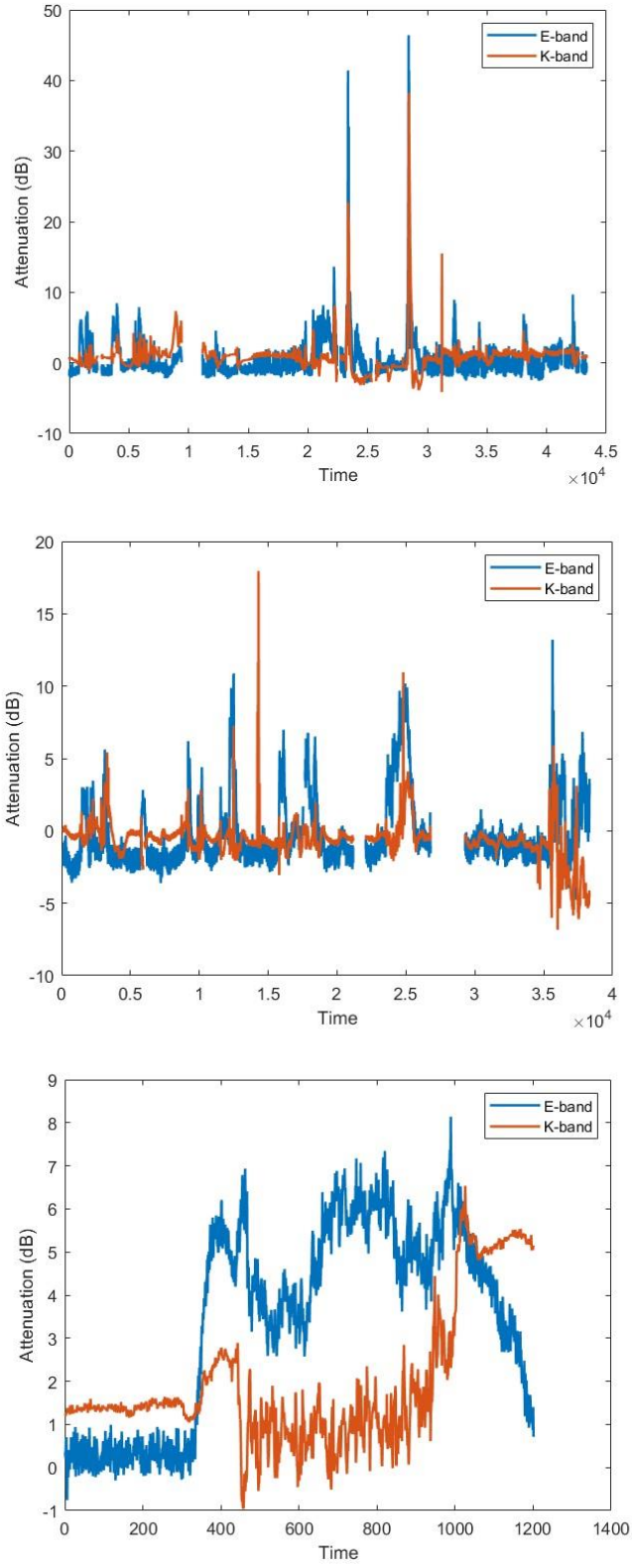

Figure 6.2 Attenuation variation in three different months

Analysis of attenuation data reveals a consistent relationship between attenuation distribution and measured precipitation distribution. Figure 6.3 is a histogram showing the probability distribution of rain attenuation for different dB values.

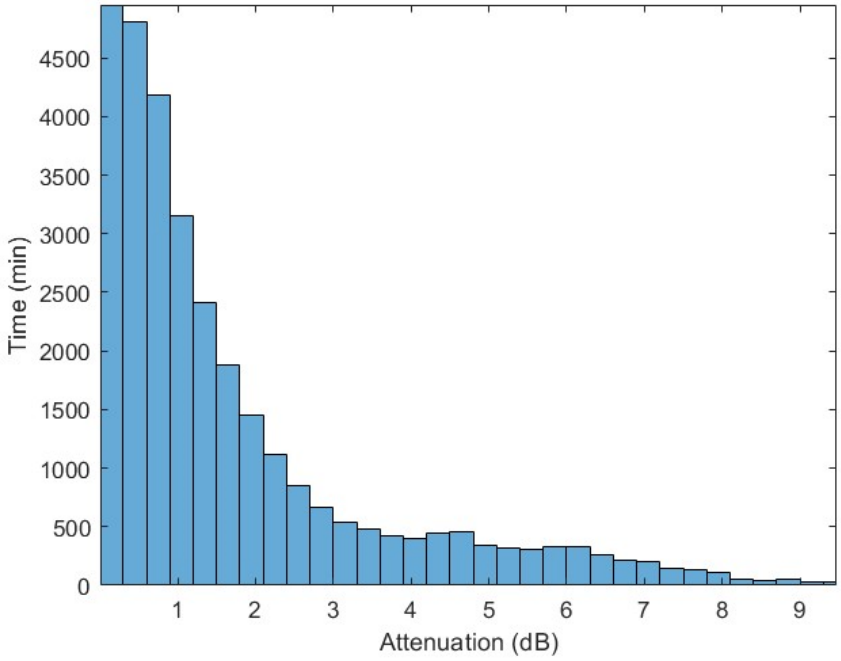

Figure 6.3 Probability distribution of measured rain attenuation

6.2 Rain Attenuation Modelling

6.2.1 Rain scattering characters

It has been introduced in chapter 2 that the specific rain attenuation could be calculated by the following the equation based on DSD model

$$\gamma = 4.343\int_0^\infty \delta_{ext}(D)N(D)dD \tag{2.16}$$

In this equation, δ_{ext} is extinction cross section for water drops of diameter D, N(D) is the drop size distribution value at diameter D. Depending on the value of size parameter $x=\pi D/\lambda$, where λ is the wavelength, the calculation of extinction cross section could be implemented by either Rayleigh scattering theory or Mie scattering theory. When the wavelength of radio wave λ is far larger than the diameter of scattering particles D, in this scenario are raindrops, the size parameter $x \ll 1$, most extinction is caused by Rayleigh scattering. When λ is similar to the diameter of scattering particles, Mie scattering occurs, and Mie theory is used to calculate the extinction cross section.

The extinction efficiency of Rayleigh scattering could be approximated as follows:

$$Q_{ext} = 4x\,\mathrm{Im}\left\{ l(1+\frac{lx^2(m^4+27m^2+38)}{15(2m^2+3)}) \right\} + \frac{8}{3}x^4\,\mathrm{Re}\left\{ l^2 \right\} \tag{6.1}$$

$$\text{where } l = \frac{m^2-1}{m^2+2}$$

m is the complex refractive index of water at 77.52 GHz, the value is 3.8528+2.0742j. Im and Re stand for the imaginary part and real part of the extinction efficiency, respectively.

The extinction efficiency of Mie scattering could be calculated as equation 6.2 to 6.4:

$$Q_{ext} = \frac{2}{x^2}\sum_{n=1}^{\infty}(2n+1)\,\mathrm{Re}\left\{ a_n + b_n \right\} \tag{6.2}$$

$$a_n = \frac{\psi_n'(mx)\psi_n(x) - m\psi_n(mx)\psi_n'(x)}{\psi_n'(mx)\xi_n(x) - m\psi_n(mx)\xi_n'(x)} \tag{6.3}$$

$$b_n = \frac{m\psi_n'(mx)\psi_n(x) - \psi_n(mx)\psi_n'(x)}{m\psi_n'(mx)\xi_n(x) - \psi_n(mx)\xi_n'(x)} \tag{6.4}$$

Where $\psi_n(x)$ and $\xi_n(x)$ are the Riccati-Bessel functions and can be expressed using spherical Bessel functions of the first kind and third kind as:

$$\psi_n(x) = \sqrt{\frac{\pi x}{2}} J_{n+\frac{1^x}{2}}$$

$$\xi_n(x) = \sqrt{\frac{\pi x}{2}} H_{n+\frac{1^x}{2}}$$

The extinction efficiency for Mie scattering and Rayleigh scattering theory are shown in figure 6.4:

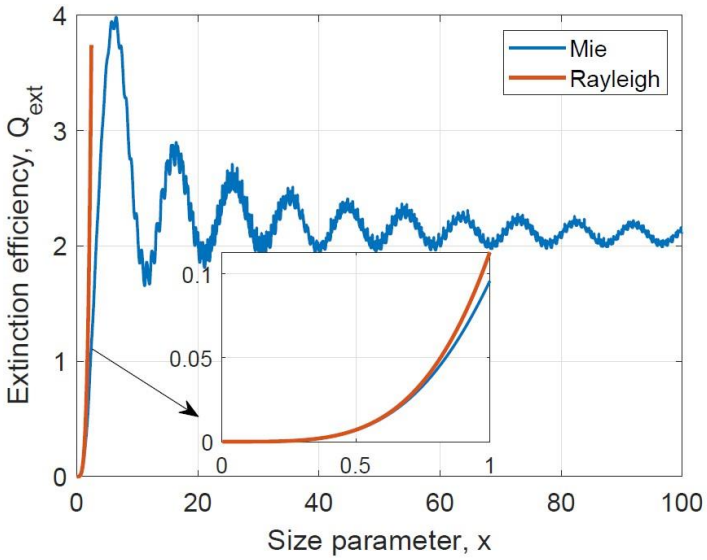

Figure 6.4 Extinction efficiency for Mie scattering and Rayleigh scattering

When x<0.6 the extinction efficiency of Mie scattering and Rayleigh scattering is similar, when x=0.6 the extinction efficiency reached to 1.4039 and when x>0.6 the extinction efficiency of Rayleigh scattering is monotonically increasing and the extinction efficiency of Mie scattering is fluctuating and approaching a certain value. In order to investigate what kind of scattering method need to be used to calculate the extinction efficiency, drop diameters for the whole year were analysed. The results are shown in table 6.1.

Table 6.1 Percentage of Rayleigh scattering (x<0.6) for 25.84 GHz and 77.52 GHz

Percentage (%) of Rayleigh scattering (x < 0.6)	25.84 GHz	77.52 GHz
January	75.20	22.23
February	63.83	12.65
March	72.20	11.01
April	82.42	8.91
May	87.34	8.91
June	87.04	16.84
July	77.68	10.63
August	86.88	13.06
September	89.03	16.51
October	86.03	15.35
November	84.73	11.64

December	85.82	9.73
whole year	78.95	12.84

The result shows that for the 77.52 GHz signal, Mie scattering contributes significantly more than Rayleigh scattering to the final rain attenuation. Because the wavelength of 77.52 GHz signal is 3.87 mm, which is similar to the rain drop diameter range. On the other hand, for the 25.84 GHz signal because the wavelength, which is 11.69 mm, is relatively larger to the rain drop diameter range, it means Rayleigh scattering method is more suitable for lower frequency and Mie scattering method is more suitable for higher frequency in calculations of the rain attenuation.

6.2.2 Wet antenna effect

After deciding the proper scattering methods to calculate the extinction efficiency for the 77.52 GHz signal and 25.84 GHz signal, another factor which influences the measured results are the wet antenna effect. It is caused by the water layer on the antennas. Wet antenna effect could introduce two kinds of deviations. Firstly, the water attached on the surface of the antenna can lead to an overall increase in attenuation. Transmitting signal could be absorbed and scattered by the water. Secondly, when precipitation stops, the attenuation of the signal may continue for some time due to the lingering effects of surface water attached on the antenna. This can cause a delay in the reflection of attenuation levels to accurately represent the real-time relationship between attenuation and precipitation.

The relationship of total attenuation and attenuation brought by wet antenna effect can be expressed by equation 6.5:

$$A_{total} = A_p + A_a \tag{6.5}$$

A_p stands for attenuation caused along the propagation path, A_a is the wet antenna attenuation which is proposed by the empirical relationship given in equation 6.6:

$$A_a = C(1 - e^{-dA_p}) \tag{6.6}$$

C and d are model parameters. The parameter is estimated by inspection of the

largest systematic differences between predictions and measurements and is calculated by nonlinear regression of the model in the observation period. In practice, the wet antenna effect is around 2 dB in similar links similar reported by A. Benarroch.[2] However, in this project, because of the shortness of the link (35 m), the wet antenna effect influences more on the measured data. To find the relationship between total attenuation and wet antenna attenuation, several rain events with extremely high rain rate are selected to maximize the wet antenna effect. Figure 6.5 shows the relationship between the estimated wet antenna effect and the measured rain attenuation.

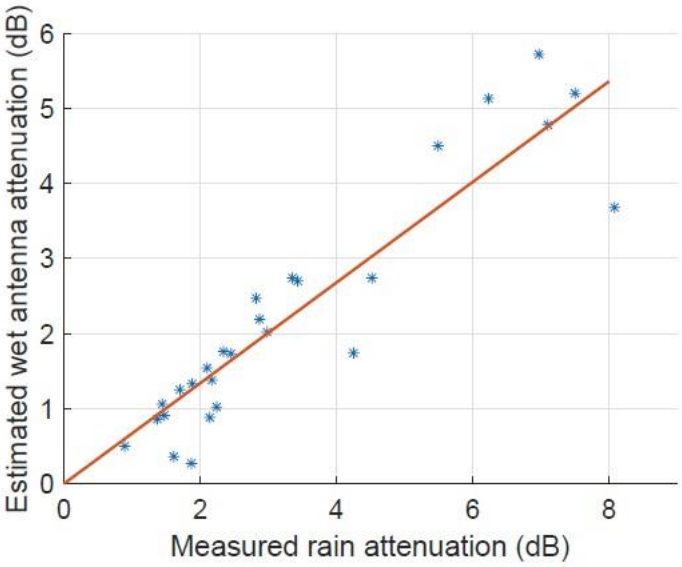

Figure 6.5 Relationship between estimated wet antenna effect and total attenuation

The figure surprisingly shows that the wet antenna attenuation is linear with the total measured data with a coefficient of 0.67, which means that the wet antenna effects introduce about 67% of total attenuation into the data.

To reduce the wet antenna attenuation, additional radomes have been installed at both the transmitter and receiver ends. Several pieces of fabrics are coated with super hydrophobic material and covered the front of the antennas for better weather-proofing effect. The fabrics are tested in the lab first to prevent possible attenuation on radio wave propagation. When rain hits the fabric cover, water tend to gather to a lager drop and fall to the ground quickly so that the influence of antenna wetness will be reduced.

Figure 6.6 shows the measured and estimated attenuation of a rain event on 30th of November, 2018 with the hydrophobic material cover.

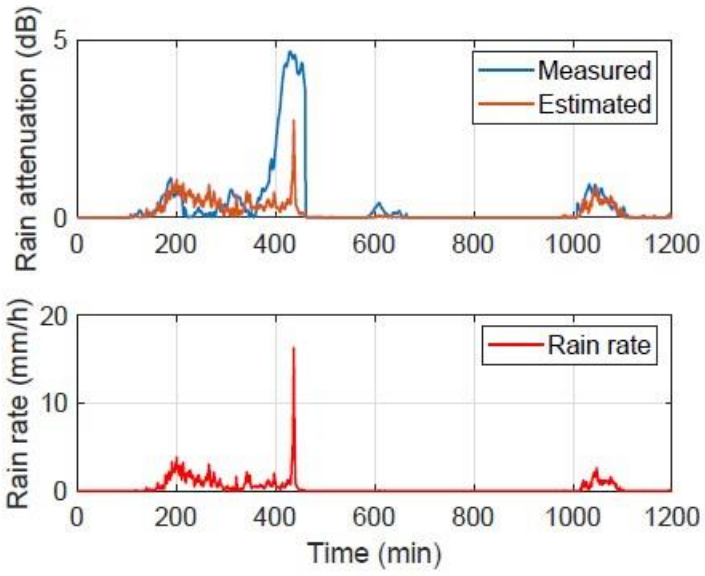

Figure 6.6 Measured and estimated attenuation with the hydrophobic material cover

In scenarios with similar rainfall intensities, the variance between the observed and the predicted results has been significantly reduced to a 2 dB range, a substantial enhancement from the original 5 dB gap that was noted before the introduction of the improved hydrophobic material cover. This reduction signifies a 3 dB decrease attributable to the wet antenna effect. At lower rainfall rates, such as less than 5 mm/h, the level of antenna wetness remains minimal, leading to a negligible divergence between the expected and the actual signal loss levels. However, under conditions of higher rainfall, for instance, at a rate of 16 mm/h, the influence of wet antennas on signal loss becomes comparable to that caused by rainfall itself, making it an essential factor to be integrated into the analytical process.

6.3 Summary

This chapter presents an analysis of rain attenuation focusing on the modelling and measurement of rain attenuation. Rain attenuation data was recorded from the 35-meter terrestrial link operating at 25.84 GHz (K-band) and 77.52 GHz (E-band). A correlation between signal power attenuation and rain rate is revealed, with signal power

decreasing in direct proportion to increasing rain intensity. The specific rain attenuation is calculated using both the DSD model with Mie scattering theory and the Rayleigh scattering theory, depending on the size parameter relative to the radio wave wavelength. This chapter demonstrated that Mie scattering dominated attenuation at 77.52 GHz due to the proximity of raindrop diameters to the wavelength, while Rayleigh scattering remained applicable for 25.84 GHz under low-intensity rainfall. A hybrid approach combining both methods achieved a prediction accuracy within 1.2dB of measured attenuation, outperforming the ITU-R P.530 model, which underestimated losses by up to 3.5dB for short links.

This chapter also addresses the wet antenna effect, which is shown to contribute significantly to the total attenuation, particularly at higher rain rates and provides a solution to significantly reduce the wet antenna effect by implementing hydrophobic radomes to cover both the transmitter and receiver ends.

6.4 References

[1] Recommendation ITU-R P.838.3: “Specific attenuation model for rain for use in prediction methods” ITU-R P. Ser., Geneva, Switzerland, ITU International Telecommunications Union, 2005.

[2] J. M. Garcia-Rubia, em. Riera, P. Garcia-del-Pino, and A. Benarroch, "Attenuation measurements and propagation modeling in the w-band," IEEE Transactions on Antennas and Propagation, vol. 61, no. 4, pp. 1860–1867, Apr. 2013.

Chapter7 Outdoor Directional Measurements in the V-Band

This chapter investigates the propagation characteristics of V-band frequencies (57-66 GHz) in outdoor environments. It includes measurements and analyses of path loss, reflection, diffraction, and scattering effects on radio signals. The focus is on understanding the behaviour of directional radio waves, which are crucial for the development of high-capacity, short-range communication links.

7.1 Experiment Setup

This measurement was performed using the same type of channel sounder introduced in chapter 3 with some modification on the transmitter and the receiver side. Dual channels RF heads were used for the capability of 2×2 multiple-in multiple-out (MIMO) measurements. At the transmitter a single pole double throw (SPDT) switch was used to switch the channels alternatively. The signal acquisitions operated simultaneously at the receiver with a dual channel 14-bit data acquisition card with a sampling rate of 40 MHz. Unlike the transmitter introduced in chapter 3, in which the band signal was up-converted to E-band, the band signal was up-converted by times 4 frequency multipliers to operate in the V-band within the frequency range of 50-75 GHz for this measurement. To be specifically, operating frequencies of this measurements were at the boundaries of the V-band in 51-57 GHz and 67-73 GHz respectively. Standard horn antennas were used at the transmitter with gain of 11 dBi at 52 GHz and 13 dBi at 67 GHz, with corresponding half power beam-widths of 53^{o} and 39^{o}. while the gain of the antennas at the receiver were 19 dBi at 52 GHz and 21 dBi at 67 GHz, with corresponding half power beam-widths of 19^{o} and 15^{o}.

Four links with different polarizations were set as: co-polarized links of vertical to vertical (V-V) and horizontal to horizontal (H-H), cross-polarized links of vertical to horizontal (V-H) and horizontal to vertical (H-V). Azimuthal directional measurements were achieved by mounting the receiver on a rotation table which is programmed to

rotate the full 360º in a 5º step angle. One second of data was recorded at each angle step.

Figure 7.1 shows the selected scenario for the measurement which represented a typical urban environment: a street canyon with some low-rise architectural obstacles.

Figure 7.1 Picture of the measurement scenario

During the measurements, the transmitter was positioned with its antennas elevated at a height of 3 meters to the ground and the antennas of the receiver were positioned at a height of 1.6 meters above the ground level. The receiver was mounted on a trolley and moved though predefined positions, which each spaced 6 meters apart from the others. Table 7.1 shows the parameters of experiment setup.

Table 7.1 Table of parameters of experiment setup

Frequency range	51-57 GHz	67-72 GHz
Sweep duration	819μs	
Sampling rate	40 MHz	
Record duration	1s	
Transmitter antenna	11 dBi; 53°	13 dBi; 39°
Receiver antenna	19 dBi; 19°	21 dBi; 15°
Link polarization	H-H; V-V; H-V; V-H	

7.2 Measurement Results

In this section, three main channel parameters delay spread, azimuth angular spread and path loss from the measurement are presented. These parameters could help to understand the spatial and temporal variation of signal channels. The parameters were calculated based on the recorded average power delay profile and power angular profile of the received signal.

7.2.1 Delay spread

The channel delay spread is a channel parameter which indicates the time dispersion of the channel due to multipath. The variation in path lengths results in signals arriving at different times. Usually two parameters are determined from the average power delay profile: the average delay τ_D and the rms delay spread S, which are the first and second moments of the power delay profile, respectively. These parameters are obtained from the following equations:

$$\tau_a = \frac{\int_{t_0}^{t_1} (\tau - \tau_a)\, p(\tau) d\tau}{\int_{t_0}^{t_1} p(\tau) d\tau} \tag{7.1}$$

$$S = \frac{\int_{t_0}^{t_1} (\tau - \tau D)^2 \, p(\tau) d\tau}{\int_{t_0}^{t_1} p(\tau) d\tau} \tag{7.2}$$

where $p(\tau)$ is the average power as a function of time delay, τ and t_0 is chosen before the arrival time of the first received echo, τ_a such that the magnitude of the power profile is insignificantly small. t_1 is the last time that the average power delay profile crosses a particular threshold level, which is chosen above the noise floor of the system. [1] In this measurement, the noise floor was adopted with a -20 dB threshold from the peak power.

For each angular direction, the estimated delay spread was classified into two categories: within-boresight (WBS) and out-of-boresight (OBS). The WBS classification applies when the main beams of both the transmitting and receiving antennas are aligned, indicating a direct and unobstructed line of sight. On the other hand, the OBS classification is used when the main beams of the antennas are not aligned, suggesting potential blockages or misalignments that may create multiple propagation path. Figure 7.2 shows the CDF of the estimated delay spread for (a) 51-57 GHz and (b) 67-73 GHz frequency bands.

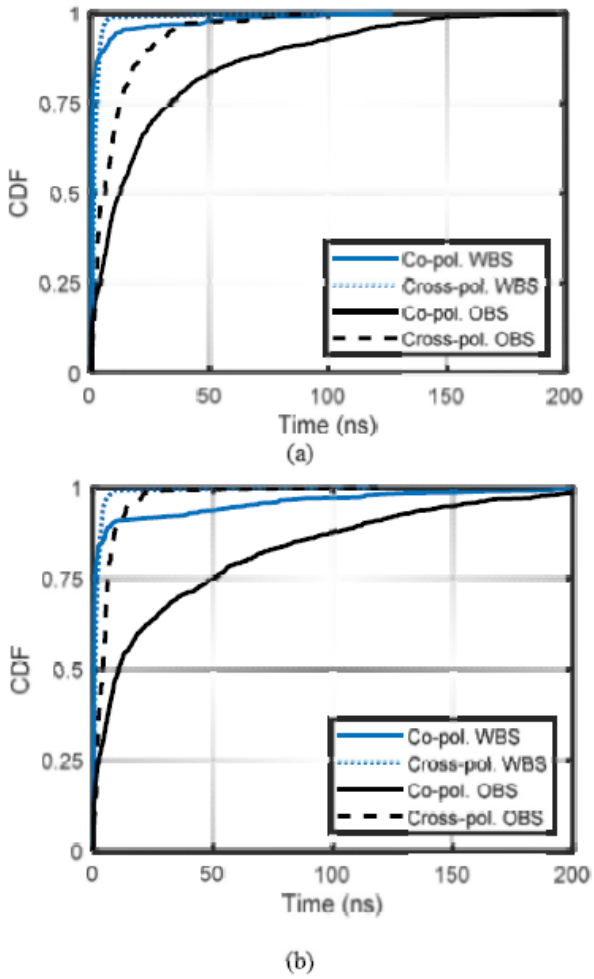

Figure 7.2 CDF of the delay spread for different frequency bands

Table 7.2 shows the delay spread values at the CDF level of 50% and 90% and the corresponding standard deviation.

Table 7.2 Statistics of the delay spread in ns

Beam direction	Link type	CDF: 50%; 90%; standard deviation	
		51-57 GHz	67-73 GHz
WBS	Co-polarization	0.7;6.6;14.5	0.6;8.2;30.8
	Cross-polarization	1.8;4.2;7.8	1.1;3.7;9.0
OBS	Co-polarization	12.4;80.3;36.6	11.0;112.7;50.6
	Cross-polarization	6.1;25.9;14.8	4.3;11.1;11.4

Table 7.2 indicates two facts, the first one is that the co-polarized links had less delay spread compared to the cross-polarized links. The second fact is WBS transmissions had less average delay spread compared to the OBS transmissions. The reason for that could be either a weak or absence of the direct component as result of the misalignment of the antennas main beam. [2]

7.2.2 Angular spread

The angular spread is an indicator of the incoming wave's dispersion. Given that the data were collected at a range of azimuth angles for the receiver, the angular spread of the incoming wave was estimated from the power angular profile (PAP) at each azimuth, in accordance with equation 7.3. [3] The power received at each azimuthal rotation is equivalent to the integral of the corresponding power delay profile.

$$\phi_s = \sqrt{\frac{\sum_{k=1}^{K} P_R(\phi_k)(\phi_k - \phi_m)^2}{\sum_{k=1}^{K} P_R(\phi_k)}} \tag{7.3}$$

$$\phi_m = \arg\left(\frac{\sum_{k=1}^{K} P_R(\phi_k) e^{i\phi_k}}{\sum_{k=1}^{K} P_R(\phi_k)}\right) \tag{7.4}$$

where K is the total number of angular positions, ϕ_k is the corresponding angle, in radian, and ϕ_m is the average azimuthal arrival angle. The angles are restricted between -180^o to 180^o.

Figure 7.3 shows the CDF of the estimated angular spread values of the co-polarized and cross-polarized links for each frequency band.

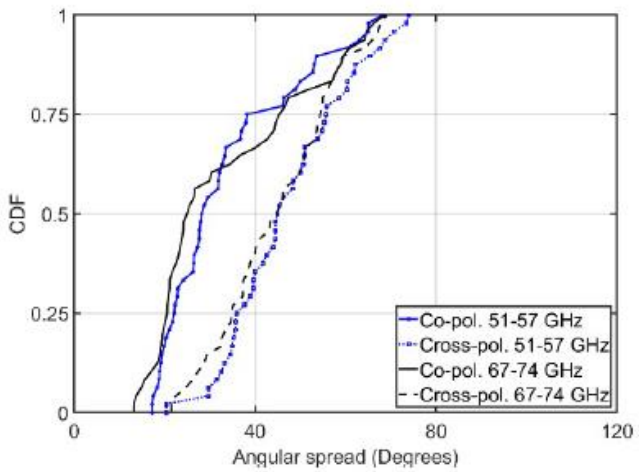

Figure 7.3 CDF of the angular spread for different frequency bands

Table 7.3 shows the angular spread values at the CDF level of 50% and 90% and the corresponding standard deviation.

Table 7.3 Statistics of the angular spread in degrees

CDF: 50%; 90%; standard deviation		
Frequency	Co-polarization	Cross-polarization
51-57 GHz	28.2;54.9;14.6	44.9;65.9;12.8
67-73 GHz	24.9;59.7;16.8	44.6;60.4;12.7

The table shows that the co-polarized links had lower average angular spreads compared with their corresponding cross-polarized links. The observed effect could be attributed to the propensity of power distribution to exhibit a more even pattern across the various angles of incidence for the cross-polarized signals.

7.2.3 Path loss

Path loss is an important parameter in wireless communication systems. It presents the attenuation that the wave experience as it propagates through a particular environment. The log-distance model, which is only depend on frequency and distance, was chosen for this measurement due to its concision. The model is shown in equation 7.5:

$$PL(d) = PL_0 + 10n\log_{10}(d) \tag{7.5}$$

where PL_o stands for the path loss intercept ,in dB, and n stands for the dimensionless path loss exponent. Both PL_o and n are estimated through the linear least square regression method which has been discussed in chapter 5.

Measured path loss data were computed from the synthesized omnidirectional received power, which is the integral of the received power in power angular profile, at each location. [4] Figure 7.4 shows the estimated path loss of the co-polarized links and cross-polarized links.

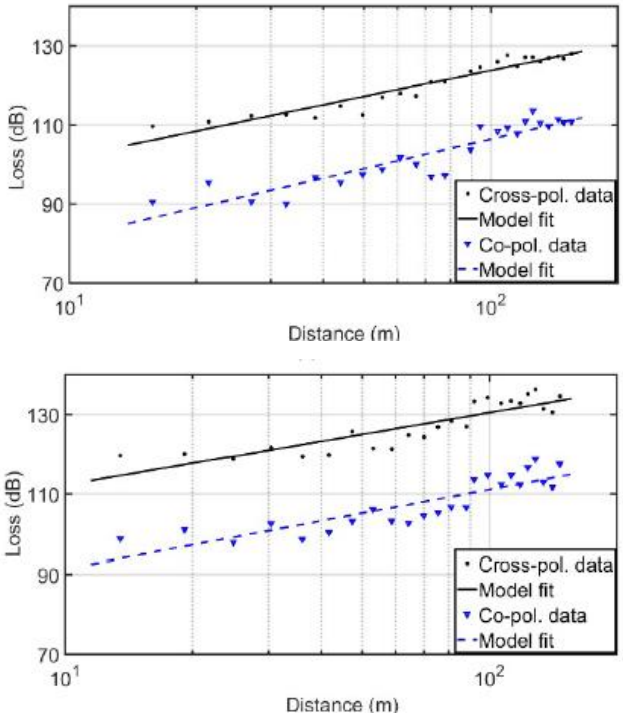

Figure 7.4 Path loss at 51-57 GHz and 67-73 GHz

Figure 7.4 indicates that the co-polarized links had around 10 dB less path loss than the corresponding cross-polarized links. It is caused by the mismatch of the polarization. The fitting results for log-distance path loss model parameters are given in table 7.4.

Table 7.4 Fitting parameters for log-distance model

Model parameters: n, $PL_{o,,}$ standard deviation		
Frequency	Co-polarization	Cross-polarization

51-57 GHz	2.4;56.8;3.0	2.2;79.9;1.8
67-73 GHz	2.0;71.5;3.2	1.8;94.1;2.9

7.3 Summary

This chapter presented a deep investigation into the propagation characteristics of V - band frequencies (57 - 66 GHz) in outdoor environments. The research aimed to understand the behaviour of directional radio waves, which is of great significance for the development of high-capacity, short-range communication links.

The experiment setup was carefully designed. A modified version of the channel sounder introduced in Chapter 3 was utilized. Dual channels RF heads were employed to enable 2×2 MIMO measurements. At the transmitter, a single pole double throw switch was installed to alternate the channels, and the signal acquisitions at the receiver were carried out simultaneously using a dual-channel 14-bit data acquisition card with a sampling rate of 40 MHz. Standard horn antennas with different gains and half-power beam-widths were used at both the transmitter and the receiver. Four links with different polarizations were set up. Azimuthal directional measurements were achieved by mounting the receiver on a rotation table, which was programmed to rotate 360° in 5° step angles, and one second of data was recorded at each angle step. The transmitter and receiver were positioned at specific heights, and the receiver was moved through predefined positions spaced 6 meters apart.

From the measurement results, three main channel parameters were analysed: delay spread, azimuth angular spread, and path loss. The channel delay spread, which indicates the time dispersion of the channel due to multipath, was calculated from the average power delay profile. The results showed that co-polarized links had less delay spread compared to cross-polarized links, and within-boresight transmissions had less average delay spread than out-of-boresight transmissions. The angular spread, an indicator of the incoming wave's dispersion, was estimated from the power angular profile. It was found that co-polarized links had lower average angular spreads compared with their corresponding cross-polarized links. Path loss, an important

parameter in wireless communication systems, was measured and analysed using the log-distance model. The co-polarized links had around 10 dB less path loss than the corresponding cross-polarized links due to polarization mismatch.

This chapter provided valuable empirical data on V-band radio wave propagation in outdoor environments. This data is essential for validating and improving existing propagation models, as well as for the design of V-band communication systems. The analysis of the three key channel parameters also offered insights into the spatial and temporal variation of signal channels. Understanding these variations is crucial for optimizing communication link performance, such as reducing interference and improving signal quality. Finally, the findings on the differences in delay spread, angular spread, and path loss between different polarization links can guide the selection of polarization configurations in practical communication systems, enhancing system efficiency and reliability. Overall, this chapter significantly advanced the understanding of radio wave behaviour in the V-band, which is vital for the development of future high - speed, short - range communication technologies.

7.4 References

[1] Salous, S. "Measurement of multipath delay statistics over a 72‐to 90 ㎝ Hz bandwidth at 1.8 GHz in two European cities using a chirp sounder." Radio Science 34.4(2016):797-816.

[2] Raimundo, X., S. Salous, and A. A. Cheema. "Indoor radio propagation measurements in the V-band." Radio Propagation and Technologies for 5G (2016) IET, 2016.

[3] Piersanti, Stefano, L. A. Annoni, and D. Cassioli. "Millimeter waves channel measurements and path loss models." 2012 IEEE International Conference on Communications (ICC) IEEE, 2012.

[4] Sun, Shu , et al. "Synthesizing Omnidirectional Antenna Patterns, Received Power and Path Loss from Directional Antennas for 5G Millimeter-Wave Communications." IEEE (2016).

Chapter8 Conclusions and Future Work

8.1 Conclusions

The primary objective of this thesis is to investigate the impact of precipitation events, particularly rain, on radio wave propagation, especially for millimetre wave. Three main research interests: precipitation statistical study, drop size distribution analysis and rain attenuation modelling are introduced combined with both hardware and software designing and coding.

On precipitation analysis part, as described in Chapter 4, one year of precipitation data from January 2018 to January 2019 was acquired by PWS100 laser disdrometer. This data was processed to meet the high - standard requirements of the ITU Study Group 3 databanks, contributing to a comprehensive evaluation of rain-related parameters. Rain intensity, a crucial parameter for rain attenuation research, was analysed. Complementary cumulative distribution functions of rain intensity were calculated and clearly depicted the distribution of rain intensities each month in 2018. Through annual rain intensity analysis and worst-month analysis, it was found that the majority of rain events in the Durham region exhibited intensities below 50 mm/h, and the worst month in 2018 was July, with a maximum rain intensity exceeding 150 mm/h. Rain duration was another parameter under study. The relationship between rain intensity and duration was explored, and it was found that, generally, long - duration precipitation events tended to have lower intensities. The total duration of rain events with intensities greater than 0.2 mm/h in 2018 was 24931 minutes, and most of the time, rain intensity was less than 50 mm/h. The number of rain events was also analysed, and it was shown that 60% of total detected rain events had average rain intensity between 5 - 10 mm/h, while only 7% had average rain intensity higher than 40 mm/h.

Rain drop size distribution was a key aspect of the precipitation analysis. It provided detailed micro-structure information about rainfall. The DSD was calculated using the data from the PWS100 disdrometer, with the number of raindrops recorded and separated into 300 slots based on diameter The average velocity of raindrops was

estimated using a theoretical relationship with drop diameter for DSD computation. Monthly and annual DSDs were presented in Figures 4.6 and 4.7 respectively, and it was found that the peak DSD occurred around a rain drop size of 0.7 mm. To further understand the DSD, several distribution models were applied, as described in Chapter 5. The Marshall-Palmer exponential distribution model, log-normal distribution model, and gamma distribution model were compared. The Marshall-Palmer model, though simple for calculations, had limitations in presenting the number of small rain drops with diameters less than 1.5 mm compared to the actual measured data. The log-normal distribution model could capture the skewness of raindrop size distributions, but at certain rain rates, the fitted models had issues similar to the exponential model. The gamma distribution model, with its flexible curve shape due to the gamma function, was shown to be superior in adapting to the observed DSD data. It could better capture the skewed drop populations of convective rain and the narrow spectrum of stratiform events. This finding, as stated in Chapter 4, indicated the necessity of region-specific model calibration, especially in temperate climates like Durham with mixed precipitation types.

Regarding the rain attenuation model study, a 35-meter terrestrial link operating at 25.84 GHz (K - band) and 77.52 GHz (E - band) was established, as detailed in Chapter 3. Over the course of one year measurements from January 2018 to January 2019, a significant amount of data was collected and analysed, following the requirements of ITU recommendations to ensure reliable statistical results. The widely used ITU-R P.530 model was evaluated in the context of this short-range link. It was found that this model had limitations for short links. The ITU-R P.530 model is based on long - term rain rate data and specific rain attenuation equations. However, for short links, its assumptions, such as a uniform rain cell structure, lead to inaccurate estimations. In contrast, the DSD model, which uses raindrop size distribution and Mie scattering method to calculate attenuation, was found to be more suitable. The DSD model takes into account the "wet antenna effects", an additional attenuation caused by the water layer covered on the antennas. As shown in Chapter 6, this effect can significantly influence the measured attenuation, especially in short links. In this project, due to the

short 35 - meter link, the wet antenna effect was found to contribute about 67% of the total attenuation, as indicated by the linear relationship between the estimated wet antenna effect and the measured rain attenuation. To mitigate this effect, hydrophobic radomes were installed at both the transmitter and receiver ends, and super-hydrophobic-coated fabrics were used to cover the antennas. This effectively reduced the wet antenna effect, as demonstrated by the reduction in the variance between observed and predicted attenuation results.

Furthermore, the choice of scattering methods for calculating rain attenuation was investigated. Depending on the relationship between the diameter of raindrops and the wavelength of the radio wave, either Rayleigh scattering or Mie scattering was applicable. For the 77.52 GHz signal, since its wavelength (3.87 mm) is similar to the rain drop diameter range, Mie scattering contributed significantly more to the final rain attenuation. In contrast, for the 25.84 GHz signal with a relatively larger wavelength (11.69 mm) compared to the rain drop diameter range, Rayleigh scattering was more suitable under low-intensity rainfall conditions. A hybrid approach combining both methods achieved a prediction accuracy within 1.2 dB of the measured attenuation, outperforming the ITU - R P.530 model, which underestimated losses by up to 3.5 dB for short links.

Some outdoor directional measurements in the V - band (57 - 66 GHz) were conducted in this research as well. Using a modified channel sounder, parameters like delay spread, angular spread, and path loss were measured. The results showed that co - polarized links had less delay spread and angular spread, and lower path loss compared to cross - polarized links, providing valuable data for V - band communication system design.

The research emphasizes the significance of understanding rain characteristics and scattering effects, essential for improving the reliability and efficiency of communication systems, especially at higher frequencies and in complex weather conditions.

8.2 Future Work

Although this project is finished productively, it is just a start for understanding the rain influence on millimetre wave propagation. Several new upgrades have been done including a new IF head to simplify the sounding system. By reducing the numbers of wires, a lot of connection problems could be avoided and the reliability of the system will be increased. Also, a side link is planned to be set up with an angle of the main link to get the scattering signal and study the potential of multi-scattering propagation characters.

Several other ideas could be implemented as well such as extending the length of propagation path to get clear attenuation data; use enhanced modelling methods like neural networks and deep learning technology; the frequency and bandwidth could be expanded to meet the industry requirements of 5G networks. Combine research with other possible environmental attenuation factors like wind speed, temperature and fog or cloud. This project has a potential to make a significant contribution to the next generation communication network.

Appendix A Verilog code for FPGA

```
//code fot time synchronization

module TimeSyncAdnan( dclk,pps,rclk,fswitch,temp1, temp2, temp3, temp4);

input dclk,rclk,pps, fswitch ;
output temp1, temp2, temp3, temp4;

reg triggerOut,triggerdelay, triggerhalf, triggerquarter ;
reg flagdelay,flagdcountr;
reg control;
reg rclkl;
wire clk;
reg temp1, temp2, temp3, temp4;
integer dcountr, dcountr1, dcountr2, dcountr3, dcountr4, dcountr5, dcountr6 ;
integer delay;

initial
begin
rclkl=1'b0;
triggerOut = 1'b0 ;
triggerdelay= 1'b0;
triggerhalf = 1'b0;
triggerquarter = 1'b0;
flagdelay = 1'b0;
control = 1'b1;
flagdcountr = 1'b0;
dcountr    = 0 ;
```

```
dcountr1 = 0 ;
dcountr2 = 0;
dcountr3 = 0;
dcountr4 = 0;
dcountr5 = 0;
dcountr6 = 0;
delay = 20 ; // add delay value
end
always @(posedge rclk)// 10MHz to 500Hz
begin
dcountr6=dcountr6 + 1;
if(dcountr6 == 10000)
begin
rclkl=1'b1;
end
if(dcountr6 == 20000)
begin
rclkl=1'b0;
dcountr6=0;
end
end
//assign clk=rclkl;
//assign clk=fswitch?rclkl:dclk;
//always @(posedge pps or negedge flagdcountr)//pps
//begin
//        if(!flagdcountr)begin
//                control=1'b0;
//              end
//        else begin
//                control=1'b1;
```

```
//          end
//end
//
//always @ (posedge clk)//counter
//begin
//if(control==1'b1)
//begin
//dcountr3 = dcountr3 + 1;
//flagdcountr=1'b1;
//if (dcountr3 == 500000)
//begin
//dcountr3 = 0;
//flagdcountr=1'b0;
//end
//end
//if (control==1'b0)
//begin
//dcountr4 = dcountr4 + 1;
//if (dcountr4 == 10)
//begin
//dcountr4=0;
//flagdcountr=1'b1;
//end
//end
//end
always @ (posedge dclk)//triggerOut
begin
      if ( control == 1)
    begin
    dcountr = dcountr + 1 ;
```

```
            if ( dcountr == 860)
            begin
            triggerOut= 1'b1;
            end
            if ( dcountr == 1720 )
            begin
            triggerOut=1'b0;
            dcountr = 0;
            end
        end
    end
    always @ (posedge dclk)//triggerdelay
    begin
         if ( control== 1)
         begin
        dcountr1 = dcountr1 + 1 ;
        if ( dcountr1 == 860 && ~flagdelay )
        begin
        dcountr1 = dcountr1 - delay ;
        flagdelay = 1'b1;
        end
              if ( dcountr1 == 860)
            begin
            triggerdelay = 1'b1;
            end

            if ( dcountr1 == 1720 )
            begin
            triggerdelay = 1'b0;
            dcountr1 = 0;
```

```
            end
        end
    end
    always @ (posedge dclk)//divide by 2
    begin
         if ( control == 1)
         begin
        dcountr2 = dcountr2 + 1 ;
            if ( dcountr2 == 1720)
            begin
            triggerhalf = 1'b1;
            end

            if ( dcountr2 == 3440 )
            begin
            triggerhalf = 1'b0;
            dcountr2 = 0;
            end
        end
    end
    //always @ (posedge dclk)//divide by 4
    //begin
    //       if ( control == 1)
    //      begin
    //      dcountr5 = dcountr5 + 1 ;
    //          if ( dcountr5 == 3440)
    //          begin
    //            triggerquarter= 1'b1;
    //          end
    //
```

```
//          if ( dcountr5 == 6880)
//          begin
//            triggerquarter=1'b0;
//          dcountr5 = 0;
//          end
//     end
//end
always @ (posedge rclk)
begin
temp1= triggerOut;
temp2= triggerdelay;
temp3= triggerhalf;
temp4= fswitch?triggerOut:rclkl;
//temp4 = rclkl;
end
endmodule
```

Appendix B C++ Code to Record Attenuation Data

```
#include "stdafx.h"
#include <windows.h> // for time
#include <stdio.h>    // for time
#include <string.h>
#include <sstream>
#include <conio.h>
#include <cstdlib>

#include <direct.h>
#include<sys/stat.h>
#include<sys/types.h>
//#define MY_ACQ_BRD_NUM              2              // first board in system
#define MY_SAMPLING_RATE_MHZ    40             // 40 MHz

double ClkRate;
//#define CONNECT_TO_REMOTE_DEVICE

#ifdef CONNECT_TO_REMOTE_DEVICE
#define MY_REMOTE_SERVER_ADDR           "127.0.0.1"
#define MY_REMOTE_SERVER_PORT
PX14_SERVER_PREFERRED_PORT
#endif

// Initialize data acquisition settings
static int AcqDeviceSetup (HPX14 hBrd2,int MY_ACQ_BRD);
// Main recording function
//static int RecordingMain (HPX14 hBrd,HPX14 hBrd2, int argc, char* argv[]);
```

```
static int RecordingMain (HPX14 hBrd2, int argc, char* MainFolder,char* Filename,int MY_ACQ_BRD);
#define DUMP_SAMPLES                    16    // added

void clearScreen(void);
int real_main(int argc, char* argv[])
{

    unsigned int serial_num;
    HPX14 hBrd2;
       hBrd2= PX14_INVALID_HANDLE;
    int res;
    char choose= '1';
    int MY_ACQ_BRD_NUM = 1;
    unsigned int FileNum = 1; //1440 for 24 hours

    char pDestFolder[45];    // Link into the destination folder
    char foldername[45];

    char ptemp[20];    // keep track of the file name
    char temp[10];    // keep track of the file number
    char ptemp2[30]; // keep track of the file number

    int ix; // Keep track of error on Record and Setting functions

    clearScreen();
    printf ("Press ESC to quit or Any other key to continue\n");
    if (27 == _getch())
        return 0;
    printf ("\nConnecting to PX14400 device(s)...\n");
```

```
        res = ConnectToDevicePX14(&hBrd2, MY_ACQ_BRD_NUM); // Connected to the second card Master

        if (SIG_SUCCESS != res)
        {
            DumpLibErrorPX14(res, "Failed to connect to PX14400 device: ");
            return -1;
        }

        fflush(stdin);
        printf("\n Data Saving Folder Location:");
        printf("\n please input the Main folder Name where data is to be saved: ");
            gets(foldername);    // the name of Main folder
        printf("\n please input the file name:      ");
            gets(ptemp);    // Name of the files

        if(!_mkdir(foldername))
              printf("Folder %s has been created\n", foldername);
          else
              printf("Folder has not been created it may alread exist in the distination drive\n");


        printf ("\nDo you like to Stop now\n");
        printf ("Press ESC to quit the program or Any other key to continue\n");
        if (27 == _getch())
            return 0;


        GetSerialNumberPX14(hBrd2, &serial_num);
```

```
printf (" - Connected to PX14400 #%u - Card 1\n", serial_num);


// Initialize data acquisition hardware settings
printf ("Initializing hardware settings...\n");

res = AcqDeviceSetup(hBrd2,MY_ACQ_BRD_NUM);    // Hardware settings

if (SIG_SUCCESS != res)
{
    DisconnectFromDevicePX14(hBrd2);      // Disconnect from the device
    return -1;
}
        Sleep (1000);
clearScreen();
printf("\n\n Enter 'an interger' duration of the measurement in minutes: \n");
printf("      Note: At Each minute a 1s data file will be recorded\n ");
printf("Examples:30 min = 30 ; 24 hour = 1440 ; 4days = 5760;");
printf("Make sure the storage space is sufficient for the data you trying to
record '1s' data is approx. 160Mbit for each Card;");
printf("\n Enter record duration:");
scanf("%d", &FileNum);
printf("\n You have chosen to record for %d minutes",FileNum);
    Sleep (2000);
clearScreen();
// Loops for record the files
 SYSTEMTIME    lt, ltp;
 printf("\n Data acquisition in process ...\n");
  GetLocalTime(&ltp);
 printf (" Time %d : %d (hh:mm) \n", ltp.wHour, ltp.wMinute) ;
```

```
        for ( unsigned int counter = 1; counter <=FileNum ; counter++ )
        {
            if((counter%5)==0)
            {          printf ("\n    DisConnecting to PX14400 device(s)...\n");
                      res=DisconnectFromDevicePX14(hBrd2);
                     if (SIG_SUCCESS != res)
                        {
                            DumpLibErrorPX14(res, "Failed to disconnect to PX14400
device: ");
                            return -1;
                        }
                              Sleep(5000);
                              printf ("\nConnecting to PX14400 device(s)...\n");
                               Sleep(10000);
                       res = ConnectToDevicePX14(&hBrd2, MY_ACQ_BRD_NUM);
// Connected to the second card Master
                        if (SIG_SUCCESS != res)
                        {
                            DumpLibErrorPX14(res, "Failed to connect to PX14400
device: ");
                            return -1;
                        }
                }

                itoa(counter, temp, 10); // int to string

                 sprintf(ptemp2,"%s_%s",ptemp,temp );    //File name concatinated with
the file number
```

```
            clearScreen();
          // Loops for record the files
           printf("\n Data acquisition in process ...\n");
           // start of acquisition
              // Setup and run the recording

               // RecordingMain(hBrd,hBrd2, 2, argv); // Calling the record function

               res= RecordingMain(hBrd2, 2, foldername,
ptemp2,MY_ACQ_BRD_NUM); // Calling the record function
                 if (SIG_SUCCESS != res)
                   {
                      DumpLibErrorPX14(res, "Failed to disconnect to PX14400
device: ");
                      return -1;
                   }

              //       ix= RecordingMain(hBrd2, 2, foldername,
ptemp2,MY_ACQ_BRD_NUM); // Calling the record function
                // if(ix==-1){
              //        printf ("/n An Error has occured\n");
                 //        break;
              // }

              if (_kbhit() && 27==_getch())
                   {   break;    // Coming out of the loop by pressing the escape button
                   }
                GetLocalTime(&lt);
              printf( "Recorded File number %d of Total number of files %d -
",counter, FileNum);
```

```
                printf ("Time    %d : %d (hh:mm) \n", lt.wHour, lt.wMinute) ;


            while(1)
            {
                GetLocalTime(&lt);
        //      printf ("Time    %d : %d (hh:mm)", lt.wHour, lt.wMinute) ;
                if( lt.wMinute == 0 )
                {
                    lt.wMinute = 60 ;
                }
                if ( ltp.wMinute+1 == lt.wMinute ) // +1 means i minute difference from previous measurements
                {
                        ltp.wMinute = lt.wMinute ;
                    if( ltp.wMinute == 60 )
                    {
                        ltp.wMinute = 0 ;
                    }
                       break ;
                }
            }

        //printf ("Time    %d : %d (hh:mm) \n", lt.wHour, lt.wMinute) ;

    }
      printf("\n Data Acquisition Finished ...\n");
    // Ensure that board is idle

    SetOperatingModePX14(hBrd2, PX14MODE_STANDBY);
```

```
    // Disconnect from hardware.
    DisconnectFromDevicePX14(hBrd2);

return 0;
}

int main(int argc, char* argv[])
{
    int res;

    res = real_main(argc, argv);
    printf ("Press any key to exit...\n");
    _getch();

    return res;
}

int AcqDeviceSetup (HPX14 hBrd2,int MY_ACQ_BRD)
{
    int res,res2;
    char choose= '1';

#if defined(MY_SAMPLING_RATE_MHZ)
    ClkRate = MY_SAMPLING_RATE_MHZ;
#else
    // Determine our acquisition rate
    printf ("Acquisition rate in MHz [20.0, 400.0]? ");
    if (!scanf("%lf", &ClkRate))
    {
        printf ("Umm, what?");
```

```
        return -1;
    }
#endif
    //printf (" - Acquisition rate: %0.3f MHz\n", ClkRate);

    // Reset all hardware settings to default values

     res2 = SetPowerupDefaultsPX14(hBrd2);
    if (SIG_SUCCESS != res2)
    {   DumpLibErrorPX14(res2, "Failed to set powerup defaults: ", hBrd2);
        return -1;}

        Sleep (2000);
    clearScreen();
                    // Activating the Channels
    printf("\n Channel(s) selection ...\n");

        res2 = SetActiveChannelsPX14 (hBrd2, 0 ); // Set both channels "on"
    if (SIG_SUCCESS == res2)
          printf(" - Card-2 Channel 1 and Channel 2 are actives\n");
    else {
        DumpLibErrorPX14(res2, "Failed to set powerup defaults: ", hBrd2);
        return -1;     }

        Sleep (2000);
    clearScreen();
    printf("\n         Clock Source Settings ...\n");

       res2 = SetAdcClockSourcePX14 (hBrd2, 0 ); // Set both channels "on"
    if (SIG_SUCCESS == res2)
```

```
            printf(" - Card-2 internal clock\n");
        else {
            DumpLibErrorPX14(res2, "Failed to set clock source: ", hBrd2);
            return -1;
        }

            // locking to external 10 MHz
        printf("\n         Locking to external clock Settings ...\n");
          res2 = SetInternalAdcClockReferencePX14 (hBrd2, 1 ); // Set both channels
"on"
        if (SIG_SUCCESS == res2)
            printf(" - Card-2 lock the external clock\n");
        else {
            DumpLibErrorPX14(res2, "Failed to lock into external clock: ", hBrd2);
            return -1;
        }
            Sleep (2000);
        clearScreen();

        printf("\n         Set the Sampling rate ...\n");

        printf("\n Choose the Sampling rate for the 'Card 1' and 'Card 2' By Selecting
the follwing intergers \n");
        printf("\n     1 - fs = 10 MHz \n     2 - fs = 20 MHz   \n     3 - fs = 30 MHz
\n     ");
        printf("4 - fs = 40 MHz   \n     5 - fs = 50 MHz   \n     6 - fs = 80 MHz   \n
Default - fs = 40 MHz");
        printf("\n Enter your selection:");
        choose=_getch();
        switch(choose)
```

```
{
case '1':
    {   ClkRate = 10.0;
    break;}
case '2':
    {   ClkRate = 20.0;
    break;}
case '3':
    { ClkRate = 30.0;
    break;}
case '4':
    { ClkRate = 40.0;
    break;}
case '5':
    {ClkRate = 50.0;
    break;}
case '6':
    {   ClkRate = 80.0;

    break;}
default:
    { ClkRate = 40.0;
    break;}
}
  res2 = SetInternalAdcClockRatePX14(hBrd2, ClkRate); // Set both channels
"on"

if (SIG_SUCCESS == res2)
    printf("\n You have choosen %4.2f MHz sampling rate for Card
2",ClkRate);
```

```
else {
      DumpLibErrorPX14(res2, "Failed to set clock rate: ", hBrd2);
      return -1;
}
      Sleep (2000);
       clearScreen();
       printf("\n          Trigger Source Settings ...\n");
// Trigger from External

     res2 = SetTriggerSourcePX14 (hBrd2, PX14TRIGSRC_INT_CH1); //
if (SIG_SUCCESS == res2)
          printf(" - Card-2 set to be triggered from External source\n");
else {
      DumpLibErrorPX14(res2, "Failed to set the triggered source: ", hBrd2);
      return -1;
}

//Post trigger

     res2 = SetTriggerModePX14 (hBrd2, 0 ); // Set both channels "on"
if (SIG_SUCCESS == res2)
          printf(" - Card-2 configured to post trigger\n");
else {
      DumpLibErrorPX14(res2, "Failed to configure the post trigger: ", hBrd2);
      return -1;
}
Sleep (2000);
     clearScreen();
// set vertical range to 220 mVpp
//printf("\n Vertical-Range selection ...\n");
```

```
// Added for user selection

printf("\n\n\n Choose the Vertival range Vpp for the 'Card 2' By Selecting the follwing intergers \n");
printf("\n 1 - Vpp = 0.220 V \n 2 - Vpp = 0.439 V \n 3 - Vpp = 0.696 V \n ");
printf("4 - Vpp = 1.103 V \n 5 - Vpp = 2.20 V \n 6 - Vpp = 3.487 V \n Default - Vpp = 0.311 V");
printf("\n Enter your selection:");
choose=_getch();
switch(choose)
{
case '1':
{res = SetInputVoltRangeCh1PX14 (hBrd2, PX14VOLTRNG_0_220_VPP);
res2 = SetInputVoltRangeCh2PX14 (hBrd2, PX14VOLTRNG_0_220_VPP);
printf("\n You have selected %c for the Card 2",choose);
break;}
case '2':
{res = SetInputVoltRangeCh1PX14 (hBrd2, PX14VOLTRNG_0_439_VPP);
res2 = SetInputVoltRangeCh2PX14 (hBrd2, PX14VOLTRNG_0_439_VPP);
printf("\n You have selected %c for the Card 2",choose);
break;}
case '3':
{res = SetInputVoltRangeCh1PX14 (hBrd2, PX14VOLTRNG_0_696_VPP);
```

```
                res2 = SetInputVoltRangeCh2PX14 (hBrd2,
PX14VOLTRNG_0_696_VPP);
                printf("\n You have selected %c for the Card 2",choose);
               break;}
          case '4':
               {res = SetInputVoltRangeCh1PX14 (hBrd2,
PX14VOLTRNG_1_103_VPP);
                res2 = SetInputVoltRangeCh2PX14 (hBrd2,
PX14VOLTRNG_1_103_VPP);
                printf("\n You have selected %c for the Card 2",choose);
               break;}
          case '5':
               {res = SetInputVoltRangeCh1PX14 (hBrd2,
PX14VOLTRNG_2_200_VPP);
                res2 = SetInputVoltRangeCh2PX14 (hBrd2,
PX14VOLTRNG_2_200_VPP);
                printf("\n You have selected %c for the Card 2",choose);
               break;}
          case '6':
               {res = SetInputVoltRangeCh1PX14 (hBrd2,
PX14VOLTRNG_3_487_VPP);
                res2 = SetInputVoltRangeCh2PX14 (hBrd2,
PX14VOLTRNG_3_487_VPP);
                printf("\n You have selected %c for the Card 2",choose);
               break;}
          default:
               {res = SetInputVoltRangeCh1PX14 (hBrd2,
PX14VOLTRNG_0_311_VPP);
                res2 = SetInputVoltRangeCh2PX14 (hBrd2,
PX14VOLTRNG_0_311_VPP);
```

```
            printf("\n You have selected default for the Card 2");
            break;}
        }


        if (SIG_SUCCESS != res2)
            {
            DumpLibErrorPX14(res, "Card 2 - failed to set CH2 vertical range : ", hBrd2);
            return -1;
           }
            Sleep (1000);
        return SIG_SUCCESS;
    }

    //int RecordingMain (HPX14 hBrd,HPX14 hBrd2, int argc, char* argv[])
    int RecordingMain (HPX14 hBrd, int argc, char* MainFolder,char* Filename,int MY_ACQ_BRD)
    {           //RecordingMain(hBrd,hBrd2, 2, foldername,ptemp2); // Calling the record function
        HPX14RECORDING hRec2;
        bool bDone, bDone2;
        int res;
        int i; // added
        unsigned long ACQUISITION_SAMPLES;

        char pDestFile[75];

         ACQUISITION_SAMPLES = ClkRate*1e6*2;
         sprintf(pDestFile,"%s\\%s.rd16",MainFolder,Filename);
```

```
        if (_kbhit() && 27==_getch())
        {       return SIG_SUCCESS;     // Get out of the Loop
        }

        res = AcquireToBoardRamPX14(hBrd, 0, ACQUISITION_SAMPLES,
5000,    PX14_FALSE);
        if (SIG_SUCCESS != res)
        {   if (res == SIG_PX14_TIMED_OUT)
            {    // Acquisition timed out
                        puts("RAM acquisition timed out.");
            }
            else
            {
                DumpLibErrorPX14(res, _T("Failed to do RAM acquisition:"),
hBrd);
                return -1;
            }
        }
        else
        {
            if (pDestFile != NULL)
            {
                    PX14S_FILE_WRITE_PARAMS fwp;
                    memset                  (&fwp,                  0,
sizeof(PX14S_FILE_WRITE_PARAMS));
                    fwp.struct_size = sizeof(PX14S_FILE_WRITE_PARAMS);
                        // Destination file pathname
                    fwp.pathname = pDestFile;
                    fwp.flags = PX14FILWF_GENERATE_SRDC_FILE;
```

```
                    printf ("Saving acquisition data to file...\n");
                    res = ReadSampleRamFileBufPX14(hBrd, 0,
ACQUISITION_SAMPLES, &fwp);
                    if (SIG_SUCCESS != res)
                    {
                        DumpLibErrorPX14(res, _T("Failed to do RAM
acquisition:"), hBrd);
                        return -1;
                     }
                }
            }

        return SIG_SUCCESS;
    }

    void clearScreen(void){
            system("cls");
         printf ("Long Term Data Recording Program\n");
        printf ("Make sure the sounder is operating before running this program\n");
        printf("This program Records '1s' duration data  at every min on both Cards-
1 and Card-2 \n");
        printf ("The user needs to specify the number of files (minutes to record)\n");
    }
```

Appendix C Matlab Code for Data Recording

```
%% Import data from text file.
% Script for importing data from the following text file:
%    D:\weather data\01.2018\CR1000_PWS100_Data_2018_01_01_2121.dat
% To extend the code to different selected data or a different text file,

clear all;
clc;

% Import the file
% Attenaution Measurement Data

fold_weather = 'D:\weather data\01.2018';
  dirs=dir(strcat(fold_weather,'\*.dat'));
 dircell=struct2cell(dirs)';
 filenames=dircell(:,1);
 loop=size(filenames);
for iixx =1:38785 %% Complete this for loop ... This should loop for all
the files
fileLocAtt = 'D:\Jan'; % Location of the Measurement Attenuation Data
DELIMITER_att = ' ';
HEADERLINES_att = 26;
delimiter = ',';
startRow = 5;

%% Read columns of data as strings:
formatSpec =
'%q%q%q%q%q%q%q%q%q%q%q%q%q%q%q%q%q%q%q%q%q%q%q%q%q%q%q%q%q%q%q%q%q%q%q%q%q%
%q%q%q%q%q%q%q%q%q%q%q%q%q%q%q%q%q%q%q%q%q%q%q%q%q%q%q%q%q%q%q%q%q%q%q%q%q%
q%q%q%q%q%q%q%q%q%q%q%q%q%q%q%q%q%q%q%q%q%q%q%q%q%q%q%q%q%q%q%q%q%q%q%q%q%q%
%q%q%q%q%q%q%q%q%q%q%q%q%q%q%q%q%q%q%q%q%q%q%q%q%q%q%q%q%q%q%q%q%q%q%q%q%q%
q%q%q%q%q%q%q%q%q%q%q%q%q%q%q%q%q%q%q%q%q%q%q%q%q%q%q%q%q%q%q%q%q%q%q%q%q%q%
%q%q%q%q%q%q%q%q%q%q%q%q%q%q%q%q%q%q%q%q%q%q%q%q%q%q%q%q%q%q%q%q%q%q%q%q%q%
q%q%q%q%q%q%q%q%q%q%q%q%q%q%q%q%q%q%q%q%q%q%q%q%q%q%q%q%q%q%q%q%q%q%q%q%q%q%
%q%q%q%q%q%q%q%q%q%q%q%q%q%q%q%q%q%q%q%q%q%q%q%q%q%q%q%q%q%q%q%q%q%q%q%q%q%
q%q%q%q%q%q%q%q%q%q%q%q%q%q%q%q%q%q%q%q%q%q%q%q%q%q%q%q%q%q%q%q%q%q%q%q%q%q%
%q%q%q%[^\n\r]';


fileID = fopen(strcat(fold_weather,'\',filenames{iixx}),'r');
```

```
dataArray = textscan(fileID, formatSpec, 'Delimiter', delimiter,
'HeaderLines' ,startRow-1, 'ReturnOnError', false);

fclose(fileID);

raw = repmat({''},length(dataArray{1}),length(dataArray)-1);
for col=1:length(dataArray)-1
    raw(1:length(dataArray{col}),col) = dataArray{col};
end
numericData = NaN(size(dataArray{1},1),size(dataArray,2));

for
col=[2,3,4,5,6,7,8,9,10,13,14,15,16,17,18,19,20,21,22,23,24,25,26,27,28,29,
30,31,32,33,34,35,36,37,38,41,42,43,44,45,46,47,48,49,50,51,52,53,54,55,56,
57,58,59,60,61,62,63,64,65,66,67,68,69,70,71,72,73,74,75,76,77,78,79,80,81,
82,83,84,85,86,87,88,89,90,91,92,93,94,95,96,97,98,99,100,101,102,103,104,1
05,106,107,108,109,110,111,112,113,114,115,116,117,118,119,120,121,122,123,
124,125,126,127,128,129,130,131,132,133,134,135,136,137,138,139,140,141,142
,143,144,145,146,147,148,149,150,151,152,153,154,155,156,157,158,159,160,16
1,162,163,164,165,166,167,168,169,170,171,172,173,174,175,176,177,178,179,1
80,181,182,183,184,185,186,187,188,189,190,191,192,193,194,195,196,197,198,
199,200,201,202,203,204,205,206,207,208,209,210,211,212,213,214,215,216,217
,218,219,220,221,222,223,224,225,226,227,228,229,230,231,232,233,234,235,23
6,237,238,239,240,241,242,243,244,245,246,247,248,249,250,251,252,253,254,2
55,256,257,258,259,260,261,262,263,264,265,266,267,268,269,270,271,272,273,
274,275,276,277,278,279,280,281,282,283,284,285,286,287,288,289,290,291,292
,293,294,295,296,297,298,299,300,301,302,303,304,305,306,307,308,309,310,31
1,312,313,314,315,316,317,318,319,320,321,322,323,324,325,326,327,328,329,3
30,331,332,333,334,335,336,337,338,339,340]
    rawData = dataArray{col};
    for row=1:size(rawData, 1);
        regexstr =
'(?<prefix>.*?)(?<numbers>([-]*(\d+[\,]*)+[\.]{0,1}\d*[eEdD]{0,1}[-
+]*\d*[i]{0,1})|([-]*(\d+[\,]*)*[\.]{1,1}\d+[eEdD]{0,1}[-
+]*\d*[i]{0,1}))(?<suffix>.*)';
        try
            result = regexp(rawData{row}, regexstr, 'names');
            numbers = result.numbers;

            % Detected commas in non-thousand locations.
            invalidThousandsSeparator = false;
            if any(numbers==',');
                thousandsRegExp = '^\d+?(\,\d{3})*\.{0,1}\d*$';
                if isempty(regexp(thousandsRegExp, ',', 'once'));
```

```
                    numbers = NaN;
                    invalidThousandsSeparator = true;
                end
            end
            % Convert numeric strings to numbers.
            if ~invalidThousandsSeparator;
                numbers = textscan(strrep(numbers, ',', ''), '%f');
                numericData(row, col) = numbers{1};
                raw{row, col} = numbers{1};
            end
        catch me
        end
    end
end

rawNumericColumns = raw(:,
[2,3,4,5,6,7,8,9,10,13,14,15,16,17,18,19,20,21,22,23,24,25,26,27,28,29,30,3
1,32,33,34,35,36,37,38,41,42,43,44,45,46,47,48,49,50,51,52,53,54,55,56,57,5
8,59,60,61,62,63,64,65,66,67,68,69,70,71,72,73,74,75,76,77,78,79,80,81,82,8
3,84,85,86,87,88,89,90,91,92,93,94,95,96,97,98,99,100,101,102,103,104,105,1
06,107,108,109,110,111,112,113,114,115,116,117,118,119,120,121,122,123,124,
125,126,127,128,129,130,131,132,133,134,135,136,137,138,139,140,141,142,143
,144,145,146,147,148,149,150,151,152,153,154,155,156,157,158,159,160,161,16
2,163,164,165,166,167,168,169,170,171,172,173,174,175,176,177,178,179,180,1
81,182,183,184,185,186,187,188,189,190,191,192,193,194,195,196,197,198,199,
200,201,202,203,204,205,206,207,208,209,210,211,212,213,214,215,216,217,218
,219,220,221,222,223,224,225,226,227,228,229,230,231,232,233,234,235,236,23
7,238,239,240,241,242,243,244,245,246,247,248,249,250,251,252,253,254,255,2
56,257,258,259,260,261,262,263,264,265,266,267,268,269,270,271,272,273,274,
275,276,277,278,279,280,281,282,283,284,285,286,287,288,289,290,291,292,293
,294,295,296,297,298,299,300,301,302,303,304,305,306,307,308,309,310,311,31
2,313,314,315,316,317,318,319,320,321,322,323,324,325,326,327,328,329,330,3
31,332,333,334,335,336,337,338,339,340]);
rawCellColumns = raw(:, [1,11,12,39,40]);

%% Replace non-numeric cells with NaN
R = cellfun(@(x) ~isnumeric(x) && ~islogical(x),rawNumericColumns); % Find
non-numeric cells
rawNumericColumns(R) = {NaN}; % Replace non-numeric cells

numMeas = length(rawCellColumns(:, 1));

for nW=1:numMeas
     clc;
```

```
      [iixx nW]
      [fYear, fMonth, fDay, fHour, fMin, fSec] = datevec(rawCellColumns(nW,
1));
      [MonthNum, fMonth] = month(rawCellColumns(nW, 1));
       %TextFileName = strcat(num2str(fDay),'-',fMonth,'-',num2str(fYear),'
Time-',num2str(fHour),'.',num2str(fMin));

       nDate1 = strcat('EBand -',num2str(fDay),'-',fMonth,'-
',num2str(fYear),' Time-',num2str(fHour),'.',num2str(fMin));
       nDate2 = strcat('KBand -',num2str(fDay),'-',fMonth,'-
',num2str(fYear),' Time-',num2str(fHour),'.',num2str(fMin));


       fileLocAtt1=strcat(fileLocAtt,'\',nDate1,'.txt');  %% attenuation
data for the EBand Address
       if exist(fileLocAtt1,'file')==0
          Pow_av_R1T1_e(nW,1) = nan; % maximun signal at 4MHz
          Powpeak_av_R1T1_e(nW,1) = nan; % The average of the sweeps peak
          Pow_av_R1T2_e(nW,1) = nan; % maximun signal at 4MHz
          Powpeak_av_R1T2_e(nW,1) = nan; % The average of the sweeps peak
          Pow_av_R2T1_e(nW,1) = nan; % maximun signal at 4MHz
          Powpeak_av_R2T1_e(nW,1) = nan; % The average of the sweeps peak
          Pow_av_R2T2_e(nW,1) = nan; % maximun signal at 4MHz
          Powpeak_av_R2T2_e(nW,1) = nan; % The average of the sweeps peak
       else       %% EBand InportData
           newData1 = importdata(fileLocAtt1, DELIMITER_att,
HEADERLINES_att);   %% Loads the attenuation data for the EBand
           freqaxis_e = newData1.data(1:41,1);
           Rx1Tx1_e = newData1.data(1:41,2:2:end);
           Rx1Tx2_e = newData1.data(42:82,2:2:end);
           Rx2Tx2_e = newData1.data(83:123,2:2:end);
           Rx2Tx1_e = newData1.data(124:164,2:2:end);
           for tr=1:1  %% Estimates the Peak and average Powers of EBAND
               aa = mean(Rx1Tx1_e,2); % The average of all sweeps at each
frequency
                    Pow_av_R1T1_e(nW,1) = max(aa); % maximun signal at 4MHz
               aa = max((Rx1Tx1_e));    % maximun of each sweep.
                    Powpeak_av_R1T1_e(nW,1) = mean(aa); % The average of the
sweeps peak

               aa = mean(Rx1Tx2_e,2); % The average of all sweeps at each
frequency
                    Pow_av_R1T2_e(nW,1) = max(aa); % maximun signal at 4MHz
               aa = max((Rx1Tx2_e));    % maximun of each sweep.
```

```
                    Powpeak_av_R1T2_e(nW,1) = mean(aa); % The average of the
sweeps peak

                aa = mean(Rx2Tx1_e,2); % The average of all sweeps at each
frequency
                    Pow_av_R2T1_e(nW,1) = max(aa); % maximun signal at 4MHz
                aa = max((Rx2Tx1_e));    % maximun of each sweep.
                    Powpeak_av_R2T1_e(nW,1) = mean(aa); % The average of the
sweeps peak

                aa = mean(Rx2Tx2_e,2); % The average of all sweeps at each
frequency
                    Pow_av_R2T2_e(nW,1) = max(aa); % maximun signal at 4MHz
                aa = max((Rx2Tx2_e));    % maximun of each sweep.
                    Powpeak_av_R2T2_e(nW,1) = mean(aa); % The average of the
sweeps peak
            end
        end
        clear fileLocAtt1;
        fileLocAtt1=strcat(fileLocAtt,'\',nDate2,'.txt');  %% Loads the
attenuation data for the KBand
        if exist(fileLocAtt1,'file')==0
                    Pow_av_R1T1_k(nW,1) = nan; % maximun signal at 4MHz
                    Powpeak_av_R1T1_k(nW,1) = nan; % The average of the
sweeps peak
                    Pow_av_R1T2_k(nW,1) = nan; % maximun signal at 4MHz
                    Powpeak_av_R1T2_k(nW,1) = nan; % The average of the
sweeps peak
                    Pow_av_R2T1_k(nW,1) = nan; % maximun signal at 4MHz
                    Powpeak_av_R2T1_k(nW,1) = nan; % The average of the
sweeps peak
                    Pow_av_R2T2_k(nW,1) = nan; % maximun signal at 4MHz
                    Powpeak_av_R2T2_k(nW,1) = nan; % The average of the
sweeps peak
        else
            newData2 = importdata(fileLocAtt1, DELIMITER_att,
HEADERLINES_att);
            freqaxis_k = newData1.data(1:41,1);
            Rx1Tx1_k = newData2.data(1:41,2:2:end);
            Rx1Tx2_k = newData2.data(42:82,2:2:end);
            Rx2Tx2_k = newData2.data(83:123,2:2:end);
            Rx2Tx1_k = newData2.data(124:164,2:2:end);

            for tr=1:1  %% Estimates the Peak and average Powers of EBAND
```

```
            aa = mean(Rx1Tx1_k,2); % The average of all sweeps at each
frequency
                 Pow_av_R1T1_k(nW,1) = max(aa); % maximun signal at 4MHz
            aa = max((Rx1Tx1_k));    % maximun of each sweep.
                 Powpeak_av_R1T1_k(nW,1) = mean(aa); % The average of the
sweeps peak

            aa = mean(Rx1Tx2_k,2); % The average of all sweeps at each
frequency
                 Pow_av_R1T2_k(nW,1) = max(aa); % maximun signal at 4MHz
            aa = max((Rx1Tx2_k));    % maximun of each sweep.
                 Powpeak_av_R1T2_k(nW,1) = mean(aa); % The average of the
sweeps peak

            aa = mean(Rx2Tx1_k,2); % The average of all sweeps at each
frequency
                 Pow_av_R2T1_k(nW,1) = max(aa); % maximun signal at 4MHz
            aa = max((Rx2Tx1_k));    % maximun of each sweep.
                 Powpeak_av_R2T1_k(nW,1) = mean(aa); % The average of the
sweeps peak

            aa = mean(Rx2Tx2_k,2); % The average of all sweeps at each
frequency
                 Pow_av_R2T2_k(nW,1) = max(aa); % maximun signal at 4MHz
            aa = max((Rx2Tx2_k));    % maximun of each sweep.
                 Powpeak_av_R2T2_k(nW,1) = mean(aa); % The average of the
sweeps peak
          end
      end

 end

 %% Concatinate the DATA

for ixx=1:1
    TIMESTAMP_ =[TIMESTAMP_; rawCellColumns(:, 1)];
    Pow_av_R1T1_e_=[Pow_av_R1T1_e_; Pow_av_R1T1_e];
    Powpeak_av_R1T1_e_=[Powpeak_av_R1T1_e_; Powpeak_av_R1T1_e];
    Pow_av_R1T2_e_=[Pow_av_R1T2_e_  ;Pow_av_R1T2_e];
    Powpeak_av_R1T2_e_=[ Powpeak_av_R1T2_e_ ;Powpeak_av_R1T2_e];

    Pow_av_R2T1_e_=[Pow_av_R2T1_e_  ;Pow_av_R2T1_e];
    Powpeak_av_R2T1_e_=[Powpeak_av_R2T1_e_  ;Powpeak_av_R2T1_e];
```

```
    Pow_av_R2T2_e_=[Pow_av_R2T2_e_  ;Pow_av_R2T2_e];
    Powpeak_av_R2T2_e_=[Powpeak_av_R2T2_e_  ;Powpeak_av_R2T2_e];

    Pow_av_R1T1_k_=[Pow_av_R1T1_k_  ;Pow_av_R1T1_k];
    Powpeak_av_R1T1_k_=[Powpeak_av_R1T1_k_  ;Powpeak_av_R1T1_k];

    Pow_av_R1T2_k_=[Pow_av_R1T2_k_  ;Pow_av_R1T2_k];
    Powpeak_av_R1T2_k_=[Powpeak_av_R1T2_k_  ;Powpeak_av_R1T2_k];

    Pow_av_R2T1_k_=[Pow_av_R2T1_k_  ;Pow_av_R2T1_k];
    Powpeak_av_R2T1_k_=[Powpeak_av_R2T1_k_  ;Powpeak_av_R2T1_k];

    Pow_av_R2T2_k_=[Pow_av_R2T2_k_  ;Pow_av_R2T2_k];
    Powpeak_av_R2T2_k_=[Powpeak_av_R2T2_k_  ;Powpeak_av_R2T2_k];


end

 clearvars Pow_av_R1T1_k Powpeak_av_R1T1_k Pow_av_R1T2_k Powpeak_av_R1T2_k
Pow_av_R2T1_k Powpeak_av_R2T1_k Pow_av_R2T2_k Powpeak_av_R2T2_k
Pow_av_R1T1_e Powpeak_av_R1T1_e Pow_av_R1T2_e Powpeak_av_R1T2_e
Pow_av_R2T1_e Powpeak_av_R2T1_e  Pow_av_R2T2_e  Powpeak_av_R2T2_e

 end %% This is the for loop into all the files in the WeatherStation Data

%% Create output variable

 CR_PWS_Data = table;  % Use this command to turn it inot

save('combinedata.mat','CR_PWS_Data');

%% Clear temporary variables
    clearvars filename delimiter startRow formatSpec fileID dataArray ans
raw col numericData rawData row regexstr result numbers
invalidThousandsSeparator thousandsRegExp me rawNumericColumns
rawCellColumns R;
```

Appendix D Matlab Code for DSD Fitting

```
load('F:\phd\processed\weather_201801.mat')
load('F:\writings0622\mat\matlabpara\dsdparameters.mat')
load('F:\writings0622\mat\2018raineventscoefficients\Jancoefficients.mat')
CR_PWS_Data1 = CR_PWS_Data{:,34:333};
CR_PWS_Data1(isnan(CR_PWS_Data1))=0;
PWS100_PrecipitationAccumulation_ = CR_PWS_Data{:,13};
len=length(CR_PWS_Data1);
d=zeros(len,1);
for i=1:len
    if any(CR_PWS_Data1(i,1:100))

d(i,1)=1;
    end
end
m=d*para(1,1:100);
Nd=m.*CR_PWS_Data1(:,1:100);
ndlarge=zeros(len,100);
ndlarge(:,16:100)=Nd(:,16:100);
x=linspace(0.1,10,100);
z=linspace(1,len/60/24,len);
% mesh(x,z,ndlarge);
mesh(x,z,Nd);
ylim([1 31]);
xlabel('Rain drop diameter (mm)','FontName','Times New
Roman','FontSize',14,'Rotation',15,'position',[5,-4]);
ylabel('Dates','FontName','Times New Roman','FontSize',14,'Rotation',-
25,'position',[-2,10]);
zlabel('DSD (m^{-3}mm^{-1})','FontName','Times New
Roman','FontSize',14,'Rotation',90);
    shg
rain(isnan(rain))=0;
size=length(rain);
d=zeros(size,1);
for i=1:size
    if any(rain(i,1))

d(i,1)=1;
    end
end
rainintensity=41*rain.^(-0.21);
nde(:,1:100)=8000.*exp(-(rainintensity./10).*a(1,1:100));
```

```
ndelarge=zeros(size,100);
ndelarge(:,16:100)=nde(:,16:100);
x=linspace(0.1,10,100);
z=linspace(1,size/60/24,size);
mesh(x,z,ndelarge);
% mesh(x,z,nde);
ylim([1 31]);
xlabel('Rain drop diameter (mm)','FontName','Times New
Roman','FontSize',14,'Rotation',15,'position',[5,-4]);
ylabel('Dates','FontName','Times New Roman','FontSize',14,'Rotation',-
25,'position',[-2,10]);
zlabel('DSD (m^{-3}mm^{-1})','FontName','Times New
Roman','FontSize',14,'Rotation',90);
shg
PWS100_AverageSize_ = CR_PWS_Data{:,15};%average size
CR_PWS_Data1 = CR_PWS_Data{:,34:333};%distribution
CR_PWS_Data1(isnan(CR_PWS_Data1))=0;
size=length(CR_PWS_Data1);
d=zeros(size,1);
for i=1:size
    if any(CR_PWS_Data1(i,1:100))

d(i,1)=1;
    end
end
m=d*para(1,1:100);
Nd=m.*CR_PWS_Data1(:,1:100);%measured DSD
Nt=sum(Nd./10,2);%total numbers
lna=log(d*a(1,1:100)./PWS100_AverageSize_).^2;
stdg=exp(sqrt(sum(lna.*Nd./10,2)/100));
exr=exp(((log(d*a(1,1:100))-
PWS100_AverageSize_*ones(1,100)).^2)./(2*stdg*ones(1,100).^2));
exl=(sqrt(2*pi))*stdg*a(1,1:100);
ex=exr./exl;
Ndlog=ex.*(Nt*ones(1,100));
x=linspace(0.1,10,100);
z=linspace(1,size/60/24,size);
mesh(x,z,Ndlog);
% mesh(x,z,Nd);
ylim([1 31]);
xlabel('Rain drop diameter (mm)','FontName','Times New
Roman','FontSize',14,'Rotation',15,'position',[5,-4]);
ylabel('Dates','FontName','Times New Roman','FontSize',14,'Rotation',-
25,'position',[-2,10]);
```

```
zlabel('DSD (m^{-3}mm^{-1})','FontName','Times New
Roman','FontSize',14,'Rotation',90);
    shg
%different rain attenuation models
%rain event 01/2018 in Durham. vertical polarised 27GHz/75GHz,distance:35m.
close all;
clear all;
clc;
load D:\codes\weatherdata\dataJan(10stepmaf).mat
fe=72;
fk=27;
d=0.035;
%clear sky mean
mean1 = mean(CR_PWS_Datafiltered{10:780,2});%'2018-01-01 21:30:00' to
{'2018-01-02 10:20:00'}
mean2 = mean(CR_PWS_Datafiltered{2778:3533,2});%{'2018-01-03 19:40:00'} to
{'2018-01-04 08:10:00'}
mean3 = mean(CR_PWS_Datafiltered{14460:15310,2});%{'2018-01-11 22:20:00'}
to {'2018-01-12 12:30:00'}
mean4 = mean(CR_PWS_Datafiltered{15340:18400,2});%{'2018-01-12 13:00:00'}
to {'2018-01-14 16:00:00'}
mean5 = mean(CR_PWS_Datafiltered{26390:28030,2});%{'2018-01-20 05:00:00'}
to {'2018-01-21 08:30:00'}
%ITU-R P.530
keh=1.0618;%for 72GHz
kev=1.0561;
aeh=0.7293;%for 72GHz
aev=0.7171;
kkh=0.1884;%for 27GHz
kkv=0.1813;
akh=0.9780;%for 27GHz
akv=0.9349;
rev(:,1)=kev*(CR_PWS_Datafiltered.PWS100_PrecipitationIntensity_(:)).^aev;%
step2: specific rain attenuation from ITU-R P.838
reh(:,1)=keh*(CR_PWS_Datafiltered.PWS100_PrecipitationIntensity_(:)).^aeh;
rkv(:,1)=kkv*(CR_PWS_Datafiltered.PWS100_PrecipitationIntensity_(:)).^akv;
rkh(:,1)=kkh*(CR_PWS_Datafiltered.PWS100_PrecipitationIntensity_(:)).^akh;
distance_factor_ITUev(:,1)=(0.477*(d^0.633)*(CR_PWS_Datafiltered.PWS100_Pre
cipitationIntensity_(:).^(0.073*aev))*(fe^0.123)-10.579*(1-exp(-
0.024*d)));%step3: effective path length eband vertical
distance_factor_ITUeh(:,1)=(0.477*(d^0.633)*(CR_PWS_Datafiltered.PWS100_Pre
cipitationIntensity_(:).^(0.073*aeh))*(fe^0.123)-10.579*(1-exp(-
0.024*d)));%step3: effective path length eband horizontal
```

```
distance_factor_ITUkv(:,1)=(0.477*(d^0.633)*(CR_PWS_Datafiltered.PWS100_Pre
cipitationIntensity_(:).^(0.073*akv))*(fk^0.123)-10.579*(1-exp(-
0.024*d)));%step3: effective path length kband vertical
distance_factor_ITUkh(:,1)=(0.477*(d^0.633)*(CR_PWS_Datafiltered.PWS100_Pre
cipitationIntensity_(:).^(0.073*akh))*(fk^0.123)-10.579*(1-exp(-
0.024*d)));%step3: effective path length kband horizontal

for i=1:height(CR_PWS_Datafiltered);%data size
if distance_factor_ITUev(i,1)<0.4;
    distance_factor_ITUev(i,1)=0.4;% maxmum distance factor is recommended
as 2.5
end
if distance_factor_ITUeh(i,1)<0.4;
    distance_factor_ITUeh(i,1)=0.4;% maxmum distance factor is recommended
as 2.5
end
if distance_factor_ITUkv(i,1)<0.4;
    distance_factor_ITUkv(i,1)=0.4;
end
if distance_factor_ITUkh(i,1)<0.4;
    distance_factor_ITUkh(i,1)=0.4;
end
end

attenuation_ITUev(:,1)=d*rev(:,1)./distance_factor_ITUev(:,1);
attenuation_ITUeh(:,1)=d*reh(:,1)./distance_factor_ITUeh(:,1);
attenuation_ITUkv(:,1)=d*rkv(:,1)./distance_factor_ITUkv(:,1);
attenuation_ITUkh(:,1)=d*rkh(:,1)./distance_factor_ITUkh(:,1);
%the UK (2003RAL) model
distance_factor_UK(:,1)=0.874+0.0225*((CR_PWS_Datafiltered.PWS100_Precipita
tionIntensity_(:).^0.54-1.7)*d^0.7);
attenuation_UK(:,1)=d*CR_PWS_Datafiltered.PWS100_PrecipitationIntensity_(:)
./distance_factor_UK(:,1);
%the Brazil model
distance_factor_Brazil(:,1)=1+(d/119*CR_PWS_Datafiltered.PWS100_Precipitati
onIntensity_(:).^-.0224);
rain_rate_factor(:,1)=1.763*CR_PWS_Datafiltered.PWS100_PrecipitationIntensi
ty_(:).^(0.753+0.197/d);
attenuation_Brazilev(:,1)=kev*rain_rate_factor(:,1).^aev*d./distance_factor
_Brazil(:,1);
attenuation_Brazileh(:,1)=keh*rain_rate_factor(:,1).^aeh*d./distance_factor
_Brazil(:,1);
attenuation_Brazilkv(:,1)=kkv*rain_rate_factor(:,1).^akv*d./distance_factor
_Brazil(:,1);
```

```
attenuation_Brazilkh(:,1)=kkh*rain_rate_factor(:,1).^akh*d./distance_factor
_Brazil(:,1);
%DSD model

DSD=CR_PWS_Data{:,50:349};
% f=75GHz refractive index Re=1.3
% f=75GHz size parameter x=2pi*diameter/wavelength
% f=75GHz wavelength=4mm
% f=27GHz refractive index Re=1.3
% f=27GHz size parameter x=2pi*diameter/wavelength
% f=27GHz wavelength=11mm
for j=1:300
    qexte(1,j)=mie(1.3,0.5*pi*(j/10-0.05));
    qextk(1,j)=mie(1.3,2*pi*(j/10-0.05)/11);
end
%attenuation
for i=1:43358
attene(i,1)=d*25*4.343*0.001*sum(qexte.*DSD(i,:));%Measuring area 40cm^2
attenk(i,1)=d*25*4.343*0.001*sum(qextk.*DSD(i,:));
end
    save('rainattenJan.mat');
```